

# **UCLA**

## **UCLA Electronic Theses and Dissertations**

**Title**

Exploring the Universality of Sonoluminescence

**Permalink**

<https://escholarship.org/uc/item/85b3s2d6>

**Author**

Bataller, Alexander William

**Publication Date**

2014

Peer reviewed|Thesis/dissertation

UNIVERSITY OF CALIFORNIA  
Los Angeles

# Exploring the Universality of Sonoluminescence

A dissertation submitted in partial satisfaction  
of the requirements for the degree  
Doctor of Philosophy in Physics

by

**Alexander William Bataller**

2014

© Copyright by  
Alexander William Bataller  
2014

ABSTRACT OF THE DISSERTATION

# Exploring the Universality of Sonoluminescence

by

**Alexander William Bataller**

Doctor of Philosophy in Physics

University of California, Los Angeles, 2014

Professor Seth Putterman, Committee Chair

Sonoluminescence is the phenomenon whereby acoustic energy is converted into light through the violent collapse of gas bubbles in a liquid. A salient feature of sonoluminescence is the emission of a blackbody spectrum. Recent experiments have shown that the flashes of light from sonoluminescence are generated from a dense plasma characterized by an unusually high electron density. Furthermore, this plasma is a new state of matter whose properties are derived from a thermodynamic equation of state and is independent of how it was generated. In this dissertation, the universality of sonoluminescence is tested and its plasma properties are explored. Highly-ionized dense plasmas are confirmed in two different sonoluminescence systems using new experimental techniques. Plasmas are generated in high-pressure gases for two different systems whose properties are remarkably similar to sonoluminescence in temperature and ionization. Taken together, these experiments show that the plasma of sonoluminescence is not unique to itself and is consistent with a newly-discovered phase of matter.

The dissertation of Alexander William Bataller is approved.

Gary Williams  
Benjamin Schwartz  
Seth Putterman, Chair

University of California, Los Angeles  
2014

*To my parents Gary and Susan for their unending support,  
my wife Veronica for daring me to dream bigger,  
and my country for encouraging second chances.*

*"When I discover something new it has a musty smell,  
as if it hadn't been opened since the world began."*

*-Buckminster Fuller*

# Contents

<b>List of Figures</b>	viii
<b>List of Tables</b>	xii
<b>1 Introduction</b>	1
<b>2 Background: Sonoluminescence and Strongly Coupled Plasma</b>	4
2.1 Sonoluminescence . . . . .	5
2.2 Strongly Coupled Plasma . . . . .	11
<b>3 Thermodynamic Theory</b>	14
3.1 Saha's Equation - Dilute Theory . . . . .	15
3.2 Saha's Equation - Dense Theory . . . . .	17
3.3 Saha's Equation - Multiple Ionization . . . . .	24
<b>4 Kinetic Theory</b>	30
4.1 Inverse Bremsstrahlung . . . . .	32
4.2 Thermalization Time . . . . .	37
4.3 Recombination Time . . . . .	38
<b>5 Sulfuric Acid Sonoluminescence</b>	42
5.1 Introduction . . . . .	43
5.2 Energy Balance for a Sonoluminescence Bubble Yields a Measure of Ionization Potential Lowering . . . . .	44

<b>6 Sonoluminescence-Laser Interaction</b>	<b>55</b>
6.1 Introduction . . . . .	56
6.2 Collision Time Measurements in a Sonoluminescing Plasma with a Large Plasma Parameter . . . . .	57
<b>7 Laser Breakdown in High-Pressure Gases</b>	<b>69</b>
7.1 Introduction . . . . .	70
7.2 Blackbody Emission from Laser Breakdown in High-Pressure Gases . . . . .	71
<b>8 Spark Discharge in High-Pressure Gases</b>	<b>82</b>
8.1 Introduction . . . . .	83
8.2 A Nanosecond, High-Power, Dense, Microplasma Switch for Visible Light .	84
<b>9 Conclusion</b>	<b>93</b>
<b>A Derivation of the Electron-Ion Collision Time</b>	<b>95</b>
<b>B Derivation of Coulomb Logarithm</b>	<b>97</b>
B.1 “Dilute” Model: . . . . .	97
B.2 “Daligault” Model: . . . . .	98
B.3 “Debye” Model: . . . . .	98
<b>C Derivation of Inverse Bremsstrahlung</b>	<b>100</b>
C.1 Drude model . . . . .	100
C.1.1 Electronic equation of motion . . . . .	100
C.1.2 Limits: $\omega\tau \gg 1$ . . . . .	102
C.1.3 Limits: $\omega\tau \gg 1$ and $\gamma \ll 1$ ( $\omega \gg \omega_p$ ) . . . . .	102
C.1.4 Limits: $\omega\tau \gg 1$ and $\gamma \gg 1$ ( $\omega \ll \omega_p$ ) . . . . .	103
C.2 Dawson derivation . . . . .	103
C.3 Zel'dovich and Landau derivation . . . . .	104
C.4 Conclusions . . . . .	105
<b>D Supplemental Material - Sulfuric Acid Sonoluminescence</b>	<b>108</b>

<b>E Supplemental Material - Sonoluminescence-Laser Interaction</b>	<b>111</b>
E.1 Experimental Setup . . . . .	111
E.2 Continuous Mie Scattering . . . . .	113
E.3 Spectrum . . . . .	114
<b>F Supplemental Material - Laser Breakdown in High-Pressure Gases</b>	<b>115</b>
F.1 Experimental Setup . . . . .	115
F.2 Opacity . . . . .	118
F.2.1 Spectral Saturation . . . . .	118
F.2.2 Absorption Lines . . . . .	119
F.3 Greybody . . . . .	121
<b>G Supplemental Material - Spark Discharge in High-Pressure Gases</b>	<b>127</b>
G.1 Experimental Setup . . . . .	127
G.2 Spectrum . . . . .	132
G.3 Shock waves . . . . .	135
<b>Bibliography</b>	<b>138</b>

# List of Figures

2.1	Spectrum of MBSL in Ar and O <sub>2</sub> -saturated water. Reproduced from Ref. [83]. . . . .	6
2.2	Plasma phase space. Reproduced from Ref. [49]. . . . .	12
3.1	Ionization reduction vs. electron density for various screening theories. . . . .	19
3.2	Free energy vs. ionization for various screening theories. . . . .	22
3.3	Phase diagram of xenon gas with various screening models. . . . .	23
3.4	Solution to Saha's equation vs. nuclei density . . . . .	26
3.5	Solution to Saha's equation vs. nuclei density for various temperatures. . . . .	27
4.1	Photon mean free path vs. electron density for various screening models. . . . .	34
4.2	Frequency-dependent electron-ion collision time vs. electron density for various screening theories. . . . .	35
4.3	Plasma reflection vs. electron density for various screening theories. . . . .	36
5.1	Sulfuric Acid: Bubble radius vs. time from Mie scattering. Reproduced from Ref. [56]. . . . .	45
5.2	Sulfuric Acid: Sonoluminescence spectrum. Reproduced from Ref. [56]. . . . .	46
5.3	Sulfuric Acid: Collapse and blackbody emission radius vs. sonoluminescence intensity. Reproduced from Ref. [56]. . . . .	48
6.1	Sonoluminescence-Laser: Mie and sonoluminescence intensity scatter plots. . . . .	59
6.2	Sonoluminescence-Laser: Histogram of sonoluminescence-laser interaction strength. . . . .	61

6.3	Sonoluminescence-Laser: Calculated plasma reflection vs. electron density for various screening theories. . . . .	63
6.4	Sonoluminescence-Laser: Light decay length vs. electron density for various screening theories . . . . .	65
6.5	Sonoluminescence-Laser: Frequency-dependent electron-ion collision time vs. electron density for various screening theories. . . . .	67
7.1	Laser Breakdown: Spectrally integrated plasma emission vs. radius and time. . . . .	73
7.2	Laser Breakdown: Calibrated spectrum vs. time for xenon breakdown at various pressures. . . . .	74
7.3	Laser Breakdown: Spectral intensity and blackbody fits for 5 bar xenon breakdown at various times. . . . .	76
7.4	Laser Breakdown: Blackbody temperature and emissivity vs. time for xenon, argon, and helium. . . . .	77
8.1	Spark Discharge: Laser transmission and plasma emission of spark discharges formed in 2 and 10 xenon gas as a function of time. . . . .	85
8.2	Spark Discharge: Experimental block diagrams. . . . .	87
8.3	Spark Discharge: Calibrated time-resolved spectrum for 10 bar xenon discharges. . . . .	89
8.4	Spark Discharge: Framing images of laser-plasma interactions for 10 bar xenon discharges. . . . .	91
A.1	Electron-ion collision trajectory . . . . .	96
D.1	Sulfuric Acid: Photograph of experimental setup. . . . .	108
D.2	Sulfuric Acid: Available energy at collapse radius vs. sonoluminescence intensity . . . . .	109
D.3	Sulfuric Acid: PMT histogram vs. PMT intensity and blackbody temperature. . . . .	110
E.1	Sonoluminescence-Laser: Block diagram of experimental setup. . . . .	111

E.2	Sonoluminescence-Laser: Continuous Mie scattering and Rayleigh-Plesset fit for water sonoluminescence. . . . .	113
E.3	Sonoluminescence-Laser: Calibrated spectrum of sonoluminescence with and without laser interaction. . . . .	114
F.1	Laser Breakdown: Photograph of experimental setup. . . . .	115
F.2	Laser Breakdown: Photograph of the polarizing variable attenuator. . . . .	116
F.3	Laser Breakdown: Block diagram of the experimental setup. . . . .	117
F.4	Laser Breakdown: Spectral saturation for xenon, argon, and helium breakdown. . . . .	119
F.5	Laser Breakdown: Absorption lines for xenon and argon breakdown. . . . .	120
F.6	Laser Breakdown: Spectrum of argon breakdown at elevated pressures. . . .	121
F.7	Laser Breakdown: Spectrum of 50 bar argon breakdown for various times with blackbody and greybody fits. . . . .	122
F.8	Laser Breakdown: Spectrum and greybody fits of 50 bar argon breakdown with various screening models. . . . .	123
F.9	Laser Breakdown: Plasma properties vs. time for 50 bar argon breakdown using greybody fits. . . . .	124
F.10	Laser Breakdown: Spectrum of 25 and 75 bar argon breakdown with greybody fits. . . . .	125
G.1	Spark Discharge: Photograph of the pressure chamber and a CAD cross section. . . . .	127
G.2	Spark Discharge: Microscope images of tungsten ablation before and after 32,000 discharges. . . . .	128
G.3	Spark Discharge: Experimental photograph of spark discharge with CW laser absorption. . . . .	129
G.4	Spark Discharge: Framing images of CW laser blocking with 20 bar xenon spark discharge. . . . .	130
G.5	Spark Discharge: Experimental photograph of spark discharge with YAG laser absorption. . . . .	131

G.6	Spark Discharge: Temporally-resolved spectral image for helium 10 bar spark discharge.	132
G.7	Spark Discharge: Spectral intensity of 10 bar helium and xenon discharge at early times.	133
G.8	Spark Discharge: Spectral intensity of xenon 10 and 2 bar taken at +100 and +20 ns, respectively.	133
G.9	Spark Discharge: Spectral intensity comparison of xenon 10 bar spark discharge and 0.5 bar laser breakdown.	134
G.10	Spark Discharge: Shock wave image of 10 bar xenon discharge.	135
G.11	Spark Discharge: Shock wave as a function of radius and time for 10 bar xenon discharge.	136
G.12	Spark Discharge: Shock wave radius and velocity as a function of time for 10 bar xenon discharge.	137

# List of Tables

3.1	Plasma parameters and calculated values of the ionization fraction for the plasmas explored in this thesis. . . . .	28
4.1	Calculated electron-electron, ion-ion, and electron-ion thermalization times for argon laser breakdown. . . . .	38
4.2	Calculated electron-electron, ion-ion, and electron-ion thermalization times for xenon laser breakdown. . . . .	38
4.3	Calculated recombination times for argon laser breakdown. . . . .	40
4.4	Calculated recombination times for xenon laser breakdown. . . . .	40
4.5	Calculated recombination times for xenon sonoluminescence. . . . .	40
F.1	Laser Breakdown: Plasma parameters for argon breakdown using greybody values. . . . .	126

## ACKNOWLEDGMENTS

I would like to thank my advisor, Professor Seth Putterman, for giving me all of the tools that I needed to succeed. I am forever grateful to Seth for taking a chance on a young student with wild ideas to change the world. Seth has guided me through every stage of my graduate degree and has provided me both the means and ability to conduct scientific research at the highest level. An even greater attribute than his vast knowledge of physics is Seth's excitement for exploring new frontiers of science. This combination of wisdom and youthfulness has made him a luminary in physics and an incredible mentor. His work and unending passion for physics will inspire me for the rest of my life.

I would like to thank Professor Gary Williams and Professor Keith Weninger for their valuable discussions and guiding me through the world of sonoluminescence, as they are indeed masters of its study. I also thank Professors Giovanni Zocchi and Benjamin Schwartz for being on my committee and taking the time to guide me through the thesis process.

I would like to thank my current and former lab mates: Dr. Carlos Camara, Dr. Brian Kappus, Dr. Brian Naranjo, Dr. Johnathan Hird, Dr. Adam Collins, Dr. Emil Kirilov, Dr. Guillaume Plateau, Dr. John Koulakis, and Seth Pree. I owe special thanks to Dr. Carlos Camara, Dr. Brian Kappus, and Dr. John Koulakis. Dr. Carlos Camara took me under his wing and taught me how to conduct research like an experimentalist and how to think like an experimentalist. He is a brilliant scientist and a great friend. Dr. Brian Kappus has guided me through numerous experiments and is the finest experimental physicist I know. Working with Dr. Brian Kappus has been an absolute privilege. I thank Dr. John Koulakis for learning the field of spark discharges with me and suffering through many of its challenges. He is a good friend and is the type of critically-minded scientist that every lab should have. The experiments and results of this thesis could not have been accomplished without the efforts and guidance of these exceptional scientists.

I would like to thank the tireless professionals in the Physics Machine Shop for making these experiments possible. In particular, I would like to thank Harry Lockhart and Shylo Stiteler for giving me the tools to create high-level experiments. Although they are both experts in their craft, their primary passion is in education and they represent the

definition of an "open door policy".

I would like to thank my friends and family who've given me so much love and support. No one can ask for more when it comes to my parents, as they've provided for all my needs and shown me the importance of a good education. I thank my sister Becky for teaching me to never be content with your life and that education is a life-long endeavor. I thank my sister Janel for having my back during my hardest moments. I thank my brother William whose own life inspires me to have the courage for my convictions. I thank the entire Augustyn clan for accepting me into their home and encouraging my struggles in academia. I am proud to call them my family. I thank the great friends in my life who've provided much needed laughs throughout my graduate career. I thank Cory Welch for his guidance, support, and being a life-long friend. I thank Wade, Jessica, and Mikhail for all the fun times we've had in and around Los Angeles, and for all our future adventures. I especially thank my loving wife Veronica. She is my inspiration and the love of my life, and has consistently pushed me to achieve beyond what I thought was possible.

Chapter 5, "Energy Balance for a Sonoluminescence Bubble Yields a Measure of Ionization Potential Lowering" is a modified version of the published work in the Physical Review Letters Ref. [56] by Dr. Brian Kappus, the author of this thesis, and Prof. Seth Puterman. Both Dr. Brian Kappus. and the author of this thesis contributed to the experimental design, implementation, data acquisition, and analysis.

Chapter 6, "Collision Time Measurements in a Sonoluminescing Plasma with a Large Plasma Parameter" is a manuscript submitted to the Physical Review Letters by the author of this thesis, Dr. Brian Kappus, Dr. Carlos Camara, and Prof. Seth Puterman. Dr. Camara's expertise in SL and Mie scattering was instrumental to the experiment's successful SL-laser coupling. Dr. Kappus and Prof. Puterman's knowledge and advancement of plasma kinetic theory was crucial to the data analysis and interpretation.

Chapter 7, "Blackbody Emission from Laser Breakdown in High-Pressure Gases" is a manuscript submitted to the Physical Review Letters by the author of this thesis, Dr. Guillaume Plateau, Dr. Brian Kappus, and Prof. Seth Puterman. Dr. Plateau aided in laser alignment and provided beam diagnostics.

Chapter 8, "Spark Discharge in High-Pressure Gases" was an experiment conducted by the author of this thesis, Dr. John Koulakis, Seth Pree, and Prof. Seth Puterman.

This research was supported by the Defense Advanced Research Projects Agency (DARPA) in the Microsystems Technology Office (MTO) and from the Air Force Office of Scientific Research (AFOSR). Special thanks goes to the Microscale Plasma Devices (MPD) program and Dr. Dan Purdy at DARPA. Their foresight and innovative efforts in both understanding and applying dense plasmas has been essential to the success of this thesis.

## VITA

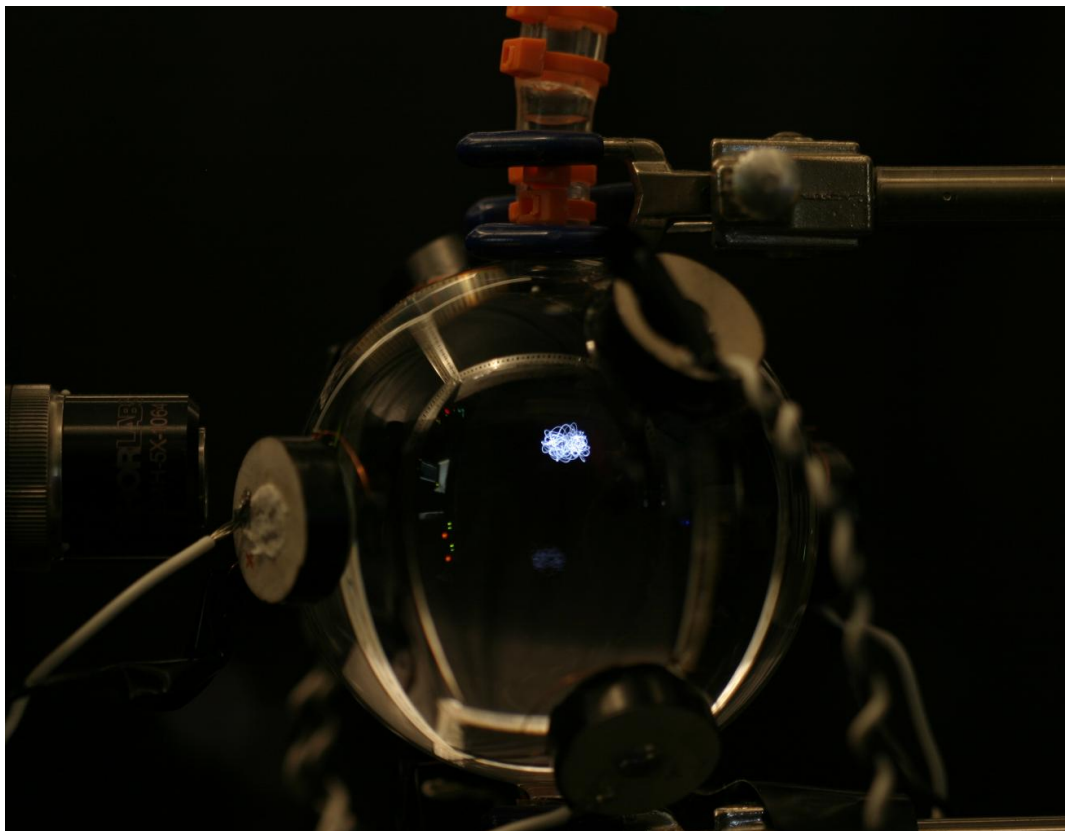
- 2005            *Summer Undergraduate Laboratory Internship*  
                    Pacific Northwest National Laboratory  
                    Richland, Washington
- 2006 - 2007     *Research and Development Intern*, Sion Power  
                    Tucson, Arizona
- 2007            *Engineering Directorate Scholarly Internship*  
                    Lawrence Livermore National Laboratory  
                    Livermore, California
- 2007            *Undergraduate Student Researcher*  
                    Department of Physics  
                    The University of Arizona, Tucson
- 2007            *B.S. in Engineering Physics*  
                    The University of Arizona, Tucson
- 2008 - 2014     *Graduate Student Researcher*  
                    Department of Physics and Astronomy  
                    University of California, Los Angeles

## PUBLICATIONS

B. Kappus, **A. Bataller**, and S.J. Puttermann, "Energy Balance for a Sonoluminescence Bubble Yields a Measure of Ionization Potential Lowering." *Physical Review Letters*, 111(23):234301, December 2013.

# Chapter 1

## Introduction



<sup>1</sup>The phenomenon known as sonoluminescence (SL) has marveled the observer since its discovery with both its eerie liquid confinement and otherworldly radiance. Indeed, this author has found himself on many occasions pausing the business of science to admire this beautiful effect. The SL effect is observed when a gas bubble surrounded by a fluid undergoes a catastrophic acoustic collapse due to the surrounding pressure gradients. Upon collapse, a brilliant flash of light is emitted from which SL owes its name. Since the early 1990s, a great deal of scientific effort has been dedicated to describing the generating mechanisms of SL and exploring its vast parameter space. As a result, the dynamics of SL has been measured with great accuracy and is well described by the equations of non-linear fluid dynamics. However, due to its micron size and picosecond lifetime, the specific mechanism which generates the light emission in SL has not been fully understood. Many theories have been proposed to explain SL's light emission, ranging from electric discharges to the exotic Casimir effect. In 2010, an experimental breakthrough was made by Dr. Brian Kappus where an SL bubble was generated with a  $100 \mu\text{m}$  collapse size and a  $1 \mu\text{s}$  lifetime [57]. These parameters made temporally and spatially resolved measurements possible and provided strong insight into SL's light-emitting mechanism. The conclusion of this work and experiments that followed [61][56] is that the light is bremsstrahlung radiation emitted from a highly-ionized and dense plasma. Furthermore, this plasma is unique in the world of plasma physics as it is a new phase of matter, characterized by its unusually high free-electron density. This paradigm shift has had a profound influence on not only the field of SL, but also the plasma physics community as it opens up a new parameter space. However, with every great discovery comes the need for experimental confirmation and new theoretical predictions. This dissertation is dedicated to both of these requirements by 1) further confirmation of SL as a highly-ionized dense plasma and 2) testing the universality of this new phase of matter by generating SL outside its liquid confines. What follows is this author's journey into the experimental worlds of both SL and dense plasma physics and my humble attempt at linking the two.

This dissertation is organized by first reviewing the history of SL in Chapter 2.

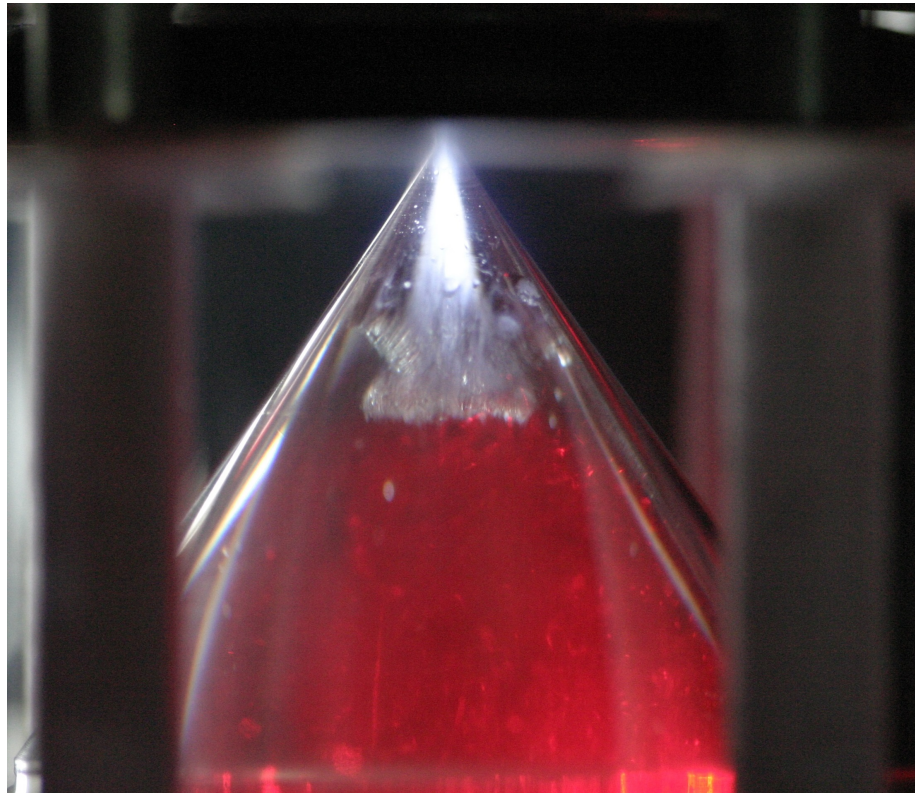
---

<sup>1</sup>Chapter Image: Long exposure of xenon sonoluminescence in concentrated sulfuric acid. An objective (left) focuses a high-intensity laser pulse for initial bubble seeding. The long camera exposure results in a swirling mass of light that traces the bubble's path within the fluid.

Strongly-coupled plasma is defined and a link is made to SL plasma. Chapter 3 reviews the thermodynamic theory of plasma and presents methods for describing dense plasma. Similarly, Chapter 4 reviews kinetic theory. The purpose of Chapters 3&4 is to provide both a physical understanding of plasma phenomenon and testable predictions, which are compared to the experimental findings. Chapters 5-8 present the experiments performed. The first two experiments (Chapters 5&6) are the SL experiments and the last two experiments (Chapters 7&8) are aimed at generating SL outside of a liquid. The experiment presented in Chapter 5 is a detailed measurement of a xenon bubble in sulfuric acid. The results of this experiment provide further evidence of SL being a dense plasma whose properties indicate a significant ionization-potential lowering. This experiment is best compared to the thermodynamic theory of Chapter 3. The experiment presented in Chapter 6 is a laser-plasma study where a high-intensity laser pulse is focused onto a xenon bubble in water. The resulting interaction strength for different laser wavelengths provides insight into the charge density and collisionality of the dense SL plasma. This experiment is best compared to the kinetic theory of Chapter 4. The experiment presented in Chapter 7 represents the lion's share of the thesis work. This experiment's goal is to reproduce the conditions of a SL plasma without the generating mechanism of non-linear fluid dynamics, thereby testing its universality. This was accomplished using laser-breakdown of high-pressure noble gases. The emission from this dense plasma is diagnosed and compared to both elements of kinetic and thermodynamic theory. The results of this experiment show a very strong similarity to the plasma of SL and helps confirm a new plasma state. Another experiment aimed at reproducing SL outside of a liquid is presented in Chapter 8. This experiment generates a dense plasma through the use of a spark-breakdown in high-pressure noble gases. Although this experiment is not as fully developed as that of the laser-breakdown experiment, it does provide a completely different plasma generation and a new measurement of an SL-like plasma. Finally, Chapter 9 summarizes the key findings of the experiments and their comparison to dense plasma theory. Potential experiments are discussed and future measurements considered for what is truly a very rich topic in physics.

## Chapter 2

### Background: Sonoluminescence and Strongly Coupled Plasma



## 2.1 Sonoluminescence<sup>1</sup>

The history of sonoluminescence (SL) begins with its discovery in 1934 by H. Frenzel and H. Schultes [31]. Motivated by recent advances in sonar technology, Frenzel and Schultes sought a quicker development of photographic film by subjecting development fluid to ultrasonic excitation. In the process, they observed tiny flashes of light emanating from within the fluid, which they described as bubbles undergoing electric discharge. And thus, the field of SL was born along with the first of many interpretations of a poorly understood phenomenon.

For the first 50 years after its discovery, SL was primarily generated by the non-resonant acoustic excitation of a fluid. This arrangement creates a cloud of cavitating bubbles and is now known as multi-bubble sonoluminescence (MBSL). After its initial discovery, the study of SL progressed slowly, with dark-adapted eyes as the primary diagnostic as the photomultiplier tube and oscilloscope were in their infancy. Even with this limitation, in 1939 E. Harvey published a study of the effects of various parameters on SL emission [42]. In fact, many of the parameters under investigation would be revisited 50 years later using modern instrumentation. It would take until the late 1950s before the publication of SL spectrum and bubble dynamics. A summary of these findings were published by P. Jarman in 1960, which noted a thermal-like spectrum and light emission coinciding with the final stage of collapse [54]. Jarman noted a model for adiabatic compression and heating of the bubble to temperatures of thousands of degrees, whereby thermal radiation is the source of light emission. It is mentioned even in this early work that the bubble emission “resemble that of a blackbody”. However, due to the spectrum being uncalibrated, the flashwidth and size of emission being unknown, and the ensemble nature of MBSL, blackbody confirmation was not possible. Jarman also proposed a model of “microshocks” to describe the thermal-like spectrum. In this model, converging shock

---

<sup>1</sup>Chapter Image: Backlit strobe photograph of “Conical Sonoluminescence” at the moment of light emission (unpublished work). An accelerating column of ethylene glycol collapses a large volume of low pressure xenon gas into a conically-shaped hollowed-out polycarbonate housing. The rising fluid blocks a He:Ne laser which is used to time the strobe relative to the plasma emission, and highlights the fluid in red. Plasma is formed at the apex of the cone during maximum compression and produces a bright flash of light, whose flashwidth can range from 100 ns to 10 ms! “Conical Sonoluminescence” represents one of the many historical paths for studying sonoluminescence.

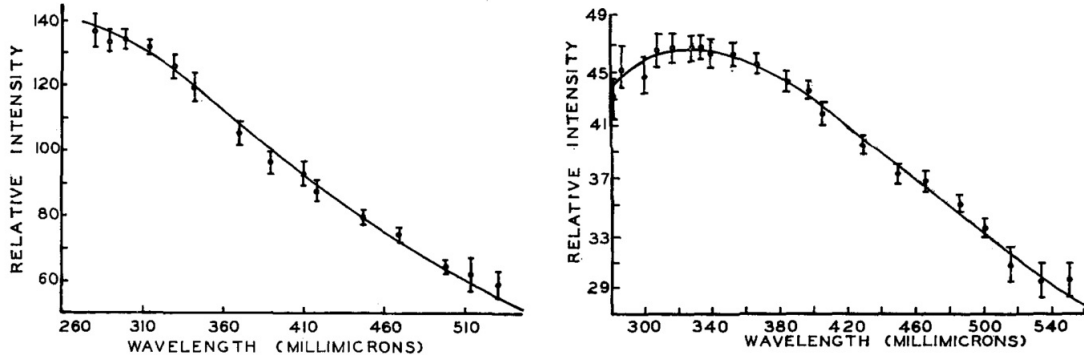


FIG. 2. Spectral distribution for argon-saturated water. Solid line is theoretical curve for blackbody temperature of 11 000°K.

FIG. 4. Spectral distribution for oxygen-saturated water. Solid line is theoretical curve for blackbody temperature of 8800°K.

Figure 2.1: Spectrum of MBSL in Ar and O<sub>2</sub>-saturated water by Holroyd et al. [83]

waves form during the bubble's final collapse stage and create shock heating similar to shock-tube experiments. This description would persist through the years and it is still considered a plausible model for SL in water. Jarman confidently ends the article with a bold prediction that “another decade of experiments should settle these issues.” Sadly, it would take over 40 years before blackbody emission could be confirmed.

Similar to the decades preceding it, little research was conducted in the 60s and 70s. However, uncalibrated spectrum taken by Holroyd et al. [83] showed excellent blackbody fits with temperatures between 8,800 and 11,000 K (Fig. 2.1). Without missing a beat, Holroyd published work showing that the light emission occurs in the collapse phase of the bubble, in the very next article of the same journal[67]. Still, characterization of the bubble dynamics was hindered by the convolution of many bubble collapses. In this time period, notable experiments were conducted that generated SL from a single bubble in various ways. An experiment by West and Howlett [95] created SL by bombarding degassed tetrachloroethylene with pulses of fast neutrons and thus seeding cavitation. The liquid was resonantly driven at 20 kHz with an amplitude of up to 20 atm, which brought about strong collapses after initial bubble growth. This method would be revisited in 2002 by Taleyarkhan [89] of “sonofusion” infamy. An experiment was conducted by Buzukov and Teslenko [14] where a large laser pulse was focused in water, causing dielectric breakdown and an expanding bubble. This bubble would collapse after its initial expansion and create a single SL flash. This work would also be revisited 3 decades later [1] and be known as

laser-induced cavitation. An effort to stabilize a single SL bubble was made by Saksena and Nyborg in 1970 [80] where an injected bubble rising in a column of viscous fluid were subjected to ultrasonic excitation. This work confirmed SL's periodicity with the sound field and showed a single pulse of light at the time of collapse for an isolated bubble. The concepts of bubble generation in this work would be crucial to later experiments involving water hammers ([85, 17, 57]) and drop tubes ([60, 58]). Ultimately, the effort to stabilize a single SL bubble was realized in 1970 by Temple [90]. In this experiment, SL was trapped at a velocity node in a resonant field and emitted light at the driving frequency. This work would pave the way for the explosion of SL research later in the 1990s. Although these experiments showed great promise, detailed bubble dynamics and spectral measurements in a resonant system would not occur for another two decades.

The 1980s belonged to the chemists as a whole new field arose known as Sonochemistry. Exploration of MBSL in various liquids and gases produced spectra with atomic and molecular excitation lines. These lines provided insight into the state of the heated gas bubble, and showed that the light is being radiated from a plasma at temperatures of thousands of degrees. As a consequence, high temperature chemistry occurs within the contents of the cavitating bubbles, which are otherwise difficult to achieve. For further insight into the topic, an excellent review of the subject has been published by Suslick [86]. The model of a rapidly collapsing gas bubble undergoing adiabatic heating and compression became the general consensus. However, the specific dynamics of the bubble's collapse and subsequent light emission was still unknown. This would all change with the advent of single-bubble sonoluminescence (SBSL).

In 1989, F. Gaitan and L. Crum [33] successfully trapped a single bubble in a resonant sound field, which produced SL with every acoustic period. This newly discovered method opened the door for measuring the bubble dynamics of SL and the properties of its light emission. Interest in SL exploded in the following decades, due mostly to the arrival of stable SBSL. To put this in perspective, the number of SL publications from 1990 to 1995 roughly equaled all publications from its discovery in 1934 to 1989! This was truly an exciting time for the experimentalist as access to SBSL was now available to any lab for little cost. Below are some of the key findings made during this time, which provided insight into the properties of SL.

1. *Bubble Dynamics:* For the first time, time-resolved collapse dynamics were observed for a single bubble using a technique called Mie scattering [33, 3]. This measurement showed that an air bubble in water undergoes a slow expansion phase and grows to ten times its static radius. The bubble then collapses at supersonic speeds and is compressed to near liquid densities! At the time of minimum collapse radius, a flash of light is emitted. This process repeats itself for every acoustic cycle with a clock-like synchronicity [6]. In some cases, the flash-to-flash jitter was below 50 ps [4]! An excellent overview of this “roller-coaster” phenomenon was published by Seth Puterman in 1995 [77]. Although many questions remained, it was determined that a highly-compressed gas bubble with a submicron size was the source of SL’s light emission.
2. *Flashwidth:* Before the arrival of SBSL, the flashwidth of SL was known to be very short. Even the fastest photomultipliers and oscilloscopes of the time could not resolve its flashwidth, making it a subnanosecond phenomenon. However, SBSL gave new life to this measurement through a technique called time-correlated single-photon counting. Using this technique, the flashwidth of SL was shown to be in the 100 ps timescale [38, 47].
3. *Spectrum:* The spectrum from SBSL in water was measured and found to be continuous in nature and void of line emission [46, 45, 69, 34, 47]. In all cases, the spectrum compared well to thermal emission and particularly to blackbody radiation. These fits showed a gas emitting at temperatures  $\gtrsim 10,000$  K.

During this decade, a number of theories were suggested to describe the observations of SBSL. A new electric discharge theory was proposed by Margulis in 1994 [68], which continued the idea of charge separation with subsequent discharge illumination originally proposed by Frenzel and Schultes. However, this theory has since been dismissed as an incorrect application of bubble fragmentation as described by Lepoint et al. [65]. An exotic theory of SL emission based on the Casimir effect was proposed by Eberlein [26] in 1996, but was quickly rejected [71, 12]. The most widely accepted theory for SL emission is the adiabatic compression model proposed as early as 1950 by Neppiras and Noltingk

[73]. In this model, the gas bubble undergoes a rapid collapse and is adiabatically heated to thousands of degrees. At thousands of degrees, the gas becomes ionized and emits bremsstrahlung radiation which is a continuous spectrum. In addition to the adiabatic compression theory, the shock-wave model suggested by Jarman in 1960 [54] was also revisited [97] due to the supersonic collapse speeds found in SBSL experiments. This model continues to be a plausible mechanism for the very high temperatures obtained in water SBSL[7].

Although great experimental gains and theoretical insights were made during this decade, a new paradox in SL would arise. This paradox was addressed by K. Yasui in 1999 [101], Vazquez et al. in 2001 [92], and Camara et al. in 2004 [15]. The spectral measurements of SBSL had now been calibrated due to the direct measurements of the SL flashwidth. The spectrum not only showed excellent fits to a blackbody in shape, but also in intensity as compared to the newly measured collapse radius. The emission from SBSL appeared to be radiating from an opaque plasma by these conclusions. However, to be a surface emitter (opaque), two conditions must be met. The first is that light and matter must be in thermal equilibrium. The second is that a photon must undergo many absorptions and re-emissions before leaving the body. This second condition appeared to be unsatisfied by SL as estimates for the photon mean-free-path ( $l_\nu$ ) were much larger than a micron. The big question in SL now became: How can SL be a blackbody with such a small size? An answer to this question would come with the arrival of SBSL in acids.

The study of SBSL has a vast parameter space such as temperature, gas mixture, driving amplitude and frequency, etc. It was predicted that lowering the vapor pressure of the driving liquid would increase the brightness of the SBSL emission by reducing the amount of vapor inside the bubble, and thereby maintaining a pure noble gas. Inorganic acids such as sulfuric and phosphoric acid proved to be excellent candidates with both very low vapor pressures and high optical transparency. In 2005, Flannigan and Suslick generated xenon and argon SBSL in concentrated sulfuric acid, which had an increased brightness of 1500 and 2700 times that of water, respectively [28]. Shortly thereafter, Hopkins et al characterized the bubble dynamics, flashwidth, and spectrum of a xenon bubble in sulfuric acid [48]. The results from this experiment show that bubbles generated

in sulfuric acid have much larger collapse radii ( $4\text{ }\mu\text{m}$ ) and longer flashwidths (10 ns) which result in the increased brightness compared to water. Once more, the spectrum is very well fit to a blackbody whose radius of emission also matches the collapse radius. Although the collapse radius is much larger than water SBSL, the plasma temperature is similar and therefore the blackbody paradox is again confronted. This shows that under vastly different experimental conditions, blackbody emission is a robust feature of SBSL. However, a firm explanation to the blackbody paradox still eluded the field.

To gain further insight into the temporally and spatially-resolved properties of the SBSL emission process, a larger and longer lasting bubble is required due to the experimental and technological limitations. Advancements in the stabilizing methods of rotating water hammers [85] and the larger and longer SL emission from inorganic acids led to incredibly bright and long lived bubbles [60]. These conditions led to the groundbreaking experiment conducted by Kappus et al. and the discovery of SL as a new phase of matter and a potential solution to the blackbody paradox [57]. In this experiment, a trapped xenon bubble is made to oscillate at 40 Hz in a cylindrical quartz tube filled with concentrated phosphoric acid. This configuration produced a very large bubble with a collapse radius of  $50\text{ }\mu\text{m}$  and a flashwidth of  $1\text{ }\mu\text{s}$ . At the time, it was believed SBSL was opaque due to its supersonic collapse speeds, which produced a very hot inner plasma core through shock-waves. However, the bubble created by Kappus had a collapse speed that was slower than the speed of sound and therefore was not expected to create shock-waves, and therefore a transparent plasma. This was not the case as again, the spectrum was an excellent blackbody fit, whose radius of emission matched the measured collapse radius! Once again, the blackbody paradox was present as  $l_\nu \sim 10^4 R_c$ . Owing to the much longer flashwidth, time-resolved spectroscopy was performed and showed a strong  $\text{Xe}^*$  line before and after the minimum collapse radius. Using this line emission and the blackbody fit, a new theory was presented where SL originates as a new form of matter, characterized by an unusually high electron density. Previously in the field of SL, electron density had been calculated using Saha's equation, which is applicable to a dilute plasma. However, as we will see in the following section, SL cannot be considered a dilute plasma. Recognizing this, Kappus et al. applied density corrections to Saha's equation and found that two solutions existed for a given temperature and atomic density. One solution is

weakly ionized and optically transparent (dilute limit). The other solution is completely ionized and optically opaque (dense limit). This dense limit is believed to be a new state of matter and provides a potential solution to the blackbody paradox.

In summary, SL is produced by the emission of a hot compressed gas. The phenomenon of SL exists in a large parameter space resulting in a wide range of emission properties. The flashwidth can range from 50 ps to as long as 1  $\mu\text{s}$ . Similarly, the size of the emitting region can range from 100 nm to as large as 100  $\mu\text{m}$ . SL is very robust over this enormous parameter space which suggests its intrinsic properties are fundamental. Indeed, over this parameter space, the blackbody temperature remains between 6,000 to 20,000 K and the atomic density is between  $1 - 10 \times 10^{21} \text{ cm}^{-3}$ . It is these two properties which make SL unique in nature and, as will be shown in the next section, a part of a larger class of matter known as strongly coupled plasma (SCP).

## 2.2 Strongly Coupled Plasma

A plasma is loosely defined as an ionized substance (often net neutral charge) and is considered a fundamental state of matter. Unlike solids, liquids, and gases, plasmas are not defined by a 1<sup>st</sup> order phase transition. Instead, the ionization changes smoothly as a function of temperature and density<sup>2</sup>. This definition creates an enormous phase space in which plasmas can exist as shown in Fig. 2.2. Numerous laboratory and astrophysical plasmas occupying the phase space of Fig. 2.2 and can be further grouped based on their similar temperatures and densities. One key distinction is made between what are known as ideal and non-ideal plasmas. This distinction is defined by the unitless parameter known as the plasma coupling parameter

$$\Gamma \equiv \frac{E_{\text{potential}}}{E_{\text{kinetic}}} = \frac{e^2}{k_B T} \left( \frac{4\pi n}{3} \right)^{1/3}, \quad (2.2.1)$$

where  $T$  is the temperature and  $n$  is the density. This quantity compares the electrostatic potential energy to the kinetic energy of the charged particles. Plasmas whose  $E_{\text{kinetic}} \gg$

---

<sup>2</sup>According to the discovery made in [57], the plasma of SL represents a 1<sup>st</sup> order phase transition. In this theory, SL plasma is defined by its high level of ionization and an abrupt transition in plasma properties. Ironically, SL plasma is categorized as a “non-ideal” plasma.

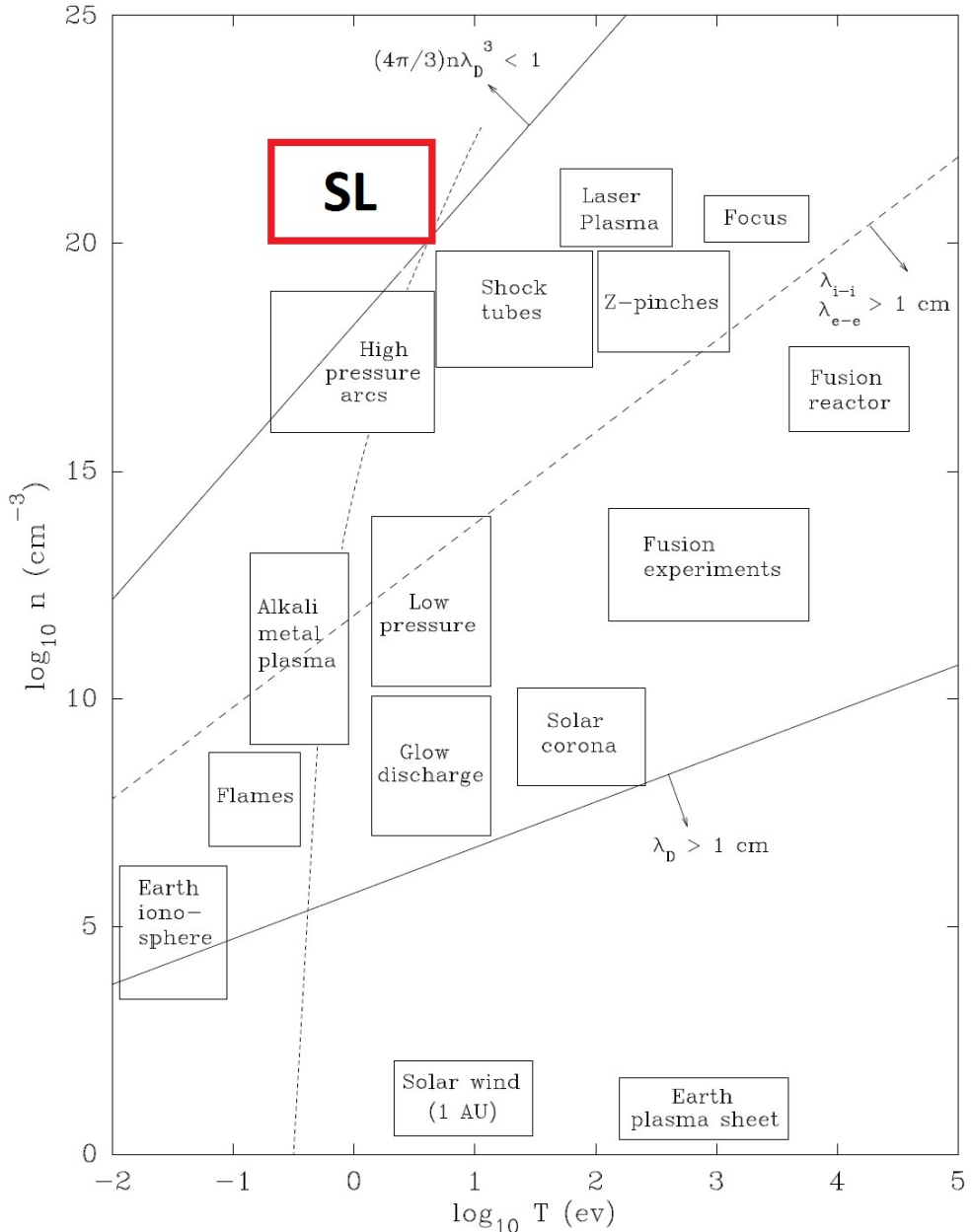


Figure 2.2: Plasma phase space in temperature and density. The graph above is a modification from [49] which now includes sonoluminescence (SL). Regions top-left of the  $(4\pi n/3)\lambda_D^3 < 1$  line represents non-ideal plasmas.

$E_{potential}$  are known as “ideal” or “weakly interacting” plasmas. In Fig. 2.2, ideal plasmas are located in regions where  $\Gamma \lesssim 1$  ( $(4\pi/3)\lambda_D^3 > 1$ ). Plasmas whose  $\Gamma \gtrsim 1$  are known as “non-ideal” or “strongly coupled plasmas” (SCP). For ideal plasmas, the equation of state for each species is described as an ideal gas (see Chapter 2). For SCPs, interparticle correlations and screening effects significantly alter the equation of state from that of an ideal gas. The equation of state in this regime is theoretically difficult to obtain due to the many-body nature of SCPs, and remains unresolved. Although not shown in Fig. 2.2, many SCPs have been generated in laboratory settings, notably through laser-solid interactions including inertial confinement fusion. A great deal of work has been done in this field and a full background is beyond the scope of this dissertation. Interested persons are encouraged to read the works of Ichimaru [50] and Fortov [?, 30].

As stated earlier, SL temperatures and densities range from 6,000-20,000 K and  $1 - 10 \times 10^{21} \text{ cm}^{-3}$ , respectively. These values result in  $1.3 < \Gamma < 9.7$  and by definition, SL is considered an SCP. Therefore, SL belongs to a much larger class of plasmas whose intrinsic properties are thermodynamic in nature, and not dependent upon its generating mechanism. To test this claim, the author of this thesis has endeavored to bring SL outside of its liquid confines.

# Chapter 3

## Thermodynamic Theory

When discussing the experimental observations of SL and SCP, it is important to consider whether the system has established local thermodynamic equilibrium (LTE). Assuming a system of constant temperature and volume, this occurs when the system's Helmholtz free energy  $F$  is minimized. For our system under consideration, LTE occurs when the constituent particles assume a Maxwell-Boltzmann distribution. Once LTE is established, all other thermodynamic properties can be derived from  $F$ . These include, and are not limited to, the equation of state, entropy, chemical potential, energy, and heat capacity of the system.

$$p = - \left( \frac{\partial F}{\partial V} \right)_{T,N} \quad (3.0.1)$$

$$S = - \left( \frac{\partial F}{\partial T} \right)_{V,N} \quad (3.0.2)$$

$$\mu = \left( \frac{\partial F}{\partial N} \right)_{T,S} \quad (3.0.3)$$

$$U = -T^2 \frac{\partial}{\partial T} \left( \frac{F}{T} \right)_{V,N} \quad (3.0.4)$$

$$C_{V,P} = \left( \frac{\partial U}{\partial T} \right)_{V,P} \quad (3.0.5)$$

These thermodynamic properties give us a way of describing states of matter and provide predictions to experimental measurements. In honor of my adviser, the question shall

now be asked: What's the free energy of the system?

### 3.1 Saha's Equation - Dilute Theory

As a preface, the following derivation can be found in most statistical mechanics textbooks such as Reif [79], although the formalism presented is from Zel'dovich [106]. The free energy for an ideal (dilute) plasma is

$$F_{ideal} = - \sum_m N_m k_B T \left( \ln \frac{Z_m}{N_m} + 1 \right) - N_e k_B T \ln \left( \ln \frac{Z_e}{N_e} + 1 \right), \quad (3.1.1)$$

where  $N_m$  are the number of  $m$  ions,  $N_e$  is the number of electrons,  $k_B$  is the Boltzmann constant,  $T$  is the temperature, and  $Z_m$  and  $Z_e$  are the partition functions for the  $m$  ions and electrons respectively. In this notation,  $m = 0$  represents the neutral atoms,  $m = 1$  represents the singly-ionized atom, etc. Conservation of the number of atoms and charge requires

$$\sum_m N_m = N \quad (3.1.2)$$

$$\sum_m m N_m = N_e. \quad (3.1.3)$$

As a first application of the free energy, the ionization level can be derived, which is a statement of chemical potential equilibrium. At equilibrium, the free energy is minimized with respect to the particle number and results in the law of mass action given by

$$\frac{N_{m+1} N_e}{N_m} = \frac{Z_{m+1} Z_e}{Z_m}. \quad (3.1.4)$$

It is important to note that the law of mass action (Eq. (3.1.4)) is always applicable at equilibrium. In the ideal limit, the constituent particles are assumed to be non-interacting and the partition function becomes a product of its individual partition functions. The translational partition function for any particle is

$$Z_{trans} = \frac{V}{\lambda^3} \quad \lambda = \frac{h}{\sqrt{2\pi M k_B T}}. \quad (3.1.5)$$

Here,  $V$  is the volume,  $\lambda$  is the thermal de Broglie wavelength,  $M$  is the particle's mass, and  $h$  is Planck's constant. The electron's partition function is given by its translational partition function times a factor of 2 to account for its spin. For bound systems, such as atoms and ions, an electronic partition function is included along with the translational partition function. The electronic partition function is

$$Z_{el} = \sum_k g_k \exp\left(-\frac{\epsilon_k}{k_B T}\right), \quad (3.1.6)$$

where  $\epsilon_k$  is the energy of the  $k^{th}$  electronic quantum state. The electronic partition function can be rewritten to normalize to the ground state energy

$$\begin{aligned} Z_{el} &= \sum_k g_k \exp\left(-\frac{\epsilon_k}{k_B T}\right) = \exp\left(-\frac{\epsilon_0}{k_B T}\right) \sum_k g_k \exp\left(-\frac{\epsilon_k - \epsilon_0}{k_B T}\right) = u_k \exp\left(-\frac{\epsilon_0}{k_B T}\right) \\ u_k &= \sum_k g_k \exp\left(-\frac{\epsilon_k - \epsilon_0}{k_B T}\right) = g_0 + g_1 \exp\left(-\frac{\epsilon_1 - \epsilon_0}{k_B T}\right) + \dots, \end{aligned} \quad (3.1.7)$$

where  $\epsilon_0$  is the ground state energy and  $g_k$  are the statistical weights of the  $k^{th}$  energy level. Putting these partition functions into Eq. (3.1.4) results in

$$\frac{n_{m+1} n_e}{n_m} = 2 \frac{u_{m+1}}{u_m} \left( \frac{2\pi m_e k_B T}{h^2} \right)^{3/2} \exp\left(-\frac{\chi_{m+1}}{k_B T}\right), \quad (3.1.8)$$

where  $n$  are the number densities,  $m_e$  is the electron's mass, and  $\chi_{m+1}$  is the ionization potential to liberate the  $m+1$  bounded electron. Eq. (3.1.8) is known as Saha's equation. To readily calculate the amount of ionization, Saha's equation can be rewritten to give

$$\frac{x_{m+1} x_e}{x_m} = \frac{2}{n} \frac{u_{m+1}}{u_m} \left( \frac{2\pi m_e k_B T}{h^2} \right)^{3/2} \exp\left(-\frac{\chi_{m+1}}{k_B T}\right), \quad (3.1.9)$$

where  $x_m = \frac{n_m}{n}$  is the ionization fraction of the  $m^{th}$  ion. Using Eqs. (3.1.2), (3.1.3), and (3.1.9), the ionization level can be calculated knowing only the temperature, total atomic density, and atom-specific energy states. This equation has been the workhorse for estimating the electron density in plasma physics. However, as mentioned earlier, Saha's equation may only be applied to *dilute* systems whose constituent particles are weakly-interacting. It is this inappropriate use of Saha's equation that has generated

the blackbody paradox and, as will be shown in the next section, has led to the phase transition theory.

## 3.2 Saha’s Equation - Dense Theory

As the density increases and/or the temperature lowers, a plasma becomes less and less ideal, until it eventually becomes an SCP. In this regime, a plasma’s Coulomb energy is comparable or larger to its kinetic energy and Saha’s equation loses its validity. This is strictly due to the weakly-interacting assumption of the partition function, and therefore the free energy needs revision. A first principles derivation would begin with the Hamiltonian of the individual particles. The partition function of this system would involve many correlated interactions amongst all the particles, which has no known analytic solution. This system is also a daunting task numerically due to the factorial nature of the partition function and the long-range interaction of the Coulomb force. However, a key property of plasma is its tendency to shield out long range interactions through electrostatic screening. This was first treated by Debye and Hückel [21] for the case of electrolytes, which found an extension to plasma physics. In this analysis, a system of oppositely charged particles is considered where a cloud of similarly charged particles form around each ion/electron. This has the effect of screening the fields of ions/electrons at a characteristic distance known as the Debye length  $\delta_D$ . This screening effect, which is produced from particle correlations, provides a simplification to the system’s partition function and gives a formulation for the free energy.

The general expression for the Coulomb energy of a plasma per unit volume is given by

$$U_{coul} = \frac{1}{2} \sum_m eZ_m n_m \phi_m, \quad (3.2.1)$$

where  $eZ_m$  and  $n_m$  is the charge and density of the  $m^{th}$  ion, respectively. Electrons are included as an “ion” by setting  $m = -1$ .  $\phi_m$  is the potential of all other charges on the  $m^{th}$  ion. Using the Debye-Hückel model, the potential approximates to

$$\phi_m = -\frac{Z_m e}{\delta_D}, \quad (3.2.2)$$

where  $\delta_D$  is the Debye screening length given by

$$\delta_D = \left( \frac{4\pi e^2}{k_B T} \sum_m n_m Z_m^2 \right)^{-1/2}. \quad (3.2.3)$$

It is in this approximation that a characteristic length-scale is introduced which has the effect of lowering the free energy of the system. The free energy per unit volume for the Coulomb potential is found by substituting Eqs. (3.2.3) and (3.2.2) into Eq. (3.2.1), and applying the thermodynamic relationship Eq. (3.0.4) to give

$$F_{coul} = -\frac{(\sum_m n_m Z_m^2) e^2}{3\delta_D} = -\frac{k_B T}{12\pi\delta_D^3}. \quad (3.2.4)$$

The total free energy is additive and is given by

$$F = F_{ideal} + F_{coul}. \quad (3.2.5)$$

Minimization of Eq. (3.2.5) with respect to the particle number gives

$$\frac{x_{m+1}x_e}{x_m} = \frac{2}{n} \frac{u_{m+1}}{u_m} \left( \frac{2\pi m_e k_B T}{h^2} \right)^{3/2} \exp \left( -\frac{\chi_{eff}}{k_B T} \right), \quad (3.2.6)$$

where

$$\chi_{eff} = \chi_{m+1} - \Delta\chi_D \quad (3.2.7)$$

$$\Delta\chi_D = \frac{Z_{m+1}e^2}{\delta_d}. \quad (3.2.8)$$

As can be seen from Eq. (3.2.6), the density correction to the free energy produces a *lowering* of the ionization potential, which is the dominant term of Saha's equation. This can have an enormous effect on the level of ionization in a dense plasma, and therefore its thermodynamic properties.

Another density effect to consider is the quantum hybridization of excited energy levels. This is the lowering of the ionization potential to the binding energy of an excited atom, whose radius is equal to the interatomic spacing. The derivation of the free energy due to hybridization can be found in Zel'dovich (pg. 199, [106]). This free energy is similar in form to the Coulomb free energy and also results in a potential lowering given by

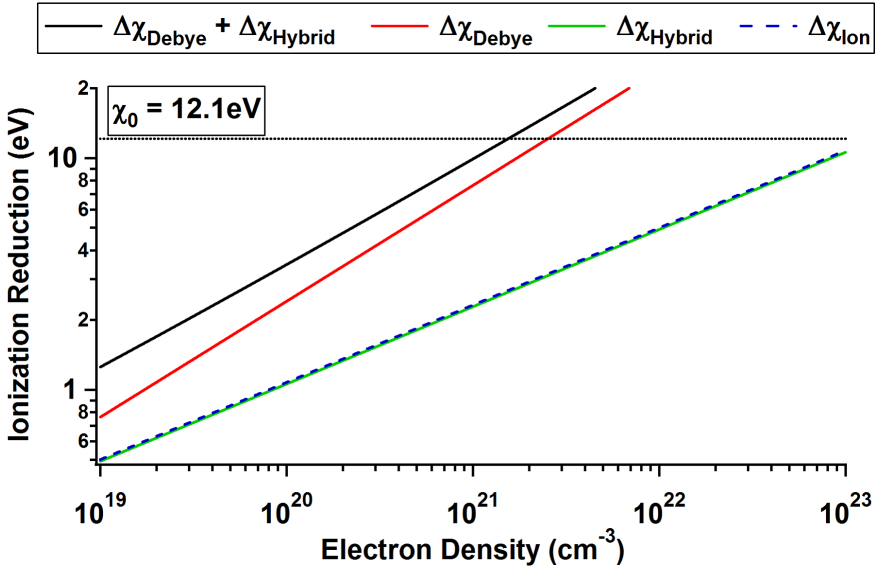


Figure 3.1: The ionization potential lowering from Debye screening and hybridization as a function of atomic density. Neutral xenon ( $m = 0$ ) is chosen, whose ionization potential is 12.1 eV and  $\gamma$  is 1.78 [57]. The temperature is taken at 15,000 K and a single level of ionization is assumed ( $n_e = n$ ).

$$\Delta\chi_{hyb} = 2\gamma a_0 n^{1/3} \chi_{m+1}, \quad (3.2.9)$$

where  $a_0$  is the Bohr radius and  $\gamma$  is an atom-specific coefficient on the order unity [57]. Like the potential lowering from Debye screening, Eq. (3.2.9) is subtracted from Eq. (3.2.7). The contributions and total amount of potential lowering as a function of density is shown in Fig. 3.1. In the density range of experimental interest, Debye screening has the largest contribution to the total potential lowering. However, the effects of hybridization is still important when calculating the total ionization level, as the effective ionization potential is inside an exponential. Fig. 3.1 also shows the limitations to the Debye-Hückel model, as the ionization potential and pressure will become negative at a critical density. Therefore, this model should be considered incomplete beyond a certain density. For purposes of calculation, the system should be considered fully ionized (for a given  $m$ ) when  $\chi_{eff} \leq 0$ .

A crucial assumption made in the Debye-Hückel model is that there are many electrons in the Debye sphere, where  $N_D = \frac{4\pi}{3} n \delta_D^3 \gg 1$ . This statement is comparable to  $\Gamma \ll 1$ ,

which is the dilute plasma limit and opposite to SL and SCP. It is not known how far the Debye-Hückel model extends into non-ideality. However, numerical results by Brush, Sahlin, and Teller [13] indicates a deviation from the effects of Debye screening by only 25% for the case of  $\Gamma \approx 1$ . Therefore, the experimental results presented in this thesis warrants comparison to the model of Debye screening.

Although Debye screening is not a first principles derivation, the Debye length is a natural plasma lengthscale from unit analysis. It is in this spirit that another lengthscale is chosen for the purposes of experimental comparison. The natural plasma lengthscale of interionic distance can replace  $\delta_D$  in Eq. (3.2.8) giving

$$\Delta\chi_{ion} = \frac{Z_{m+1}e^2}{a_m}, \quad (3.2.10)$$

where

$$a_m = \left( \frac{4\pi n_m}{3} \right)^{-1/3}. \quad (3.2.11)$$

The application of this lengthscale to the potential lowering is more commonly known as the ion-sphere model [84]. Comparing Eq. (3.2.10) to Eq. (3.2.9) shows these two quantities to be equivalent in the singly-ionized limit (Fig. 3.1). Therefore, the atom-specific coefficient  $\gamma$  will be calculated using the following relationship

$$\gamma = \frac{e^2}{2a_0\chi_{m+1}} \left( \frac{4\pi}{3} \right)^{1/3}. \quad (3.2.12)$$

The ionization level of an SCP can now be calculated using Eq. (3.2.6) for the following cases of  $\chi_{eff}$ :

1. Dilute model:  $\chi_{eff} = \chi_{m+1}$
2. Ion-sphere model:  $\chi_{eff} = \chi_{m+1} - \Delta\chi_{ion}$
3. Debye model:  $\chi_{eff} = \chi_{m+1} - \Delta\chi_D$

The dilute limit is unaffected by density effects and represents the lower limit of ionization, and is presented for purposes of comparison. The ion-sphere limit represents screening outside the interionic distance, and is considered an intermediate screening model. The Debye limit is strongly affected by screening well within the interionic distance, and is

considered the extreme screening model. It is important to note that most, if not all, work in the field of SCP acknowledges the effects of screening upon the lowering of the ionization potential. Furthermore, a phase transition to a highly-ionized plasma is also acknowledged by many authors [13, 84, 25, 57, 105], although the exact location of the transition in density-temperature space is not in consensus.

A surprising consequence of the application of Debye screening and the ion-sphere model is realized when attempting to solve Eq. (3.2.6). The density-corrected Saha's equation is now density dependent in the exponential term, which makes it a transcendental equation with the possibility of two real and positive solutions. The existence of two ionization solutions for a given density and temperature is a 1<sup>st</sup>-order phase transition. Fig. 3.2 plots the free energy per particle as a function of the ionization potential for the dilute, Debye, and ion-sphere models. For the dilute limit, only a single solution exists at any given temperature and density. Both the Debye and ion-sphere models exhibit 2 local minimum beyond a critical density for a given temperature. The critical density for the ion-sphere model is at solid densities for temperature near 1 eV. Theoretical work by Ebeling and Richert [25] found the critical density to be  $\sim 10^{22} \text{ cm}^{-3}$  using the ion-sphere model. The Debye model predicts a much lower critical density at  $\sim 10^{21} \text{ cm}^{-3}$  and is supported by recent experiments in SL [88, 57, 61, 56].

Recreating and confirming the SL phase transition outside its liquid confines requires a control and knowledge of the plasma temperature, atomic density, and a thermodynamic property (level of ionization, pressure, etc.). These plasma properties can be compared to the phase space for the models outlined in this chapter. Fig. 3.3 shows the ionization phase diagrams as a function of temperature and atomic density of xenon gas for the different screening models. In the “Dilute” model, changes in the ionization fraction are continuous and a 1<sup>st</sup>-order phase transition is absent. Both screening models (“ion-sphere” and “Debye”) exhibit a 1<sup>st</sup>-order phase transition as the atomic density reaches a critical value. This region is labeled “High Ionization” and is the region in phase space where two solutions exists according to Saha’s equation.

The phase diagram shown in Fig. 3.3 is a map to exploring the plasma phase transition as it provides a location in temperature and density for measuring high levels of ionization. This helps guide the experiments outlined in Chapters 7 and 8 by providing a range of

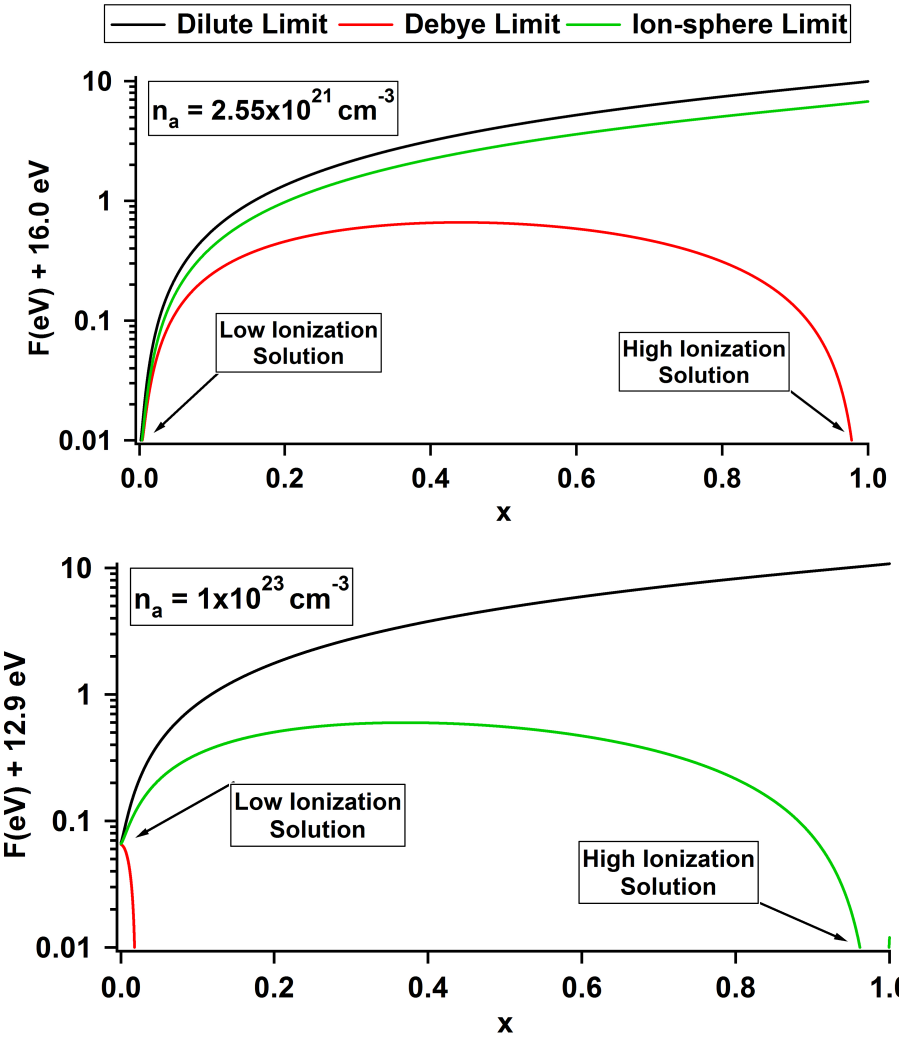


Figure 3.2: Total free energy per atom as a function of the ionization fraction in the singly-ionized regime. The gas is xenon with a plasma temperature of 10,000 K. The dilute limit has only one local minimum for all temperatures and densities. At 10,000 K, the plasma experiences two local minima at  $\sim 10^{21} \text{ cm}^{-3}$  for the Debye limit and  $\sim 10^{23} \text{ cm}^{-3}$  for the ion-sphere limit.

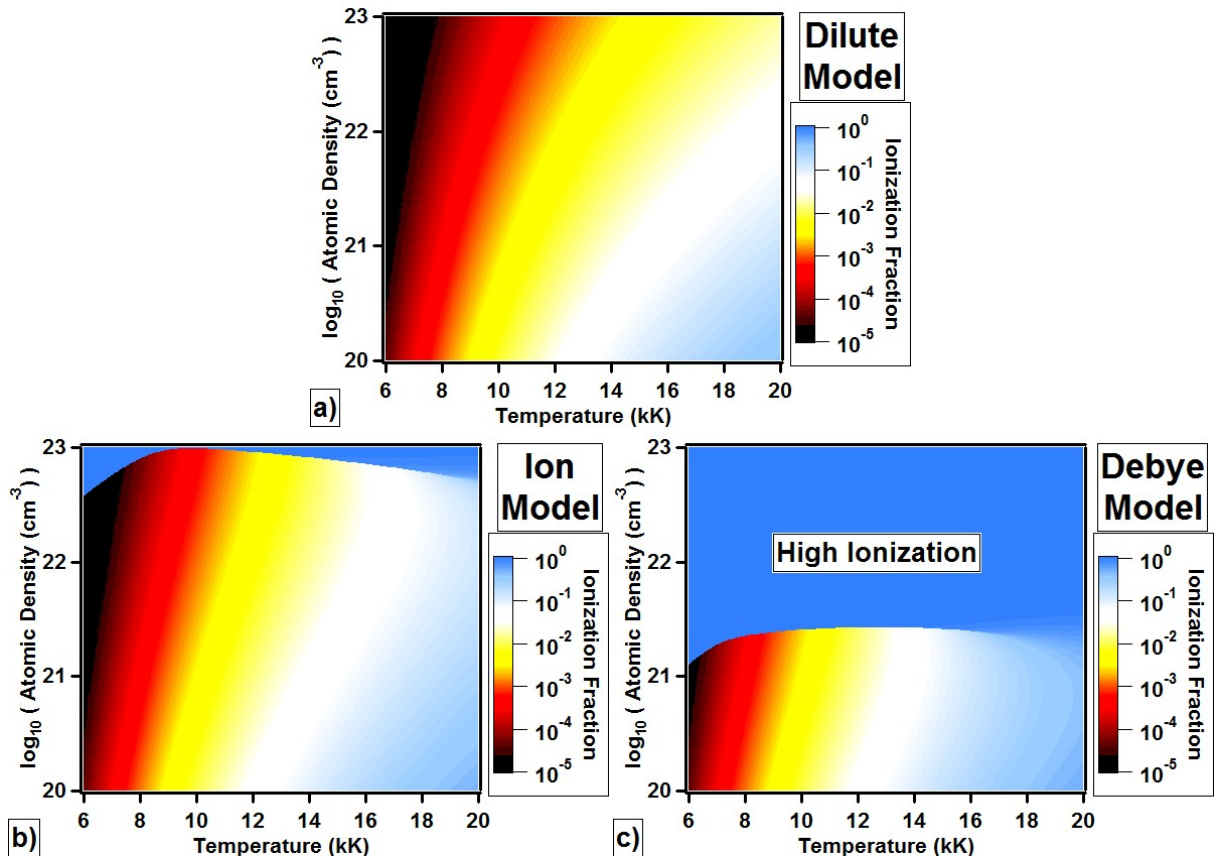


Figure 3.3: Phase diagram for xenon gas showing ionization fraction as a function of temperature and atomic density. The ionization fraction was calculated using the density-correct Saha's equation (Eq. 3.2.6) in the singly-ionized limit for the a) dilute model, the b) ion-sphere model, and the c) Debye model. Both the ion-sphere and Debye models contain an abrupt transition in ionization fraction as the atomic density is increased and is representative of a 1<sup>st</sup>-order phase transition. This transition occurs at  $\sim 10^{22} - 10^{23}$  for the ion-sphere model and  $\sim 10^{21}$  for the Debye model.

atomic densities needed to reach the phase transition. According to the “Debye” model, atomic densities on the order of  $\sim 10^{21} \text{ cm}^{-3}$  are required. This density equates to 40 bar of static pressure for a monatomic gas at room temperature and is the motivation for recreating the SL plasma outside a liquid. Furthermore, exploration of the parameter space in Fig. 3.3 will help identify the correct screening model in SCP.

In Chapter 7, laser breakdown in high-pressure gases can generate multiple levels of ionization, which is not described by the phase diagram in Fig. 3.3. For this reason, Eq. 3.2.6 must be solved for multiple ionization levels and is described in the following section.

### 3.3 Saha’s Equation - Multiple Ionization

Calculating the level of ionization requires solving the charge and ion conservation equations along with Saha (Eqs. 3.1.3, 3.1.2, and 3.2.6). For singly ionized systems, this represents a single transcendental equation and can be solved numerically with ease. However, for increasing levels of ionization, the system of equations becomes increasingly difficult to solve.

Saha’s equation with charge/ion conservation equations fully defines a plasma’s ionization level at equilibrium. For high levels of ionization, this becomes increasingly difficult to solve due to the increasing number of nonlinear transcendental equations. To overcome this complexity, Zaghloul *et. al* reformulated the Saha system of equations to produce a set of equations [105]. These equations are related through a recurrence formula and are easily solved for high levels of ionization. Saha’s equations reformulated by [105] are

$$1 - Z_{av} \left( \sum_{i=1}^Z \frac{i \prod_{j=1}^i f_j}{(Z_{av} n_H)^i} \right)^{-1} \left[ 1 + \sum_{i=1}^Z \frac{\prod_{j=1}^i f_j}{(Z_{av} n_H)^i} \right] = 0, \quad (3.3.1)$$

$$x_0 = Z_{av} \left( \sum_{i=1}^Z \frac{i \prod_{j=1}^i f_j}{(Z_{av} n_H)^i} \right)^{-1}, \quad (3.3.2)$$

$$x_{m+1} = \frac{x_m}{(Z_{av} n_H)} f_{m+1}, \quad (3.3.3)$$

where  $n_H$  is the nuclei density,  $Z_{av} = \sum_{m=1}^Z mx_m$  is the average ion charge, and  $f_{m+1}$  is the right-hand side of Saha's equation given by

$$f_{m+1} = 2 \frac{u_{m+1}}{u_m} \left( \frac{2\pi m_e k_B T}{h^2} \right)^{3/2} \exp \left( -\frac{\chi_{eff,m}}{k_B T} \right). \quad (3.3.4)$$

Eqs. 3.3.1-3.3.4 represent a complete set of equations which can be solved using an input plasma temperature, nuclei density, and atomic information (partition functions and ionization potential) to produce the level of ionization for each charge state. For the case of an ideal plasma ("Dilute" model), Saha's equation produces a singular solution. For the screened models,  $f_{m+1}$  becomes a function of the ionization level and an iterative solution is required. A procedure to find the ionization level using the "Debye" model is provided below:

1. Provide an initial guess for  $\delta_D$  and calculate  $\chi_{eff,m}$  using Eqs. 3.2.7 and 3.2.8.
2. Solve for  $Z_{av}$  in Eq. 3.3.1 using the results of step #1.
3. Solve for  $x_m$  in Eqs. 3.3.2 and 3.3.3 using  $Z_{av}$  in step #2.
4. Calculate  $\delta_D$  using the values of  $x_m$  in step #3 and Eq. 3.2.3.
5. Compare  $\delta_D$  from step #1 and step #4. Repeat steps #1-5 by adjust the input value of  $\delta_D$  in step #1 until convergence is reached.

Like the singly-ionized solutions in the preceding section, the possibility of two stable solutions is present in these calculations. Fig. 3.4 plots the solutions to Saha's equation in the multiply-ionized regime as a function of  $n_H$  for xenon at 12,350 K. Up to 8 levels of ionization are considered in Fig. 3.4. Both solutions converge at a critical density. Beyond this density, the solution to Saha's equation is highly-ionized as seen by [105]. Although two solutions exist at a given value of  $n_H$ , the low ionization solution is stable to perturbations indicated by the red arrows. However, once the high ionization solution is reached, perturbations to higher levels of ionization lead to a runaway electron density, as indicated by the blue arrows. This suggests that the total free energy in the "Debye" model is incomplete and is awaiting new physics! The gap between the two solutions represents

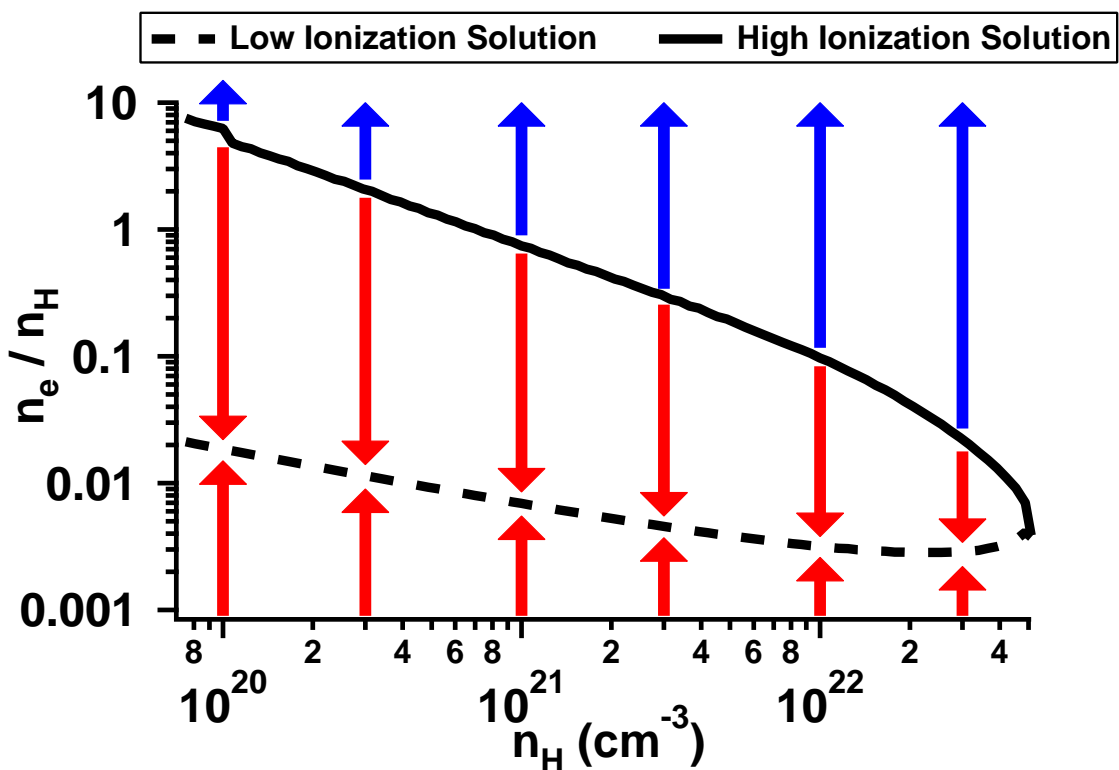


Figure 3.4: Solution to Saha's equation as a function of nuclei density for the case of xenon at 12,350 K. At each density there exists two solutions to Saha's equation defined by a low (dashed curve) and high (solid curve) level of ionization. The direction of stability is shown in red and blue curves.

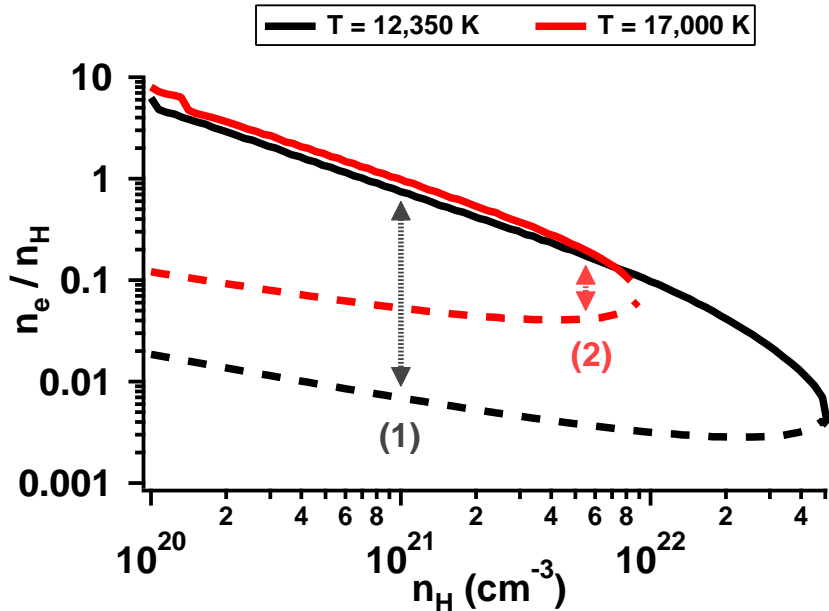


Figure 3.5: Solution to Saha’s equation as a function of nuclei density for the case of xenon at 12,350 and 17,000 K. At each density there exists two solutions to Saha’s equation defined by a low (dashed curve) and high (solid curve) level of ionization. Adiabatic compression (from density/temperature (1) to (2)) causes the distance between the two curves to shrink, and may be a possible method for reaching the phase transition in sonoluminescence.

an energy barrier for ionization. It has been suggested in [57, 59] that this gap can be overcome through density fluctuation. In SL, the adiabatic heating and compression of plasma decreases the gap distance and increases the probability of high ionization through fluctuations. An example of this gap decreasing with increasing temperature and density can be seen in Fig. 3.5.

The atomic and electronic densities of xenon SL in Chapters 5 and 6 ( $\sim 10^{21} \text{ cm}^{-3}$ ) suggest the “Debye” model of screening for calculating Saha’s equation. For the case of xenon SL in sulfuric acid, a collapse density of  $1.1 \times 10^{21} \text{ atoms/cm}^3$  and a plasma temperature of 8400 K was measured. Using these plasma parameters and the “Debye” theory of screening, Saha’s equation results in an electron density of  $> 5.0 \times 10^{20} \text{ cm}^{-3}$  ( $>45\%$ ) and a potential reduction of 81%. This result is consistent with the experiment performed in Chapter 5 as the inferred electron density is  $> 4.0 \times 10^{20} \text{ cm}^{-3}$  ( $>36\%$ ) and a potential reduction of 75%. For the case of xenon SL in water, a higher collapse

	Measured Values			
	$n_H$ (cm $^{-3}$ )	$T$ (K)	$n_e$ (cm $^{-3}$ )	$Z$
Xe Laser Breakdown	$1.25 \times 10^{20}$	12,350	$> 4.0 \times 10^{20}$	$> 3.2$
Xe Spark Discharge	$2.50 \times 10^{20}$	24,000	$> 8.0 \times 10^{20}$	$> 3.2$
Ar Laser Breakdown	$6.25 \times 10^{20}$	14,550	$> 6.25 \times 10^{20}$	$> 1.0$
Xe Sulfuric Acid SL	$1.1 \times 10^{21}$	8,400	$> 4.0 \times 10^{20}$	$> 0.36$
Xe Water SL	$4.9 \times 10^{21}$	9,250	$2 - 3 \times 10^{21}$	0.41 – 0.61

	Saha's, Low Solution		Saha's, High Solution	
	$n_e$ (cm $^{-3}$ )	$Z$	$n_e$ (cm $^{-3}$ )	$Z$
Xe Laser Breakdown	$2.1 \times 10^{18}$	0.017	$> 5.3 \times 10^{20}$	$> 4.3$
Xe Spark Discharge	$9.4 \times 10^{19}$	0.37	$> 9.2 \times 10^{20}$	$> 3.7$
Ar Laser Breakdown	$2.8 \times 10^{18}$	$4.4 \times 10^{-3}$	$> 2.8 \times 10^{20}$	$> 0.44$
Xe Sulfuric Acid SL	$3.0 \times 10^{17}$	$2.7 \times 10^{-4}$	$> 5.0 \times 10^{20}$	$> 0.45$
Xe Water SL	$1.7 \times 10^{18}$	$3.4 \times 10^{-4}$	$> 7.2 \times 10^{20}$	$> 0.15$

Table 3.1: Plasma parameters and calculated values of the ionization fraction for the plasmas explored in this thesis.

density of  $4.9 \times 10^{21}$  atoms/cm $^3$  and a plasma temperature of 9250 K was measured. Saha's equation results in an electron density of  $> 7.4 \times 10^{20}$  cm $^{-3}$  ( $> 15\%$ ). This result is consistent with the experiment performed in Chapter 6 as the inferred electron density is  $\sim 2 - 3 \times 10^{21}$  cm $^{-3}$  ( $\sim 50\%$ ).

The experiment performed in Chapter 7 represents a unique situation when compared to SL. In this experiment, a laser generates both heating and ionization in a short timescale of 100 fs. This condition leads to the possibility of multiple levels of ionization at very low atomic densities, yet consistent with the high ionization solution through Saha's equation. Using  $T = 12,350$  K for laser breakdown in 5 bar xenon (1.25 × 10 $^{20}$  atoms/cm $^3$ ), the solution to Saha's equation is  $n_e > 5.34 \times 10^{20}$  cm $^{-3}$  ( $\bar{Z} > 4.27$ ). This result compares very well to the measured electron density of  $n_e > 4.0 \times 10^{20}$  cm $^{-3}$  ( $\bar{Z} > 3.2$ )! The same analysis performed on 25 bar argon laser breakdown ( $T = 14,550$  K,  $n_H = 6.25 \times 10^{20}$  cm $^{-3}$ , and  $n_e > 6.25 \times 10^{20}$  cm $^{-3}$  ( $\bar{Z} > 1.0$ )) also compares well with a Saha solution of  $n_e > 2.76 \times 10^{20}$  cm $^{-3}$  ( $\bar{Z} > 0.44$ ). Finally, the plasma generated by the spark discharge experiment in Chapter 8 also displays a high level of ionization at relatively low atomic densities and is consistent with the solution to Saha's equation. The plasma values for all

plasmas explored in this thesis are compared to the results of Saha's equation and shown in Table 3.1. Remarkable agreement is found using the "Debye" theory of screening for a range of temperatures and densities and is strong evidence that the plasma generated in sonoluminescence is a universal phase of matter.

# Chapter 4

## Kinetic Theory

The plasma properties in Chapter 3 were derived under the condition of complete LTE. However, many situations arise where a plasma is generated or driven far off-equilibrium. In these situations, the relationships found on the basis of LTE no longer apply and kinetic theory is needed. Due to their high temperatures ( $\sim 10,000 - 20,000$  K) and densities, SCPs cannot exist for very long without destroying the surrounding chamber material. Therefore, laboratory SCPs are generated in pulsed operation and are inherently transient. The transient generation of SCPs means the possibility of off-equilibrium states and necessitates models using transport equations. In kinetic theory, transport equations describe materials that have been displaced from its equilibrium state and given enough time, will go back to equilibrium. These timescales/rates for equilibrium are important for many processes and are needed to describe the dynamic measurements of SCPs.

Kinetic theory is process-dependent and requires specific knowledge of the fundamental particle interactions. However, many plasma transport properties stem from the collisionality of electrons and ions. This is known as the electron-ion collision time  $\tau_{e-i}$  and is defined as the amount of time required for an electron to collide with an ion.  $\tau_{e-i}$  is ubiquitous in plasma physics and is at the core of many plasma processes which includes electron-ion bremsstrahlung, electron-ion thermalization, 3-body recombination/ionization, and thermal/electrical conductivity. Furthermore,  $\tau_{e-i}$  is an essential factor in the commonly used two-fluid plasma model as it describes the energy exchange between the different fluids (electrons and ions). This quantity has been determined for

the case of a fully-ionized plasma and is given as

$$\tau_{e-i} = \left[ \frac{2}{\sqrt{6\pi}} \omega_p \Gamma^{3/2} \ln \Lambda \right]^{-1}, \quad (4.0.1)$$

where  $\omega_p$  and  $\Gamma$  is the electron plasma frequency and plasma parameter respectively. These quantities are defined as

$$\omega_p \equiv \sqrt{\frac{4\pi \bar{Z} n_0 e^2}{m_e}}, \quad (4.0.2)$$

$$\Gamma \equiv \frac{\bar{Z} e^2}{k_B T} \left( \frac{4\pi n_0}{3} \right)^{1/3}, \quad (4.0.3)$$

where  $\bar{Z} = \frac{n_e}{n_0}$  is the effective ionization level, and  $n_e (n_0)$  is the electron(nuclei) density. For the case of  $\bar{Z} < 1$ ,  $\Gamma \equiv \frac{e^2}{k_B T} \left( \frac{4\pi \bar{Z} n_0}{3} \right)^{1/3}$ . Eq. 4.0.1 was first found by Spitzer [82] and subsequent derivations deviated by no more than a numerical factor of the order unity. A simplified derivation of Eq. 4.0.1 taken from [106] is provided in Appendix A.

In Eq. 4.0.1, a new term was introduced into plasma physics known as the Coulomb logarithm,  $\ln \Lambda$ . This term arises due to two fundamental characteristics of plasma: (i) the long-range potential between charged particles and (ii) the effects of electrostatic screening. In deriving Eq. 4.0.1, an integration in radius over all possible “collisions” results in a logarithmically divergent integral and an infinitely fast collision time. This divergence is due to the character of the long-range Coulomb potential as distant collisions, although small in effect, become infinite in number. However, the effects of electrostatic screening (discussed in Chapter 3) shields-out these long-range interactions and thereby making Eq. 4.0.1 convergent. In this derivation, Spitzer chose the Debye length as the characteristic screening distance, thereby defining the Coulomb logarithm as

$$\ln \Lambda \equiv \ln \frac{\delta_D}{R_c}, \quad (4.0.4)$$

where  $\delta_D$  is the Debye length (Eq. 3.2.3) and  $R_c \equiv \frac{\bar{Z} e^2}{k_B T}$  is the distance of closest approach, the distance at which the electrostatic and kinetic energies are equal and energy transfer is largest. Eq. 4.0.4 can be written using the plasma parameter such that

$$\ln \Lambda = \ln \left( \frac{\Gamma^{-3/2}}{\sqrt{3(1 + \bar{Z})}} \right). \quad (4.0.5)$$

Because the collision time depends logarithmically on the screening effects, a common practice in plasma physics is to set the Coulomb logarithm as a numerical constant. This will be referred to as the “Dilute Theory” of plasma where screening effects are ignored.

Application of Eq. 4.0.1 with Eq. 4.0.4 has been very successful in describing *dilute* plasma physics, as the Coulomb logarithm is a weak function of the plasma parameters ( $T$  and  $n_0$ ). However, trouble arises as  $\Gamma$  increases and the plasma becomes non-ideal. Indeed, Eq. 4.0.4 becomes ill-defined in dense plasma when  $\delta_D < R_c$ . To account for the increased screening effects in SCPs, various authors have put forth modified forms of the Coulomb logarithm which can vary significantly. For the purpose of comparison, three forms of the Coulomb logarithm are chosen for the experiments presented. They are:

$$\text{"Dilute"} : \quad \ln \Lambda = 1, \quad (4.0.6a)$$

$$\text{"Daligault"} : \quad \ln \Lambda = \ln (0.7\Lambda + 1), \quad (4.0.6b)$$

$$\text{"Debye"} : \quad \ln \Lambda = \ln \sqrt{\Lambda^2 + 1}. \quad (4.0.6c)$$

The “Dilute” theory represents one extreme where screening is not considered. Conversely, the “Debye” theory represents the extreme in screening where collisions only occur within the Debye length. The “Daligault” theory [22] represents an intermediate screening theory and is similar to that of the “ion-sphere” model presented in Chapter 3 (see Appendix B).

The transport properties observed in the thesis experiments presented relate directly to  $\tau_{e-i}$ . Specifically, the plasma opacity through the rate of (inverse) bremsstrahlung, the thermalization timescale needed for thermal equilibrium, and the electron-ion recombination timescale needed for ionization equilibrium are considered and their derivations are shown in the following sections.

## 4.1 Inverse Bremsstrahlung

A defining characteristic of sonoluminescence is its opaque nature in the visible frequencies. Blackbody spectra emerging from a micron-sized plasma is a strong indication of the phase transition discovered by Kappus et al. [57]. To be opaque, a body must satisfy the following conditions: (i) light and matter are in thermodynamic equilibrium

and (ii) the photon mean-free-path is much smaller than the radiating body. The second condition can be rewritten as  $\kappa l_{BB} \gg 1$ , where  $l_{BB}$  is the size of the blackbody and  $\kappa$  is a process-dependent absorption coefficient for light. The processes that result in the absorption of continuous spectra is the scattering of an electron with an ion(atom) known as free-free(free-neutral) inverse bremsstrahlung, and the ionizing absorption of a bound electron by a photon known as free-bound absorption (photoionization). For the plasma temperatures and densities under consideration in this thesis, free-free inverse bremsstrahlung is the dominant mechanism for absorption [59]. With the knowledge of this absorption coefficient  $\kappa_{e-i}$  and the plasma size, one can determine the electron density needed for opacity. Considering the mechanism for free-free inverse bremsstrahlung, it should come as no surprise that  $\kappa_{e-i}$  is fundamentally dependent upon  $\tau_{e-i}$ .

A full derivation of  $\kappa_{e-i}$  based on the Drude model can be found in Appendix C and the results are given below using the “Daligault” theory:

$$\kappa_{e-i} = 2\Im(k_p), \quad (4.1.1)$$

$$k_p^2 = \frac{\omega^2}{c^2} \left[ (1 - \gamma\beta) + \frac{\gamma\beta}{\omega\tau_\omega} i \right], \quad (4.1.2)$$

$$\omega\tau_\omega = \left[ \frac{2}{\sqrt{6\pi}} \gamma^{1/2} \Gamma^{1/2} \Gamma_\omega \ln \left( \frac{0.7}{\sqrt{3}} \Gamma_\omega^{-3/2} + 1 \right) \right]^{-1}, \quad (4.1.3)$$

$$\gamma = \left( \frac{\omega_p}{\omega} \right)^2 = \frac{4\pi n_0 \bar{Z} e^2}{m_e \omega^2}, \quad \beta = \frac{\omega^2 \tau_\omega^2}{1 + \omega^2 \tau_\omega^2}, \quad \Gamma = \left( \frac{\bar{Z} e^2}{k_B T} \right) \left( \frac{4\pi n_0}{3} \right)^{1/3},$$

$$\Gamma_\omega = \Gamma \left[ \frac{k_B T}{\hbar\omega} \left( 1 - \exp \left( -\frac{\hbar\omega}{k_B T} \right) \right) \right],$$

where  $\tau_\omega$  is the electron-ion collision time in the presence of an electromagnetic field oscillating at  $\omega$ . In the limit of  $\hbar\omega \rightarrow 0$ ,  $\tau_\omega \rightarrow \tau_{e-i}$ . Although lengthy in appearance, the above equations greatly simplify as many of the experimental plasmas presented fall within a certain regime. In the limit of  $\omega\tau_\omega$ ,  $\frac{k_B T}{\hbar\omega}$ ,  $\frac{\omega}{\omega_p} \gg 1$  and  $\Gamma \gtrsim 1$ ,  $\omega\tau_\omega \simeq 5.37\gamma^{-1/2}$  and  $\kappa \simeq 1.17\frac{\gamma^{3/2}}{\lambda}$ , where  $\lambda$  is the wavelength of light. This is a result that is unique in plasmas as  $\tau_{e-i}$  and  $\kappa_{e-i}$  become independent of temperature and scale only with the plasma frequency.

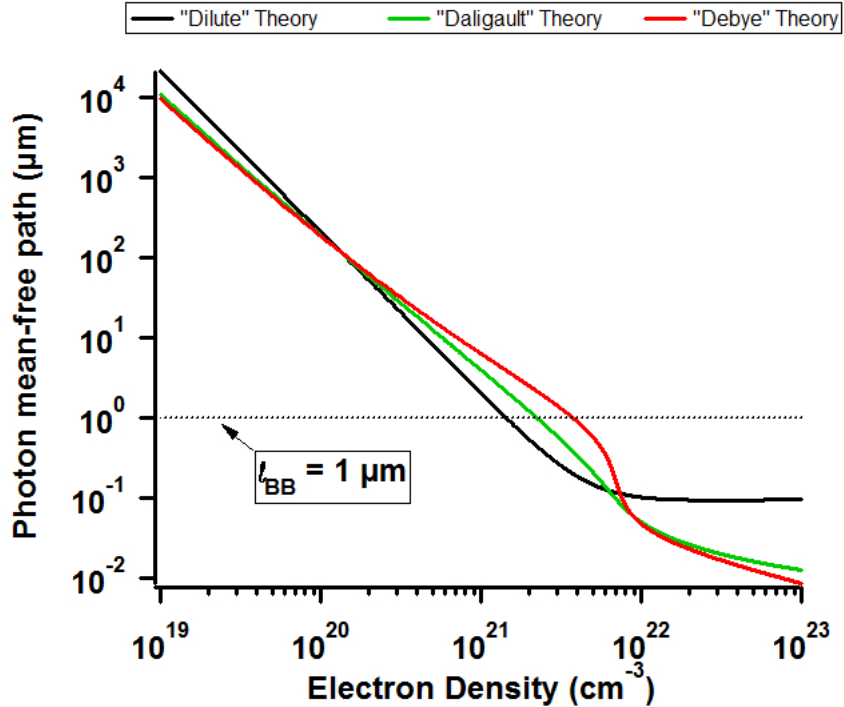


Figure 4.1: The photon mean free path ( $\kappa_{e-i}^{-1}$ ) in a plasma vs. electron density for various screening theories. The frequency of light and plasma temperature is 400 nm and 10,000 K respectively. Opacity at 400 nm can only occur in micron-sized plasma with electron densities  $> 10^{20} \text{ cm}^{-3}$ , assuming free-free as the dominant mechanism.

The formulas presented above allow not only the absorption of light in a plasma, but also the *reflection* of light by a plasma. As a simple example (and used in Chapter 6), the reflection of a plane wave incident a semi-infinite plasma slab is given by

$$R = \left| \frac{n_p - n_0}{n_p + n_0} \right|^2, \quad (4.1.4)$$

where  $n_p = \frac{k_p c}{\omega}$  is the plasma index of refraction and  $n_0$  is the index of refraction of the adjacent medium. Using the equations above, the plasma opacity ( $\kappa_{e-i}$ ), the collision time ( $\omega\tau_\omega$ ), and the reflection ( $R$ ) can be compared with the different screening theories and are shown in Figs. 4.1-4.3 as a function of the electron density. The opacity calculations presented here are applied to the blackbody plasmas seen in Chapters 5-8. Knowing the size of the plasma and its blackbody temperature, the electron density can be inferred from the opacity condition set by  $\kappa_{e-i}$  and use of the appropriate Coulomb logarithm. It

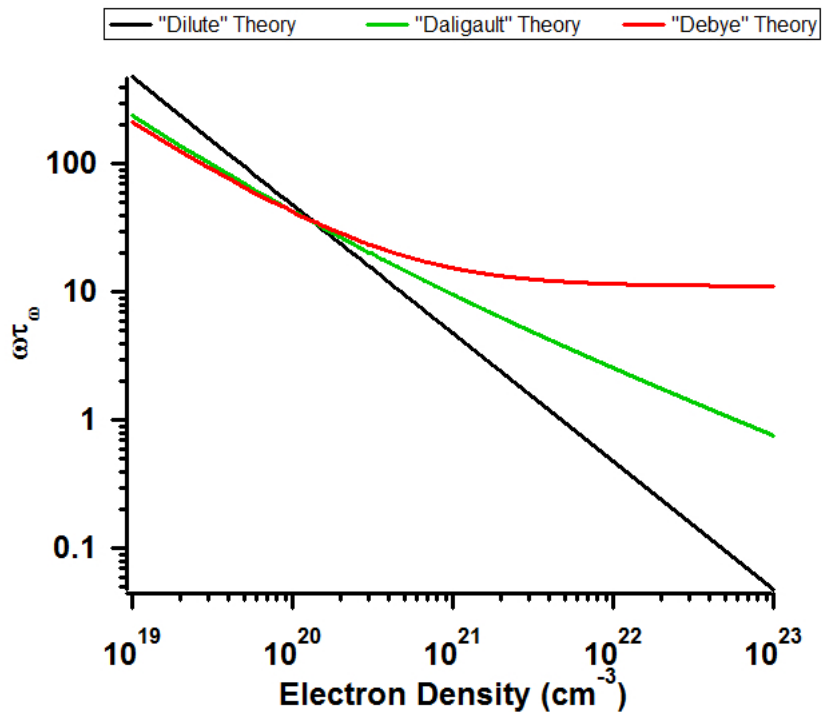


Figure 4.2:  $\omega\tau_\omega$  in a plasma vs. electron density for various screening theories. The frequency of light and plasma temperature is 400 nm and 10,000 K respectively. The collision frequency increases with the electron density and can reach levels near the frequency of light for the “Dilute” and “Daligault” screening theories. The “Daligault” theory predicts a the collision frequency scaling proportionally to the plasma frequency at large electron densities. The most extreme screening model (“Debye”) predicts a saturation in the collision frequency for electron densities  $> 10^{21} \text{ cm}^{-3}$ .

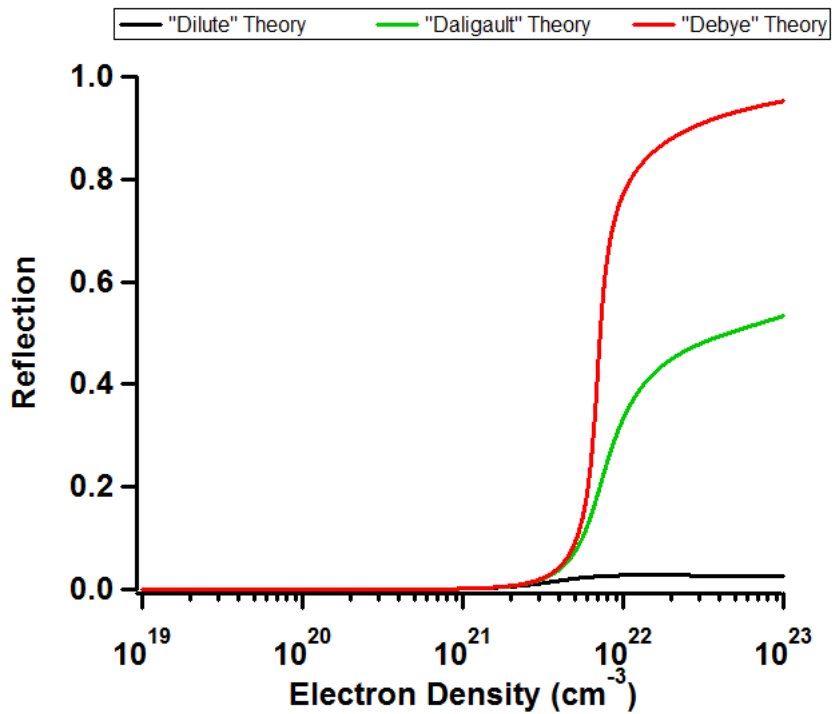


Figure 4.3: The reflection of a plane wave incident a semi-infinite plasma slab vs. electron density for various screening theories. The frequency of light and plasma temperature is 400 nm and 10,000 K respectively. The reflection of the incident wave increases slowly with the electron density. A sharp increase in reflection occurs for densities greater than the critical density ( $\omega = \omega_p$ ) for the screened theories (“Daligault” and “Debye”). In the “Dilute” theory, strong reflection is hindered as the wave is damped by the  $\omega\tau_\omega \lesssim 1$  effect.

will be shown in Chapter 6 (through plasma reflection ( $R$ )) that the “Daligault” theory of screening is the correct form in the density range under consideration.

## 4.2 Thermalization Time

As a plasma consists of ions and electrons, there exists the possibility of a two-temperature system defined by the electron temperature  $T_e$  and the ion temperature  $T_i$ . Therefore, there are several collision timescales for reaching thermal equilibrium in a plasma: (i) the electron-electron  $\tau_{e-e}$ , (ii) ion-ion  $\tau_{i-i}$ , and (iii) electron-ion  $\tau_{e-i}$  collision timescales given by

$$\tau_{e-e} = \left[ \frac{2}{\sqrt{6\pi}} \omega_{p,e} \Gamma_{ee}^{3/2} \ln \Lambda_{ee} \right]^{-1}, \quad \omega_{p,e} = \sqrt{\frac{4\pi n_e e^2}{m_e}}, \quad \Gamma_{ee} = \frac{e^2}{k_B T} \left( \frac{4\pi n_e}{3} \right)^{1/3}, \quad (4.2.1)$$

$$\tau_{i-i} = \left[ \frac{2}{\sqrt{6\pi}} \omega_{p,i} \Gamma_{ii}^{3/2} \ln \Lambda_{ii} \right]^{-1}, \quad \omega_{p,i} = \sqrt{\frac{4\pi n_i e^2}{M}}, \quad \Gamma_{ii} = \frac{\bar{Z}^2 e^2}{k_B T} \left( \frac{4\pi n_i}{3} \right)^{1/3}, \quad (4.2.2)$$

$$\tau_{e-i} = \left[ \frac{2}{\sqrt{6\pi}} \omega_{p,e} \Gamma_{ei}^{3/2} \ln \Lambda_{ei} \right]^{-1}, \quad \omega_{p,e} = \sqrt{\frac{4\pi n_e e^2}{m_e}}, \quad \Gamma_{ei} = \frac{\bar{Z} e^2}{k_B T} \left( \frac{4\pi n_i}{3} \right)^{1/3}. \quad (4.2.3)$$

The timescale for *thermal equilibrium* is mass dependent given by

$$\tau_{th,a-b} \approx \frac{m_b}{m_a} \tau_{a-b}, \quad (4.2.4)$$

where  $m_{a(b)}$  is the mass for particle  $a$  ( $b$ ). For particles of the same mass, thermal equilibrium is established in only a few collisions (electron-electron and ion-ion) while many collisions are needed for particles of different mass (electron-ion). Comparing the thermalization timescales (Eqs. 4.2.1-4.2.4) normalized to  $\tau_{e-e}$  gives

$$\text{Singly-Ionized: } \tau_{th,e-e} : \tau_{th,i-i} : \tau_{th,e-i} = 1 : \sqrt{\frac{M}{m_e}} : \frac{M}{m_e}, \quad (4.2.5)$$

$$\text{Multiply-Ionized: } \tau_{th,e-e} : \tau_{th,i-i} : \tau_{th,e-i} = 1 : \left( \frac{\ln \Lambda_{ii}}{\bar{Z}^2 \ln \Lambda_{ee}} \right) \sqrt{\frac{M}{m_e}} : \left( \frac{\ln \Lambda_{ei}}{\bar{Z} \ln \Lambda_{ee}} \right) \frac{M}{m_e}, \quad (4.2.6)$$

where  $M$  is the mass of the ions. Tables 4.1 and 4.2 show the calculated timescales in Eqs. 4.2.5 and 4.2.6 for the various screening theories. The plasma properties of xenon and argon laser breakdown in Chapter 7 are used for comparing the singly vs. multiply-ionized

	$\tau_{th,e-e}$ (fs)	$\tau_{th,i-i}$ (ps)	$\tau_{th,e-i}$ (ns)
“Dilute”	0.773	0.209	0.0563
“Daligault”	4.18	1.13	<b>0.305</b>
“Debye”	19.2	5.17	1.39

Table 4.1: Calculated values of the thermalization times between electrons, ions, and electrons with ions. Plasma values ( $T=14,550$  K and  $\bar{Z} = 1.0$ ) for laser breakdown in 25 bar argon from Chapter 7 were used to calculate the thermalization times for various screening theories. The measured value for  $\tau_{th,e-i}$  is 380 ps, which most closely follows the “Daligault” theory.

	$\tau_{th,e-e}$ (fs)	$\tau_{th,i-i}$ (ps)	$\tau_{th,e-i}$ (ns)
“Dilute”	0.944	0.045	0.0706
“Daligault”	5.22	4.19	<b>1.17</b>
“Debye”	24.5	377	18.1

Table 4.2: Calculated values of the thermalization times between electrons, ions, and electrons with ions. Plasma values ( $T=12,350$  K and  $\bar{Z} = 3.2$ ) for laser breakdown in 5 bar xenon from Chapter 7 were used to calculate the thermalization times for various screening theories. The measured value for  $\tau_{th,e-i}$  is 1.47 ns, which most closely follows the “Daligault” theory.

regimes. The *measured* values of  $\tau_{th,e-i}$  from Chapter 7 leans in favor of the screening theory of “Daligault” as highlighted in red. Furthermore, both  $T_e$  and  $T_i$  are established in timescales on the order of femtoseconds and picoseconds, respectively. Therefore, from an experimental standpoint, the plasma generated in Chapter 7 is a two-temperature plasma whose physics obeys the two-fluid model.

### 4.3 Recombination Time

As discussed in Chapter 3, the ionization level of a plasma in equilibrium is governed by Saha’s equation. In certain situations, a plasma’s ionization level can be driven or generated off its equilibrium value (ionizing shock waves, ultra-fast laser ionization, etc.). A plasma whose ionization is off its equilibrium value will seek the Saha determined value with a characteristic recombination timescale  $\tau_{rec}$ . Once a plasma has reached its Saha determined value, the plasma is in a state of *ionization equilibrium*.

The dominant process for electron recombination in high density plasmas is the 3-body recombination, which occurs from the capture of an electron by an ion in the presence of an additional electron. The reverse process to 3-body recombination is called electron impact ionization, which occurs from the impact of an electron and an ion resulting in two free electrons. Both of these processes are useful in determining if a plasma is in ionization equilibrium, and are related to each other through Saha's equation by the principle of detailed balance. For the experiment presented in Chapter 7,  $\tau_{rec}$  is a crucial timescale in determining the plasma's equation of state. The elementary theory of 3-body recombination is provided by [106] and is given as

$$\tau_{rec} = \left( \bar{v}_e \pi^2 r_0^5 \bar{Z}^4 n_0^2 \right)^{-1}, \quad (4.3.1)$$

where  $\bar{v}_e = \sqrt{8k_B T / m_e \pi}$  is the mean thermal electron speed and  $r_0 = \frac{2e^2}{3k_B T}$  is the impact parameter for recombination in a Coulomb collision. Eq. 4.3.1 is derived by multiplying the frequency of electron-ion collisions ( $\tau_{e-i}^{-1}$ ) with the probability ( $P$ ) of finding an additional electron within the collision region, as needed to conserve energy and momentum. Separating Eq. 4.3.1 into these two factors gives

$$\tau_{rec} = \left( \bar{v}_e \pi (\bar{Z} r_0)^2 n_0 \right)^{-1} \times \left( \pi (\bar{Z} r_0)^2 r_0 n_0 \right)^{-1} = \frac{\tau_{e-i}}{P}. \quad (4.3.2)$$

This formulation of  $\tau_{rec}$  does not take into consideration the screening effects of dense plasma and can be considered the "Dilute" theory. To account for screening effects,  $r_0$  is replaced with the screened impact parameter  $\rho$  given by  $\sigma = \pi \rho^2 = (\bar{Z} n_0 \bar{v}_e \tau_{e-i})^{-1}$ , where  $\tau_{e-i}$  is the electron-ion collision time for various screening theories. In the high-density limit:

$$\text{"Dilute": } \rho \approx \left( \frac{2}{3} \right)^{1/2} R_c, \quad (4.3.3a)$$

$$\text{"Dalgarno": } \rho \approx \left( \frac{1.4}{9} \right)^{1/2} \left( \frac{a}{\delta_D} \right)^{1/2} a, \quad (4.3.3b)$$

$$\text{"Debye": } \rho \approx \left( \frac{1}{3} \right)^{1/2} \delta_D, \quad (4.3.3c)$$

where  $a$  and  $\delta_D$  are given by Eqs. 3.2.11 and 3.2.3 respectively. Formulation for the screened impact parameters can be found in Appendix B.  $\tau_{e-i}$ ,  $P$ , and  $\tau_{rec}$  are calculated

	$\tau_{e-i}$ (fs)	$P$	$\tau_{rec}$
“Dilute”	0.773	162%	0.477 fs
“Daligault”	3.81	14.8%	25.7 fs
“Debye”	18.4	1.39%	1.32 ps

Table 4.3: Calculated values for the 3-body recombination timescale. Plasma values ( $T=14,550$  K and  $\bar{Z} = 1.0$ ) for laser breakdown in 25 bar argon from Chapter 7 were used to calculate  $\rho$  for various screening theories.

	$\tau_{e-i}$ (fs)	$P$	$\tau_{rec}$
“Dilute”	0.295	542%	0.0544 fs
“Daligault”	4.76	8.37%	56.9 fs
“Debye”	75.3	1.36%	5.52 ps

Table 4.4: Calculated values for the 3-body recombination timescale. Plasma values ( $T=12,350$  K and  $\bar{Z} = 3.2$ ) for laser breakdown in 5 bar xenon from Chapter 7 were used to calculate  $\rho$  for various screening theories.

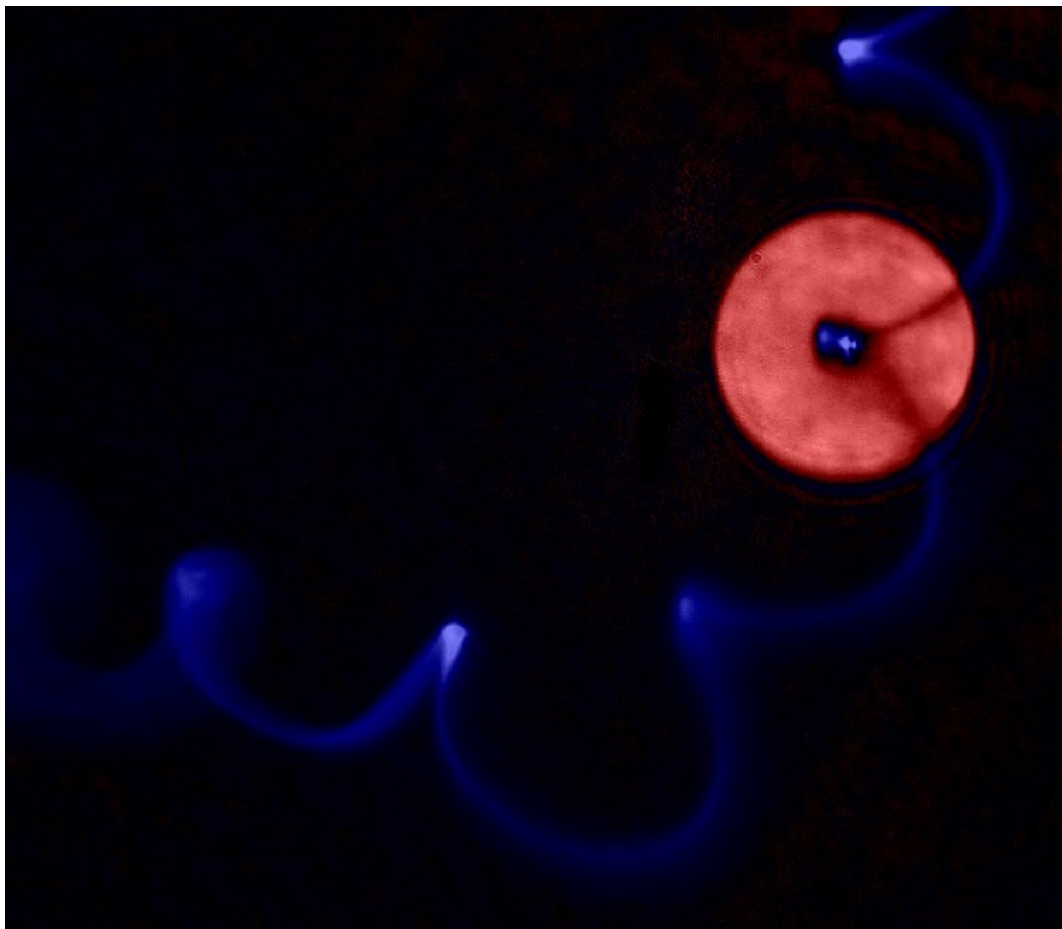
	$\tau_{e-i}$ (fs)	$P$	$\tau_{rec}$
“Dilute”	0.099	2500%	0.004 fs
“Daligault”	1.91	29.3%	6.52 fs
“Debye”	36.3	0.355%	10.2 ps

Table 4.5: Calculated values for the 3-body recombination timescale. Plasma values ( $T=9,250$  K and  $\bar{Z} \approx 0.45$ ) for the xenon SL ( $n_0 = 5.5 \times 10^{21} \text{ cm}^{-3}$ ) from Chapter 6 were used to calculate  $\rho$  for various screening theories.

in Tables 4.3 and 4.4 for the various screening theories. The plasma properties of xenon and argon laser breakdown in Chapter 7 are used in Tables 4.3 and 4.4. For comparison to a high density system, the plasma properties of xenon SL in Chapter 6 are used in Table 4.5. For all plasmas considered, the “Dilute” theory predicts an impossibly fast timescale due to an overestimation of  $P$ . The “Daligault” theory of recombination predicts  $\tau_{rec}$  on the order of  $\tau_{e-i}$ . It is important to recognize that *ALL* screening models predict  $\tau_{rec} < 10$  ps. Therefore, all plasmas measured in this thesis are in ionization equilibrium and must obey Saha’s equation.

# Chapter 5

## Sulfuric Acid Sonoluminescence



## 5.1 Introduction<sup>1</sup>

A big challenge in the field of SL has been the experimental limitations in measuring the submicron and subnanosecond bubble dynamics. The discovery of the plasma phase transition was made possible by the existence of a  $\sim 100 \mu\text{m}$  and  $\sim 1 \mu\text{s}$  SL plasma [57]. However, there does exist an SL bubble whose dynamics lie between these two extremes ( $\sim 10 \mu\text{m}$  and  $\sim 10 \text{ ns}$ ) known as “Sulfuric Acid Sonoluminescence”. The size and timescale of this SL allows one to measure its bubble dynamics with a high degree of accuracy. This provided the key motivation for verifying the plasma phase transition in the following experiment. Furthermore, this experiment provides a new approach to verifying the plasma phase transition through energy conservation. The result of this experiment is a verification of the plasma phase transition in a new SL system, whose degree of ionization and potential reduction is consistent with Debye screening of a strongly-coupled plasma (see Chapter 3).

---

<sup>1</sup>Chapter Image: A false-color microscope photograph of xenon SL dancing in sulfuric acid. The photograph was backlit with a single 100 fs laser pulse at the moment of maximum bubble radius, as seen by the large red circle. The blue corkscrew appearing across the image is created from thousands of bubble collapses, each producing SL emission. The relatively long exposure time (100s ms) and change in every collapse position provides the appearance of a continuous stream of light.

## 5.2 Energy Balance for a Sonoluminescence Bubble Yields a Measure of Ionization Potential Lowering

Application of energy conservation between input sound and the microplasma which forms at the moment of sonoluminescence places bounds on the process, whereby the gas is ionized. Detailed pulsed Mie scattering measurements of the radius versus time for a xenon bubble in sulfuric acid provide a complete characterization of the hydrodynamics and minimum radius. For a range of emission intensities, the blackbody spectrum emitted during collapse matches the minimum bubble radius, implying opaque conditions are attained. This requires a degree of ionization  $>36\%$ . Analysis reveals only  $2.1 \pm 0.6$  eV/atom of energy available during light emission. In order to unbind enough charge, collective processes must therefore reduce the ionization potential by at least 75%. We interpret this as evidence that a phase transition to a highly-ionized plasma is occurring during sonoluminescence.

Sonoluminescence (SL) is the emission of light from a bubble whose pulsations are so strong that the energy density of a surrounding sound field is concentrated by many orders of magnitude. This can be achieved in cavitation clouds [31, 69, 100] or in a single driven cavity[100, 90, 99, 6, 85, 15, 32, 18, 88]. Fig. 5.1 shows how a single spherical bubble of xenon in sulfuric acid expands to a maximum radius  $R_m$  during the rarefaction part of a 28.5 kHz standing wave and then rapidly collapses to a minimum radius  $R_c$  during the ensuing compression. For this example of sonoluminescence the flash of light emitted at  $R_c$  has a 13 nanosecond duration and its spectroscopy (Fig. 5.2) reveals an accurate match to an ideal Planck blackbody [48]. A blackbody must be opaque and so the mean free path  $l$  of light inside the light-emitting-region must be smaller than its size, or to the accuracy of our measurements,  $l < R_c$ . As SL originates in a plasma, the charge density required for opacity for this  $6.5 \pm 0.9 \mu\text{m}$  radius bubble is  $n_e > 4.0 \times 10^{20} / \text{cm}^3$  fundamental unbound charges/cc, or  $N_e > 4\pi R_c^3 n_e / 3$  unbound charges in the blackbody [106, 39]. In order to independently produce  $N_e$  free ions, the plasma requires an energy  $N_e \chi_0$  where  $\chi_0$  ( 12.1 eV) is the ionization potential of a single xenon atom. Via a detailed

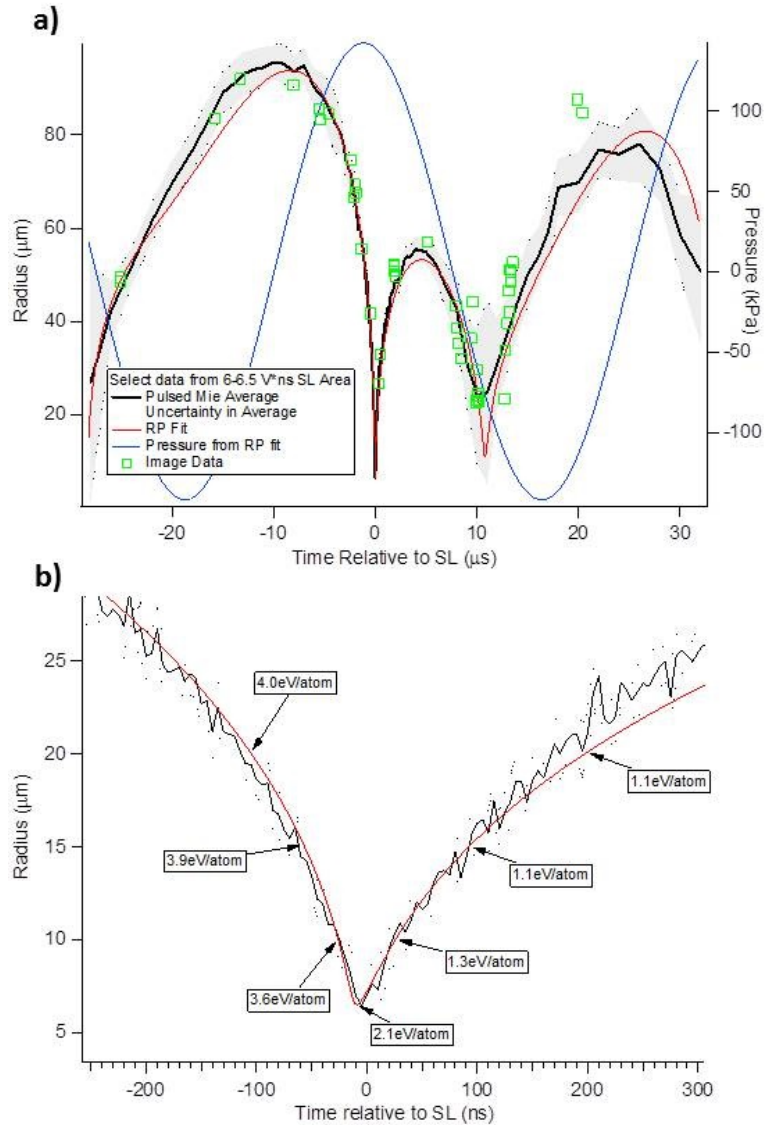


Figure 5.1: Radius versus time from Mie scattering data, backlighting image data, and RP simulation fit in sulfuric acid from flashes between 6 and 6.5 V ns integrated intensity. (a) illustrates bubble motion for just over one cycle of the sound field. (b) shows the same data scaled to reveal details of near the minimum radius and includes points of reference to delineate energy availability at various points on the curve. Uncertainty is calculated as the standard deviation of the Mie scattering points from a given time-grouping added in quadrature with the predicted velocity multiplied by the width of the grouping.

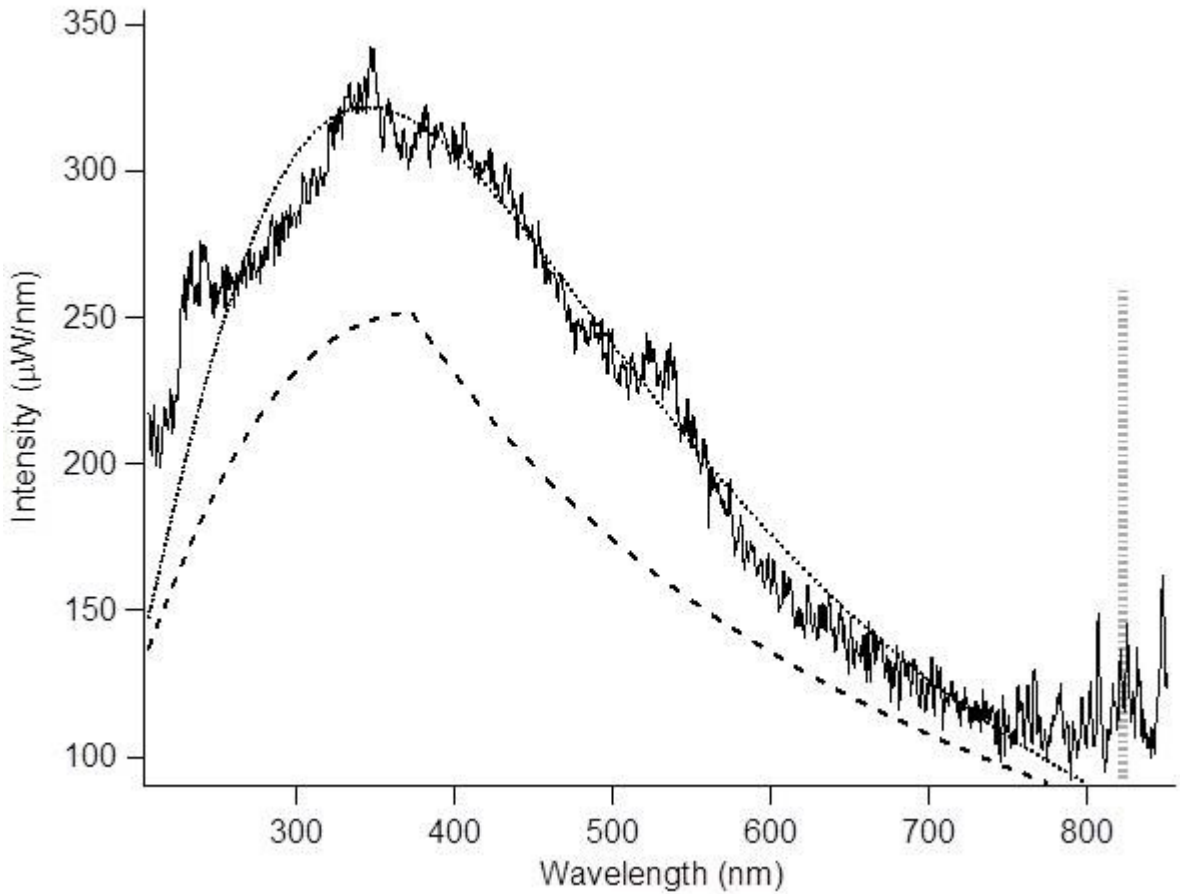


Figure 5.2: Integrated spectrum from sonoluminescence in sulfuric acid from flashes between -6 and -6.5 V ns integrated intensity. The dotted line is a fit (from 250 to 800 nm) to a Planck black body which gives  $T = 8400$  K and  $R_e = 6.9 \mu\text{m}$ . The dashed line is a theoretical transparent spectrum following Hammer *et al* [41]. This model uses a fixed size of  $6.5 \mu\text{m}$  radius, a temperature of 15900 K, and 5.4% ionization (The upper limit of our uncertainty in both temperature and density of the SL plasma). The associated 823 nm line emission for this hot, dilute model is represented by the dashed grey bar.

analysis of measurements of bubble radius “R” as a function of time “t”, we will show that the total acoustic potential energy available to the bubble on each cycle is *much less* than  $N_e\chi_0$ . There are three possible conclusions: (i) opacity is due to a mechanism other than the scattering of light by free charges, (ii) SL originates in a strongly interacting Coulomb plasma which lowers the ionization potential to such an extent that the microplasma becomes opaque, and (iii) SL has its origins in a higher temperature emitter which is a transparent blackbody imposter. The discovery [29] that spectral line shifts imply free charge densities  $10^{21}$  /cc, the analysis of spectral intensity [104], the observation that sonoluminescence can be a bubble filling blackbody [93, 92, 57], and the use of laser pulses to measure the opacity of a sonoluminescing bubble [61], select in favor of (ii); however, an evaluation of case (iii) is included in our discussion.

In order to quantify the energy contained in the dynamically evolving bubble, we acquired extremely detailed measurements of the radius as a function of time with pulsed Mie scattering. Experiments presented here are carried out in an aqueous solution that is 85% sulfuric acid (SA) by weight with 50 Torr of xenon mixed in before pressurizing with 1 atm of xenon. SL in SA is characterized by extremely bright flashes of light [28] but also by extreme jitter in space ( $\sim 2$  mm) and time ( $1 \mu\text{s}$ ). This is accompanied by SL intensity jitter due to the variety of collapse conditions brought upon by the chaotic bubble motion and resulting range of driving amplitudes [91]. A histogram of measured SL integrated intensities is shown in Fig. 3. To overcome these difficulties, we used a 100 fs, 1 mJ pulsed Ti:Sa laser at 830 nm to illuminate the bubble and collect the scattered light in a Mie scattering arrangement with a large area ( $1 \text{ cm}^2$ ) photodiode. This allowed us to simultaneously take a “snapshot” of the bubble radius while saving details of the light emission (Hamamatsu PMT) with every pulse of the laser. By recording every event independently, we could discriminate based on SL integrated intensity after the fact to build a set of radius versus time curves for selected SL conditions. Further details can be found in Appendix D.

To calibrate the Mie scattering signal, the laser could be steered into a backlighting configuration and collected with a microscope ( $5\times$  Mitutoyo Plan Apo Long WD Objective). At 16 different phases of the acoustic cycle, images of the bubble were taken to obtain an independent determination of the bubble radius throughout its motion. In a

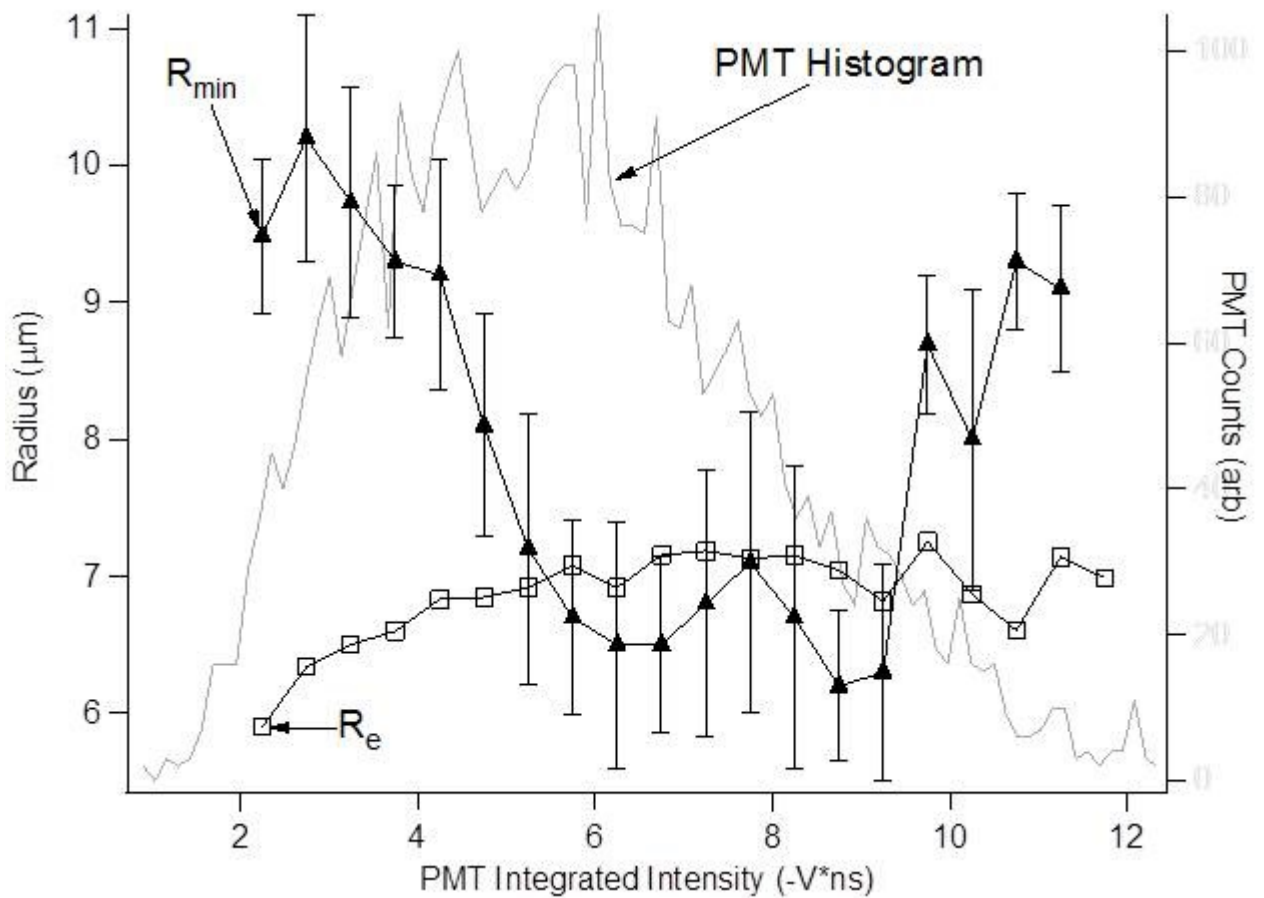


Figure 5.3: PMT histogram shows the relative frequency of integrated PMT intensities during one data acquisition.  $R_e$  is the radius of emission from black body fits of calibrated spectrum data.  $R_{\min}$  is the minimum radius measured from Mie scattering data like that of Fig. 5.1. Both  $R_e$  and  $R_{\min}$  data are discriminated by 0.5 V ns ranges of PMT integrated intensity.

similar manner to the Mie scattering data, SL integrated intensity and timing information was captured with each backlit image and this could be used to select appropriate images for each Mie scattering set. In addition, the ambient radius of the bubble ( $R_0$ ) could also be measured in this configuration by briefly interrupting the drive. For purposes of illustration, what follows is the analysis of a selection with SL integrated intensities ranging from 6 to 6.5 V ns. The postprocessed radius versus time curve resulting from this discrimination is shown in Fig. 5.1.

This Mie scattering data is fit to a solution of the Rayleigh-Plesset (RP) equation and includes thermal transport between the ideal gas in the bubble and the surrounding fluid [76, 58, 75]. The maximum Mach number  $M$  of the bubble wall relative to the speed of sound in the gas is  $\sim 0.2$ , so it is expected that the RP equation describes  $R(t)$  to a good approximation. For the purpose of theoretical analysis, this is an important advantage over other single bubbles in water which exhibit greater stability but which implode with  $M > 1$  [98, 70]. For the vast majority of the cycle, the xenon in sulfuric acid bubble behaves as an ideal gas and the simulation contains all necessary terms to accurately describe its motion. We find that the applied acoustic pressure is  $1.4 \pm 0.05$  atm with its phase shown in Fig. 5.1. Near the minimum, the necessary equations to describe its equation of state, while simultaneously satisfying all past experimental observations, do not exist. The fit we present near the minimum should be viewed in this context then as merely an accurate parametrization of the data and not a description of the internal state of the compressed matter. Nonetheless, an accurate description of the maximum collapse speed and its resulting acoustic radiation can be obtained using our methods.

During a given cycle of sound, the maximum potential energy available to heat and ionize the contents of a bubble is  $E_p = 4\pi (R_m^3 - R_c^3) p_0 / 3$ , where  $p_0$  is the ambient pressure which for Fig. 5.1 is 1 atm [66]. The number of atoms in the steady state bubble is  $N_0 = 4\pi R_0^3 p_0 / 3kT_0$ , where  $R_0$  is the ambient radius which occurs when the total pressure acting on the bubble equals  $p_0$ , and  $kT_0$  is the product of Boltzmann's constant with the ambient temperature. We measured the  $R_0$  via backlighting with sound off to be  $22 \pm 2 \mu\text{m}$  which equates to  $N_0 = 1.1 \pm 0.3 \times 10^{12}$  atoms and a collapse density of  $n_c = 1.1 \pm 0.5 \times 10^{21} / \text{cm}^3$  using  $R_c = 6.5 \mu\text{m}$ . The energy available to ionize atoms when the minimum radius is reached is equal to the potential energy plus the work done by the acoustic field, minus

the energy lost to acoustic radiation, viscosity, and heating the gas, or:

$$E_c = E_p + \Delta W_a - \Delta E_{rad} - \Delta E_\eta - \Delta U_T, \quad (5.2.1)$$

where  $\Delta E_{rad}$  and  $\Delta E_\eta$  are the energy lost to acoustic radiation and viscosity, respectively, and  $\Delta U_T$  is the energy required to heat the bubble to temperature T so that:

$$\begin{aligned} \Delta W_a &= - \int p_a dV; \\ \Delta E_{rad} &= \frac{4\pi}{c} \int R^3 \dot{R} \frac{d(p_g - p)a}{dt} dt, \end{aligned} \quad (5.2.2)$$

$$\begin{aligned} \Delta E_\eta &= 16\pi \int R \dot{R}^2 dt; \\ \Delta U_T &= \frac{3}{2} N_0 (1+x) k (T_c - T_0), \end{aligned} \quad (5.2.3)$$

where “x” is the degree of ionization and  $p_a$  is the applied acoustic pressure. For the Xe bubble in sulfuric acid pulsating as in Fig. 5.1,  $E_p/N_0 = 2.8$  eV/atom,  $\Delta W_a/N_0 = 1.7$  eV/atom,  $\Delta E_{rad}/N_0 = 1.8$  eV/atom, and  $\Delta E_\eta/N_0 = 0.7$  eV/atom. This leaves  $2.1 \pm 0.6$  eV/atom at  $R_c$ . This energy must provide for heating of electrons and ions, as well as for ionization.

We characterized the thermodynamic state of the plasma by measuring the emitted spectrum with a fiber-coupled Acton spectrometer attached to a Princeton Instruments ICCD. Individual spectrums were captured by the gated ICCD and averaged using PMT data. The spectrum associated with the dynamics of Fig. 5.1 is shown in Fig. 5.2. The calibrated spectrum when fit to a Planck blackbody yields a definite emitting radius. In this case, the size of the emitting region is  $6.4 \mu\text{m}$  at 8400 K. This agrees with the measurement of the bubble radius on collapse (Fig. 5.1b). Given the low Mach-number motion of the bubble wall, this allows us to infer that the system is opaque across the visible spectrum and nearly homogenous in both temperature and density.

Heating to 8400 K requires 1.1 eV/free particle. At an example wavelength of 400 nm, an ionization of more than 36% of the atoms, or  $N_e > 4 \times 10^{11}$ , is required for opacity. With these additional electrons, the minimum energy needed for heating is  $\Delta U_T/N_0 = 1.5$  eV. The remaining energy [ $\sim N_0(0.6$  eV)] is used to form the free electrons. Per electron-ion pair, this gives  $1.7 \pm 1.7$  eV/particle to form the free charges. Even at the limits of our

uncertainty, the available energy by this reckoning is a factor of 3 lower than the ionization potential.

According to statistical mechanics, the degree of ionization for a dilute gas follows from Saha's equation:

$$\frac{x^2}{1-x} = \frac{2g_1}{n_0\lambda^3} \exp\{-\chi/kT\}, \quad (5.2.4)$$

where  $g_1$  is the effective degeneracy of the electronic states of the ion, at 8400 K  $g_1$  is 2.7,  $\lambda = h/\sqrt{2\pi m_e kT}$  is the electron thermal de Broglie wavelength (8.1 Å at 8400 K), and  $n_0 = N_0/V_c \sim 1.1 \pm 0.5 \times 10^{21} / \text{cm}^3$  is the atomic density when the radius of the bubble has reached  $R_c$ . Using the value of the ionization potential for an isolated atom  $\chi_0 = 12.1$  eV yields  $x = 7 \times 10^{-4}$  which is orders of magnitude below the level required for opacity. In order to reach 36% ionization, this system would require the presence of a collective process that reduces  $\chi$  from 12.1 to 2.7 eV. In the event of such a process, the energy available inside of the collapsed bubble would be sufficient to produce the number of ions needed for opacity.

While the interpretation of the spectrum infers opacity and the required high level of ionization, the bubble dynamics and resulting available energy makes no such assumption. For the purposes of discussion, we can distribute the available energy to the plasma formed inside the bubble in the ideal limit where Saha's equation is applied using the bare ionization potential  $\chi = \chi_0 = 12.1$  eV. The available energy of  $2.1 \pm 0.5$  eV/atom at a density of  $1.1 \pm 0.5 \times 10^{21} / \text{cm}^3$  distributes itself according to ideal statistical mechanics to a temperature of  $13400 \pm 2500$  K and a degree of ionization of  $3 \pm 2.4\%$ . As has been emphasized [43], the spectrum of light emission at this temperature and degree of ionization should include bound-free transitions in addition to free-neutral and free-free Bremsstrahlung processes. In this manner, the best-fit transparent spectrum is calculated within the bounds of uncertainty and leads to the dashed plot in Fig. 5.2. In this case, both maximum temperature (15900 K) and atomic density ( $1.6 \times 10^{21} / \text{cm}^3$ ) were needed to best match the intensity of the data. As mentioned [44, 41], the peak in the transparent 15900 K spectrum is close to the peak in the 8400 K blackbody. Given the various uncertainties and the fact that the measured spectrum is an average over the entire implosion event, these spectra are in reasonable qualitative agreement.

Various theoretical and experimental insights can be used to distinguish between the opaque and transparent “blackbody-impostor” solutions for the light emitting state. First, consider the strong spectral line at 823 nm from a transition that has the metastable  $\text{Xe}^*$  as its ground state. This is an opaque line and its peak will lie on a blackbody curve with the plasma’s temperature [106] (p. 247). The predicted line intensity is shown in Fig. 5.2, supposing this was a transparent system at 15900 K. Yasui [102] has presented a detailed analysis of quenching of molecular lines in sonoluminescence from single bubbles in water and has argued that they are quenched by collisions. What makes SL from sulfuric acid so interesting is that the gas density at the moment of collapse is so low— being an order of magnitude less than SL in water. This system is therefore more amenable to modeling and it will be interesting to see if theory exhibits quenching of the atomic lines by collisions. Time resolved spectra of a single xenon bubble in phosphoric acid [57] were acquired at collapse gas densities and temperatures comparable to this Letter. These data show that the opaque atomic line does not disappear until it is swallowed by the broadband blackbody spectrum. For these reasons, we propose that the absence of the  $\text{Xe}^*$  823 nm line in Fig. 5.2 supports our assertion that the light emitting region is not transparent. Finally, there is an argument based upon well-known, first order corrections to Saha’s equation [106, 64]. At 15900 K with  $n_0 = 1.6 \times 10^{21} / \text{cm}^3$ , Eq. 5.2.4 yields a degree of ionization of  $x = 5.4\%$  which we now argue is unstable at the first order of perturbation. Following Landau and Zel’dovich [106, 64], the ionization potential is corrected at first order to

$$\chi \approx \chi_0 \left( 1 - 2\gamma a_B n_0^{1/3} \right) - Ae^2/\delta_D, \quad (5.2.5)$$

where  $A = 1$  is the coefficient of the Debye screening term which reduces the distance an electron must move from an atom to be liberated to  $\delta_D = \sqrt{kT/8\pi n_e e^2}$ ,  $a_B$  is the Bohr radius, and  $\gamma = 1.78$  is a coefficient determined by photon induced conductivity in cold xenon at high pressure [37]. The first term reduces the ionization potential via the hybridization of nearest neighbor xenon atoms. This term has been applied to SL previously by Yasui [103]. For 15900 K and  $n_0 = 1.6 \times 10^{21}$ , Eq. 5.2.5 yields a reduction in ionization potential of 4.8 eV. Plugging this back into Eq. 5.2.1 dramatically increases the degree of ionization and the transparent fit in Fig. 5.2.2 is no longer valid. We have

proposed that for such large T and atomic density, the effects of screening cannot be treated as a simple perturbation. Instead one must seek a self-consistent solution to Eqs. 5.2.4 and 5.2.5 subject to the available total energy (this possibility was realized in [36]). For the parameter space discussed in this Letter and with  $A \approx 1$ , no self-consistent solution exists indicating a degree of ionization approaching  $x = 1$ .

The high degree of ionization inside of an SL plasma is due to the fact that SL occurs at a relatively high atomic density. Ebeling et al. has calculated  $x(n_0)$  for given temperatures for xenon and found that at densities above  $\sim 10^{22} / \text{cm}^3$  there is a rapid increase in “ $x$ ” which looks like a first order phase transition [24]. For the 28 kHz xenon bubble in sulfuric acid discussed above and for the 40 Hz xenon bubble in phosphoric acid [57], blackbody behavior and therefore, a large value of “ $x$ ” is found at  $n_0 \sim 1.1 \times 10^{21} / \text{cc}$ . In these cases, the phase transition to opacity occurs at an unexpectedly low value of the density. A simple picture of how this can happen is provided by Eq. 5.2.5. If  $A$  is chosen to be a weakly varying function of the thermodynamic parameters then a reduction of the ionization potential to 2.7 eV as required for opacity can be achieved. At 8400 K and  $n_0 = 1.1 \times 10^{21} / \text{cc}$ , the electrostatic potential at the Debye radius is  $e^2/\delta_D = 10.7\sqrt{x}$  eV, so that lowering of due to hybridization of 2.4 eV when added to a lowering of 7.0 eV due to electrostatic screening provides the requisite ionization potential. This occurs with  $A \gtrsim 1.1$  and a self-consistent solution to Eq. 5.2.5, for the best fit parameters used in this analysis.

The above analysis was carried out for data where the PMT integrated intensity was 6–6.5 V ns. A summary of the spectrum blackbody radius fits ( $R_e$ ) and Mie scattering collapse radius ( $R_c$ ) for other selections can be found in Fig. 5.3. For a range of PMT areas,  $R_c$  and  $R_e$  agree and it is clear that blackbody behavior is attained. The analysis of potential lowering for all values is in Appendix D. In all of these cases, the ionization potential needs significant reduction to attain the required ionization.

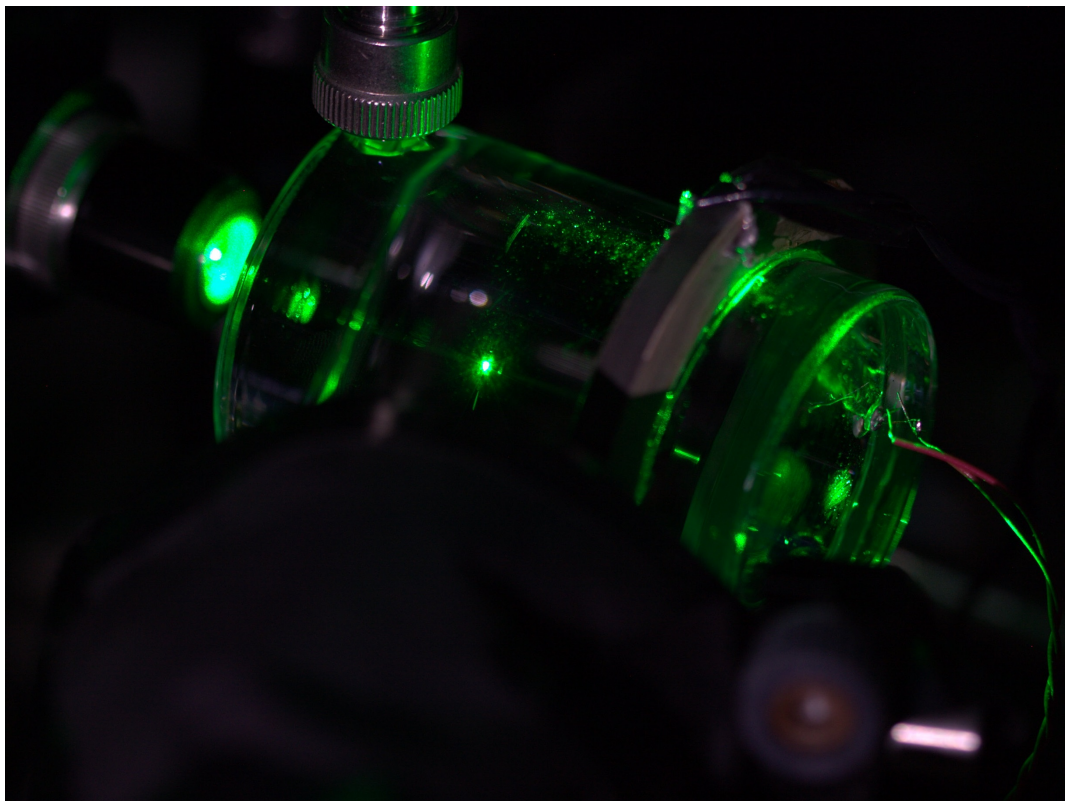
Sonoluminescence in a weakly collapsing bubble is well described by hydrodynamics. We have detailed a new technique whereby input sound and bubble dynamics can be measured with sufficient accuracy so that via application of energy conservation, one can elucidate thermodynamic properties of the plasma which form inside the bubble at the moment of light emission. In the case of a bubble in sulfuric acid driven at 28 kHz, we

can apply energy conservation and find only  $2.1 \pm 0.6$  eV/atom available to the interior gas for ionization and light emission. A transparent theory for this dense plasma can be discounted as it is unstable to well-known first order perturbation theory and fails to describe line intensity. Likewise, sufficient ionization for opacity cannot be achieved with this amount of energy using the Saha model of a dilute gas. As a result, we argue that the ionization potential must be lowered dramatically by screening and hybridization. How this theory is put on a first principles statistical mechanics basis along the lines of Teller et al. [13] remains to be seen.

We gratefully acknowledge support from the Air Force Office of Scientific Research. We thank Brian Naranjo, Keith Weninger, and Carlos Camara for valuable discussions.

# Chapter 6

## Sonoluminescence-Laser Interaction



## 6.1 Introduction<sup>1</sup>

The path which led to the experiment presented in this chapter was by no means straight. Initially, this experiment was motivated by the idea that SL plasma not only emits like a blackbody, it also absorbs like a blackbody. Calculations indicated that if SL absorbed most of the energy from a high-intensity pulsed laser, incredible temperatures could be obtained, and even the possibility of fusion in deuterated systems. Although high temperatures were not achieved, strong laser-SL coupling was demonstrated and provided a new path for studying SL plasma.

According to plasma theory, an electron density  $n_e \gtrsim 10^{21} \text{ cm}^{-3}$  is required for a micron-sized plasma to be opaque to visible light ( $T \sim 1 \text{ eV}$ ). However, in the 25 years after its discovery, a measurement of  $n_e$  in water SL remained elusive. This experiment makes the first-ever measurement of  $n_e$  and confirms SL as a strongly-coupled plasma. This result relies on the response of laser-SL coupling to different laser wavelengths and is a direct consequence of the kinetic theory presented in Chapter 4. Once more, the existence of a plasma phase transition to a highly-ionized state is consistent with the experimental findings and the density-corrected Saha's equation in Chapter 3.

---

<sup>1</sup>Chapter Image: Photograph of the experimental setup of the “Sonoluminescence-Laser Interaction” experiment. The photograph shows the water-filled SL resonator (center), Mie collecting optic (bottom), microscope objective for laser-focusing (left of resonator), and laser-bubble beam path (green illumination). A laser is focused onto a collapsing xenon bubble (center) and results in laser-plasma interactions only during SL emission.

## 6.2 Collision Time Measurements in a Sonoluminescing Plasma with a Large Plasma Parameter

The plasma which forms inside of a micron-sized sonoluminescing bubble in water for under a nanosecond has been probed with 3 ns long laser pulses. A comparison of the response to 532 and 1064 nm light indicates that the plasma density is about  $2 \times 10^{21} \text{ cm}^{-3}$  and that transport properties are dominated by strong effects due to screening. The spherical shape, uniform pressure, and well-defined atomic density make the sonoluminescing plasma a test bed for theories of strongly coupled plasmas. Plasmas in these experiments distinguish between competing theories of strong, intermediate, and zero screening.

The passage of a planar sound wave through a fluid leads to pulsations of a trapped bubble that are so large that the energy density of sound is concentrated by 12 orders of magnitude to generate flashes of ultraviolet light that can be as short as 35 ps [46, 38, 47]. The mechanism of energy concentration and the state of the bubble contents at the moment of light emission constitute the study of sonoluminescence (SL). During the rarefaction part of the sound field, the radius “ $R$ ” of the bubble expands to a maximum value, where the internal pressure of the gas it contains is low compared to the ambient value of 1 atm. In a 30 kHz sound field, the subsequent implosion is supersonic as it passes through the ambient radius “ $R_0$ ” on the way to a collapse radius “ $R_c$ ” [94]. The ideal gas law gives an ambient density of  $n_0 = 2.4 \times 10^{19} \text{ cm}^{-3}$  and for xenon gas  $\frac{R_0}{a} \sim 7.6$ , where “ $a$ ” is the radius of the bubble when the gas is compressed all the way to its van der Waals hard core. Light scattering measurements indicate that for a trapped single bubble in a 30 kHz sound field,  $R_c \sim a$  so that the atomic density in the collapsed xenon bubble is  $n_c \sim 10^{22} \text{ cm}^{-3}$  [5].

At the moment of maximum compression:  $R \sim R_c \sim 1/2 \mu\text{m}$ , a flash of light is emitted. Its spectral density closely matches an ideal Planck blackbody [92, 15, 28, 48]. As a blackbody is opaque the free charge density must be very high. According to the simplest formulas for opacity where it is due to scattering of light by free charges [106], a photon mean free path of  $1/2 \mu\text{m}$  at 532 nm and the measured temperature of 9250 K requires a

charge density  $n_e > 10^{21} \text{ cm}^{-3}$ . Analysis of line spectra in other sonoluminescing systems have been interpreted in terms of similar charge densities and temperatures [88, 29, 57].

The repetitive attainment of such dense plasmas in spherical geometries with a controlled atomic density at temperatures  $T \sim 1 \text{ eV}$  enables the use of SL for studying transport properties of dense plasmas. For this case, the plasma parameter is  $2.9 < \Gamma < 6.3$ , where

$$\Gamma = \frac{e^2}{kT} \left( \frac{4\pi n_e}{3} \right)^{1/3}. \quad (6.2.1)$$

In this paper we explore this new direction in SL research by comparing the response of the SL plasma to input laser light at two different wavelengths, 1064 and 532 nm. This test is motivated by the fact that the free charge densities are so high that the corresponding plasma frequency  $\omega_p = \sqrt{\frac{4\pi n_e e^2}{m_e}}$  (where  $m_e$  is the electron mass) is comparable to the angular frequency  $\omega$  of the light in the laser pulses, which can be used to probe the SL micro-plasma. According to whether  $\omega > \omega_p$  or  $\omega < \omega_p$  the incident light is transmitted or reflected by an ideal plasma. We note that  $n_e \sim 10^{21} \text{ cm}^{-3}$  corresponds to a plasma wavelength  $\lambda_p \sim 1000 \text{ nm}$ , which lies between the 1064 and 532 nm probe pulses. The goal of studying the interaction of a laser with SL was first introduced by Diebold [16] with the purpose of generating high plasma temperatures. A recent experiment by Khalid et al. [61] demonstrated successful SL-laser coupling and provided further evidence that SL is a highly-ionized plasma [57, 56]. Our experiment entails both spatial and temporal challenges. The laser must hit the bubble at a properly synchronized moment during the acoustic cycle.

Fig. 6.1 shows the main experimental observation that: a) a weak pulse of 532 nm light can interact with the SL plasma and lead to an increase in light emission; whereas b) the 1064 nm light interacts with the SL plasma only above an intensity threshold. The upper data set on each panel shows the Mie scattering signal from the bubble, which is a measure of its radius. The lower curve shows the intensity of SL during that same acoustic cycle as recorded by a photomultiplier tube (PMT). The diagonal data set in the middle shows the increase in light output of the bubble when the laser hits the bubble during the lifetime of the SL micro-plasma. Theoretical analysis of this data permits one to select between the transport theory of dilute plasmas and various screening modifications put

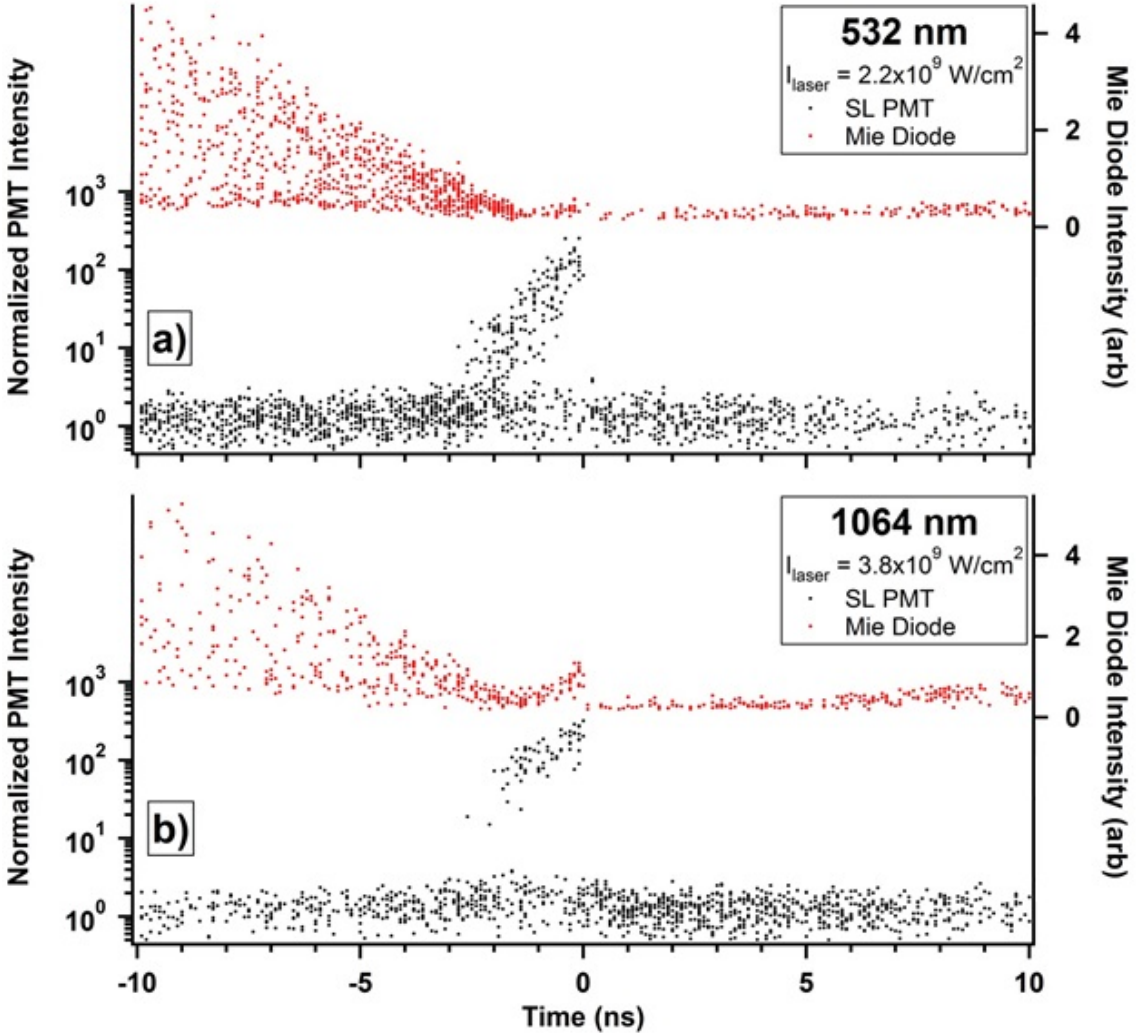


Figure 6.1: Scatter plots showing the Mie scatter intensity (red dots) and the SL intensity (black dots) for a) 532 and b) 1064 nm. The SL intensity is normalized by the intensity distribution of SL flashes without an incident laser pulse and can be seen as a band of points centered on unity. For each SL intensity point, there is a corresponding Mie scatter point which is a measure of the bubble's radius and confirms successful spatial synchronization. SL-laser interactions only occur when the laser and SL flash overlap in time. The spread in Mie scatter points is due to the drift in bubble location relative to the laser focus during the laser's repetition rate (10 Hz).

forward by different authors [63, 22, 62].

Into degassed water we dissolve 150 Torr of a gas mixture that is 99% nitrogen and 1% xenon. The water is in a 30 kHz quartz resonator driven by piezoelectric transducers. A bubble is seeded into the resonator near the velocity node of the standing wave resonance and is driven to large pulsations and sonoluminescence. A YAG laser is synchronized with the bubble by timing from the previous SL emissions, as the flashes have a sub-nanosecond clocklike repetition [6]. Three light detectors are used; a photodiode which records the scattered laser light, a photodiode that measures the intensity and timing of the laser pulse, and a PMT with a laser-blocking filter (Notch) that records the broadband SL as well as the additional broadband emission which results from a laser pulse that is successfully synchronized with an SL flash. The acquisition of many scattering events and many flashes of SL is displayed in Fig. 6.1. The intensities of each event are plotted as a function of the time elapsed between the leading edge (10% peak intensity) of the laser pulse and the SL flash (which occurs at  $t = 0$ ). For instance, the SL events plotted at -4 ns (on the lowest trace) correspond to acoustic cycles where the leading edge of the laser hit the bubble 4 ns before the SL flash. Such an early hit corresponds to a bubble with a radius larger than  $R_c$ , and so the laser light scattered from the bubble as shown on the upper trace is much larger than occurs at the minimum radius, which happens at  $t = 0$ . If the bubble is not at its minimum radius: i.e. if it is not in the process of emitting SL, then the PMT records the intensity of the SL flash for that cycle and it is plotted below the time of the laser hit. This is shown by the PMT events close to the abscissa. As the laser pulse is  $\sim 3$  ns in duration, a laser-plasma interaction can occur even when the leading edge of the laser reaches a bubble 3 ns before SL. These laser on plasma events can be weak (532 nm) or zero (1064 nm) because the laser is turning off as the SL is turning on. A laser hit can also result in a weak interaction if the bubble is not centered on the laser's focus, which results in a spread in Mie intensities for a given time. The largest events are seen when the laser arrives at the bubble as SL is turning on. In this case we find broadband emission with an energy that can be much higher than a typical flash of SL.

The SL-laser interaction gap (see Fig. 6.1) for 532 vs. 1064 nm is apparent in the histogram of events shown in Fig. 6.2. Fig. 6.2 displays the frequency of events during

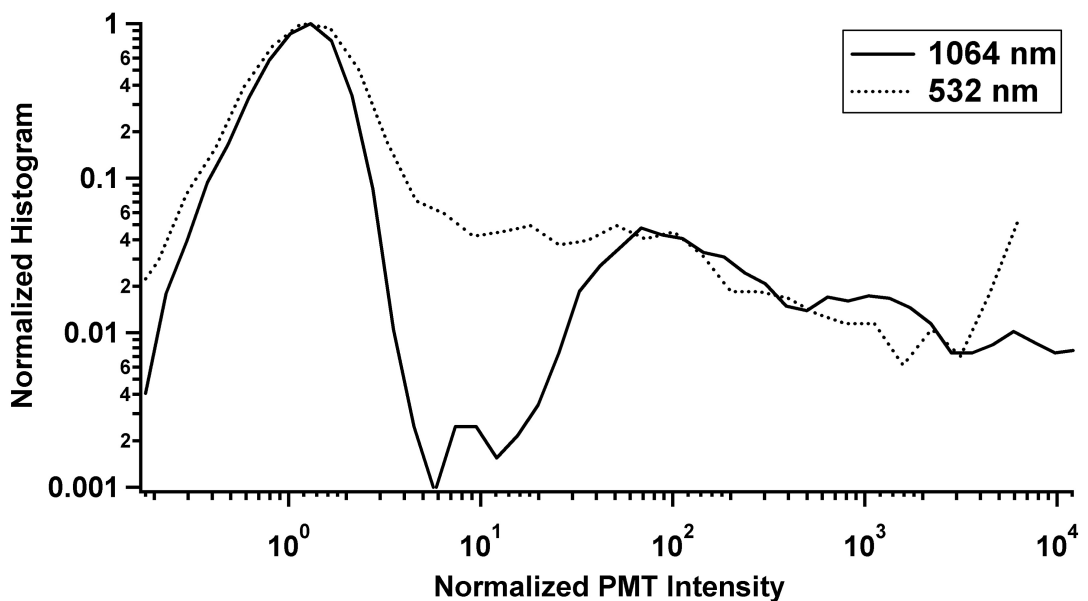


Figure 6.2: Normalized histogram of the SL intensity for a range of laser intensities ( $0.5 - 25 \times 10^9 \text{ W/cm}^2$ ) at 1064 (solid curve) and 532 nm (dotted curve). Only points within the interaction region of -4 to +1 ns (532 nm) and -8 to +1 ns (1064 nm) were used for the histogram. Although concurrent to the SL, a large number of laser shots did not result in an interaction due to the lack of spatial overlap caused by the bubble's drift in location.

the SL-laser temporal overlap as a function of the intensity of total light emission from the bubble. This includes the usual SL plus the energy grabbed from the laser by the SL plasma. The peak at unity is the strength of a typical free running flash of SL and the gap from 4-20 reflects the difference in interaction of the 532 vs. 1064 nm laser wavelengths with the SL plasma. What we measure is clearly below the breakdown threshold which occurs at an intensity 50000 times that of SL and 200 times larger than the minimum observable laser bubble interaction. This confirms that we are seeing an interaction between the laser and the SL plasma.

The interaction of a laser pulse with a plasma is affected by the plasma frequency and the collisionality (or absorptivity) of the plasma. The reflection of light by a sufficiently dense plasma when  $\omega < \omega_p$ , assumes an ideal plasma with  $\omega\tau \gg 1$ , where  $\tau$  is the collision time. In this limit the motion is reversible and no energy is absorbed by the plasma. A theory which explains the conversion of incoming light into plasma energy must include a finite  $\tau$ .

Reflectivity in the limit  $\tau \rightarrow \infty$  is graphed in Fig. 6.3. The solid curves give the plasma reflectance as a function of the free charge density for 532 and 1064 nm. On Fig. 6.3 this is labeled as the Debye theory of transport. The transition to complete reflectance at high charge density is the well-known plasma frequency effect which motivated this experiment. When interactions are included according to the transport theory of a dilute plasma (see below), one obtains the dotted line in Fig. 6.3. Application of the theory of dilute plasmas to high charge densities leads to short collision time,  $\omega\tau < 1$ . In this limit absorption shorts out plasma reflection. An explanation of the SL-laser interaction requires a theory of the collision time for dense plasmas which follows.

Electrons of mass  $m$  and velocity “ $\vec{v}$ ” are accelerated by an electric field  $\vec{E}$  according to the Drude model,

$$m_e \frac{d\vec{v}}{dt} + \frac{m_e}{\tau} \vec{v} = -e \vec{E}. \quad (6.2.2)$$

When coupled to Maxwell's equations in the presence of a disturbance driven at frequency  $\omega$ , one obtains the dispersion law for the plasma wavenumber  $k_p$  given by [27]

$$k_p^2 = \frac{\omega_p^2}{c^2} \frac{i\omega\tau}{1 - i\omega\tau} + \frac{\omega^2}{c^2}. \quad (6.2.3)$$

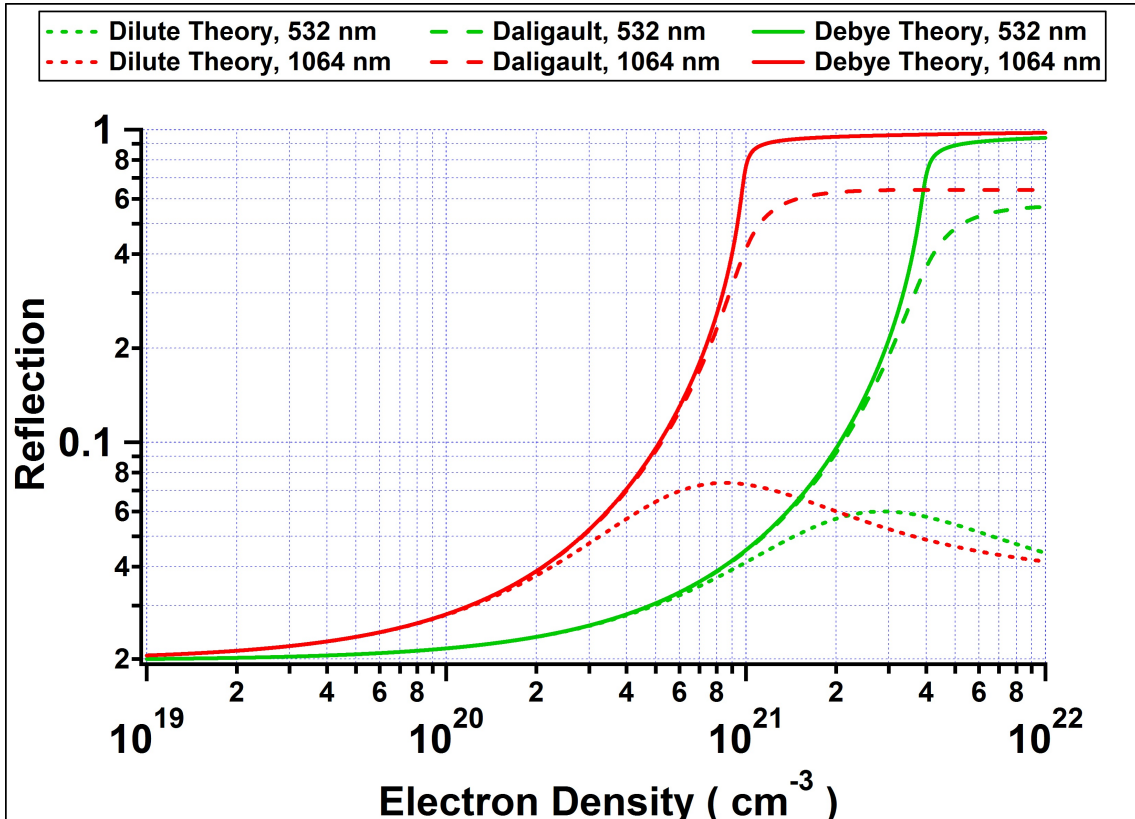


Figure 6.3: Plasma reflection of 532 and 1064 nm light as a function of electron density for various collision theories. The Debye theory (solid curves) represents a highly-screened plasma, where  $\omega\tau \gg 1$  and high levels of reflection are observed for  $\omega < \omega_p$ . The dilute theory (dotted curves) diverges from the high reflectivity behavior due to strong damping ( $\omega\tau \lesssim 1$ ) in the high density regime. The Daligault theory (dashed curves) experiences an intermediate level of reflection in the dense regime and is capable of describing both reflection at 1064 nm and spectral opacity at 532 nm.

For the frequency dependent collision time in the gaseous plasma, we take

$$\tau = \frac{3\hbar\omega}{4\pi n_e e^4 [1 - e^{-\beta\hbar\omega}]} \sqrt{\frac{3m_e kT}{2\pi}} \frac{1}{\ln \Lambda}. \quad (6.2.4)$$

This term includes the limit of  $\hbar\omega \rightarrow 0$ , where  $\tau$  is determined by small energy collisions in a Coulomb plasma, as well as free-free scattering in which an electron absorbs a photon of frequency  $\omega$ . In the limit where  $\omega > \omega_p$ ,  $\omega\tau \gg 1$ , and  $\ln \Lambda = 1$ , Eqs. (6.2.3) and (6.2.4) yield a  $2Im(k_p)$  consistent with inverse Bremsstrahlung attenuation of light (Eq. 5.21 of [106] corrected for induced emission).

For a dense plasma with  $\Gamma > 1$ , screening must be included to determine the effective collision frequency. For this analysis, we consider two screening models which assign a formulation for the Coulomb logarithm in Eq. (6.2.4). The first is the extreme screening model that utilizes the logarithmic formulation presented by Valuev [63] and sets the Debye length as the maximum impact parameter (Eq. (6.2.5a)). The second model proposed by Daligault [22] represents an intermediate scaling of the impact parameter (Eq. (6.2.5b)). The dilute theory is also considered for comparison (Eq. (6.2.5c)) where screening is not applied. These models are given by:

$$\text{"Debye"} : \quad \ln \Lambda = \frac{\sqrt{3}}{\pi} \ln \sqrt{\frac{1}{6} \Gamma_\omega^{-3} + 1}, \quad (6.2.5a)$$

$$\text{"Daligault"} : \quad \ln \Lambda = \frac{\sqrt{3}}{\pi} \ln \left( \frac{0.7}{\sqrt{6}} \Gamma_\omega^{-3/2} + 1 \right), \quad (6.2.5b)$$

$$\text{"Dilute"} : \quad \ln \Lambda = \frac{\sqrt{3}}{\pi}, \quad (6.2.5c)$$

where

$$\Gamma_\omega = \Gamma \left( \frac{kT}{\hbar\omega} \left( 1 - e^{-\beta\hbar\omega} \right) \right). \quad (6.2.6)$$

As we apply transport theory over a range of frequencies we include the possibility of the plasma parameter becoming a function of frequency (Eq. (6.2.6)) as has been included by Dawson [55]. Furthermore, we have also included an overall factor of  $\sim 2$  in Eq. (6.2.4) that distinguishes Dawson and Daligault from Zel'dovich.

Inclusion of screening (Eqs. 6.2.5a and 6.2.5b) lengthens the collision time for  $\Gamma > 1$  and according to Eq. 6.2.6 this effect varies with wavelength. Fig. 6.4 shows the distance

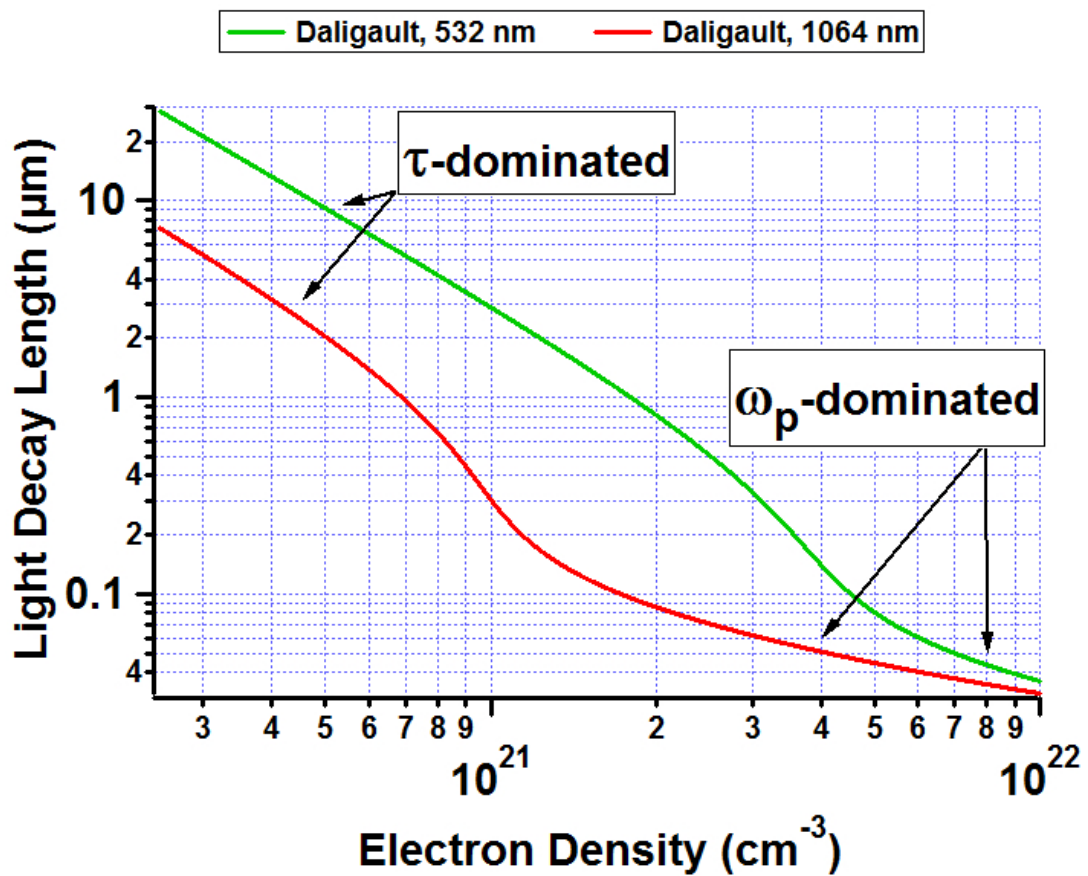


Figure 6.4: Decay length of light in a dense plasma for 532 and 1064 nm using the collision theory of Daligault. Two absorption regimes are present for the electron density under consideration and are separated at the critical density ( $\omega_p = \omega$ ). Based on the suggested electron density of  $\sim 2 \times 10^{21} \text{ cm}^{-3}$  for the SL measured in this experiment, the absorption is  $\tau$ -dominated for 532 nm and  $\omega_p$ -dominated for 1064 nm.

light travels before decaying to  $1/e$  as a function of electron density for the Daligault theory (Eq. 6.2.5b). The region labeled  $\tau$ -dominated occurs when the laser frequency is greater than the plasma frequency. For the Daligault theory at a charge density of  $\sim 2 \times 10^{21} \text{ cm}^{-3}$ , the 532 nm light is  $\tau$ -dominated while the 1064 nm light is  $\omega_p$ -dominated and is strongly reflected. In this range of charge density, the 532 nm penetrates most of the bubble while the 1064 nm penetrates just a fraction of the bubble radius.

We appeal to the Daligault theory and the region of parameter space with a charge density of  $\sim 2 \times 10^{21} \text{ cm}^{-3}$  to explain the interaction of a laser with the micro-plasma in a sonoluminescing bubble. First, at this density the decay length of 532 nm light is approximately equal to the bubble radius which is consistent with the observed Planckian spectrum. Next, the 532 nm light penetrates the bubble whereas the 1064 nm light is restricted to a depth less than 20% of the bubble radius. Furthermore, the intensity of light at 1064 nm to penetrate into the ‘surface’ region is down by a factor of 2.5 from the 532 nm light. It is important to note that for all of the theories discussed, densities lower than  $10^{21} \text{ cm}^{-3}$  would result in weak laser-plasma coupling due to the long decay length (Fig. 6.4).

A full explanation of the absorption gap shown in Figs. 6.1 and 6.2 still requires some nonlinear threshold phenomenon that allows for weak interactions at 532 nm but precludes the absorption of weak laser light at 1064 nm. This phenomenon goes beyond processes that we have included in the theory of  $\tau$  (Fig. 6.5). To this end we note that the average laser intensity at 1064 nm is  $3.8 \times 10^9 \text{ W/cm}^2$ , which corresponds to an electric field  $E \sim 10^6 \text{ V/cm}$ . From Fig. 6.5 the collision time is about 5 fs so that between collisions, an electron with thermal velocity  $\sim 7 \times 10^7 \text{ cm/s}$  moves about 3.5 nm. The change in electron velocity during a period of light is about  $10^6 \text{ cm/s}$ . The number of velocity increments of this size required to double the energy is 50, if the collisions were all additive. Due to the randomness of collisions and due to  $\omega\tau \sim 4$ , the total number of collisions required to double the energy is  $50 \times 50 \times 4 \times 4 = 40,000$ . During this time the electron walks a distance  $\sim 1 \mu\text{m}$ . This distance is much greater than the electric field’s penetration depth which we interpret as implying that at 1064 nm, externally driven diffusion precludes finite energy transfer. At 532 nm the response is  $\tau$ -dominated and the field penetrates most of the bubble and finite transfer is possible. The time required

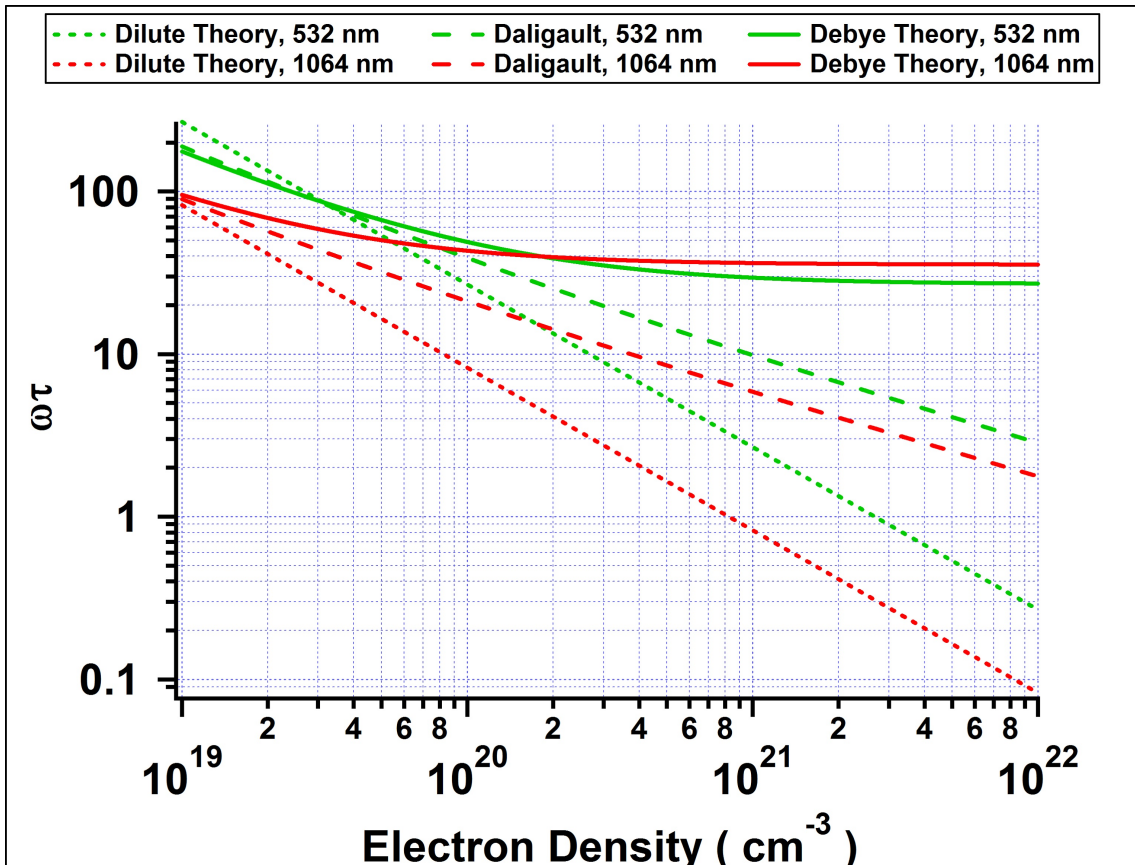


Figure 6.5: Collision time of 532 and 1064 nm light as a function of electron density for various collision theories. The collision time for the Debye theory (solid curves) is large for all electron densities and becomes density-independent for large plasma parameters. The dilute theory (dotted curves) represents the shortest collision time. The intermediate theory of Daligault (dashed curves) lies between these limiting theories and scales with  $\omega_p$  for large densities.

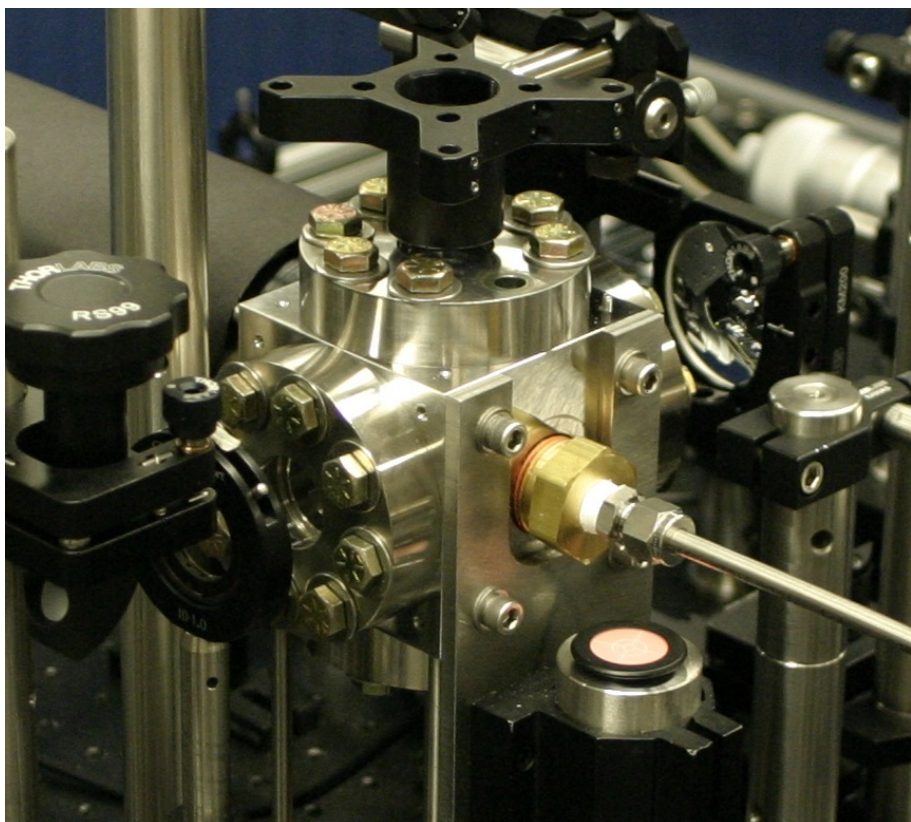
for the energy of an electron to double in the externally applied field is about 0.5 ns. Possible threshold phenomena include breakdown at the water interface and higher levels of ionization.

The plasma which forms in a collapsing noble gas bubble reaches a density with a plasma parameter in excess of unity. The bubble has a well-defined number of atoms, is spherical in shape, and has a uniform pressure. It therefore becomes a test bed for the study of transport phenomena in dense plasmas. We have probed the sonoluminescing micro-plasma by targeting it with synchronized laser pulses at 532 and 1064 nm. Light emission from the resulting interactions enable one to decide between various transport theories of dense plasmas and to determine that the plasma density is about  $2 - 3 \times 10^{21} \text{ cm}^{-3}$ . This technique has provided an electron density measurement for single-bubble SL in water, which has remained elusive for almost 25 years after its discovery. The measured plasma density of  $\sim 3 \times 10^{21} \text{ cm}^{-3}$  corresponds to a Fermi temperature of 8700 K, which is slightly less than the spectral temperature. The possibility remains that some regions of the SL parameter space can exhibit Fermi degeneracy as well as dense plasma kinetics [51, 50].

We gratefully acknowledge support from DARPA MTO for research on micro-plasmas and AFOSR for research on transport in dense plasmas. We thank Guillaume Plateau and Keith Weninger for valuable discussions.

## Chapter 7

# Laser Breakdown in High-Pressure Gases



## 7.1 Introduction<sup>1</sup>

The plasma phase transition observed in sonoluminescence occupies a region of phase space defined by temperatures and densities in the strongly-coupled regime ( $T \sim 1$  eV and  $n_0 \sim 1 - 10 \times 10^{20}$  atoms/cm $^{-3}$ ). These densities can easily be obtained by using compressed gases. For example, noble gases at 40 bar contain  $1 \times 10^{21}$  atoms/cm $^{-3}$ , which is well within the operating pressures of laboratory gas cylinders ( $\sim 150$  bar). Thermal energy must now be provided to the system. The amount of energy needed to heat up  $10^{21}$  particles/cm $^{-3}$  to 20000 K in a spherical volume with a  $25\text{ }\mu\text{m}$  radius is  $\sim 25\text{ }\mu\text{J}$ . Furthermore, the energy must be absorbed in a fast timescale to avoid a rapid decrease in atomic density due to hydrodynamic expansion. This makes femtosecond laser breakdown in noble gases an ideal system for a first attempt at reproducing the conditions of sonoluminescence.

Determination of the plasma phase transition requires knowledge of the temperature and atomic/electronic densities. The opacity of sonoluminescence has been a key indication of the plasma phase transition as a micron-sized blackbody requires  $\sim 10^{20} - 10^{21}$  electrons/cm $^{-3}$ . Therefore, a blackbody spectrum not only provides a plasma temperature, it also infers a high level of free electrons. This motivates calibrated streak spectroscopy for the following experiment.

By measuring a blackbody from laser breakdown in high-pressure gases, the phase transition of sonoluminescence is reproduced in a completely different system. This is a strong indication of a *universal* equation of state in strongly-coupled plasma, which is *not* unique to the sonoluminescence phenomenon. It belongs to a much larger class of plasma whose properties we are just beginning to explore. As a bonus, this experiment also provides an unexpected transport measurement that's both consistent with the "Daligault" theory of screening (Chapter 4) and the electron density required for opacity.

---

<sup>1</sup>Chapter Image: Photograph of the high-pressure chamber in the laser-breakdown experiment. The chamber (center) is filled with high-pressure gas through a pressure inlet (right) and is sealed on 5 sides by UV-grade pressure windows. 100 fs laser pulses are focused through a lens (top) and into the center of the gas chamber. At the location of strongest laser intensity, blackbody plasma is generated and analyzed by a streak system (not shown).

## 7.2 Blackbody Emission from Laser Breakdown in High-Pressure Gases

Laser induced breakdown of pressurized gases is used to generate plasmas under conditions where the atomic density and temperature are similar to those found in sonoluminescing bubbles. Calibrated streak spectroscopy reveals that a blackbody persists well after the exciting femtosecond laser pulse has turned off. Deviation from Saha's equation of state and an accompanying large reduction in ionization potential are observed at unexpectedly low atomic densities – in parallel with sonoluminescence. In laser breakdown, energy input proceeds via excitation of electrons whereas in sonoluminescence it is initiated via the atoms. The similar responses indicate that these systems are revealing the thermodynamics and transport of a strongly-coupled plasma.

The passage of a sound wave through a fluid can lead to pulsations of a gas bubble that are so strong that a dense plasma forms at its minimum radius. The degree of ionization  $n_e \sim 10^{21} \text{ cm}^{-3}$  is much larger than follows from Saha's equation at the measured temperature  $T \sim 10000 \text{ K}$ . Experiments on sonoluminescence (SL) have been interpreted in terms of screening correlations which modify the equation of state at atomic densities that are over an order of magnitude lower than expected from theories of strongly-coupled plasma (SCP) [88, 57, 58, 87, 61, 56, 9]. The plasma inside a sonoluminescing bubble is created via direct heating of the atoms. Mechanical energy from the sound field sets up an implosion which compresses and heats the atoms to the point where they ionize. The liberated electrons are brought up to the ion/atom temperature via collisions. The emitted thermal spectrum is mainly due to collisions of hot electrons with ions. In low frequency ( $\sim 40 \text{ Hz}$ ) experiments the flash width is hundreds of nanoseconds and the electron temperature is in local thermodynamic equilibrium (LTE) with the ions and light. If the unexpected high degree of ionization and resulting opacity of a sonoluminescing bubble is due to fundamental changes in the equation of state of cold dense plasmas then these effects should be independent of the path by which the temperature and density are reached. To test whether the sonoluminescing micro-plasma is indeed a manifestation of a new thermodynamic equation of state we have generated similar plasmas using laser

breakdown in high-pressure gases with atomic densities in the range  $10^{19} - 10^{21} \text{ cm}^{-3}$ . In this case the path for energy flow is the reverse of SL as flashes from a femtosecond laser instantly ionize and energize the electrons while the ions remain cold. We report observation of opaque plasma that persists, well after the laser has turned off, and for times much longer than the recombination timescale. The spatial, temporal, and spectral properties of these plasmas are consistent with the equations of state of the SL microplasmas and temporal evolution of the blackbody temperature provides insights into transport in SCP's.

The focusing of high-intensity laser pulses into gaseous media begins with a rapid ionization and heating of electrons. This is followed by a plasma expansion into the surrounding gas, whose luminous front vs. time is shown in Fig. 7.1. The micron-scale plasma in Fig. 7.1 was generated using a 120 fs amplified Ti:Sapphire laser (Spectra-Physics, Tsunami/Spitfire) operating at 1 kHz with an adjustable energy of 0–1 mJ/pulse using a variable attenuator. The laser was focused with a 6 cm lens into the center of a stainless steel pressure chamber. Optical access through the chamber was provided by UV-grade fused silica viewports (Raytek Inc.) and tested to 10000 psi. The plasma's light emission was collected and imaged by a 90 mm UV-to-NIR triplet lens (Edmund Optics). The plasma image was magnified by 5.34 and imaged onto the entrance slits of a 150 mm Czerny-Turner spectrometer (Princeton Instruments, sp-2150i). The spectrally-resolved plasma image was temporally-resolved by aligning the spectrometer's output image onto the entrance slits of a streak camera (Hamamatsu, C5680-A1976-01). The streak image in Fig. 7.1a is produced by keeping the spectrometer's entrance slits fully-open (3 mm) and moving the grating to 0<sup>th</sup>-order. Similarly, the spectral images in Fig. 7.2 were acquired by closing down the spectrometer's entrance slits (30  $\mu\text{m}$ ) and moving the grating to 1<sup>st</sup>-order. The total amount of incident light entering the system in either mode is defined by the overlapping slit areas. The plasma image could be moved relative to the imaging system allowing spectral analysis at any plasma location. The spectral measurements presented in this Letter contain light from a plasma area of  $32 \mu\text{m}^2$  and was located at the center of the plasma column.

Due to the limited amount of light entering the imaging system, each spectral image (Fig. 7.1) consisted of an average of  $10^5$  breakdown events. However, shot-to-shot plasma

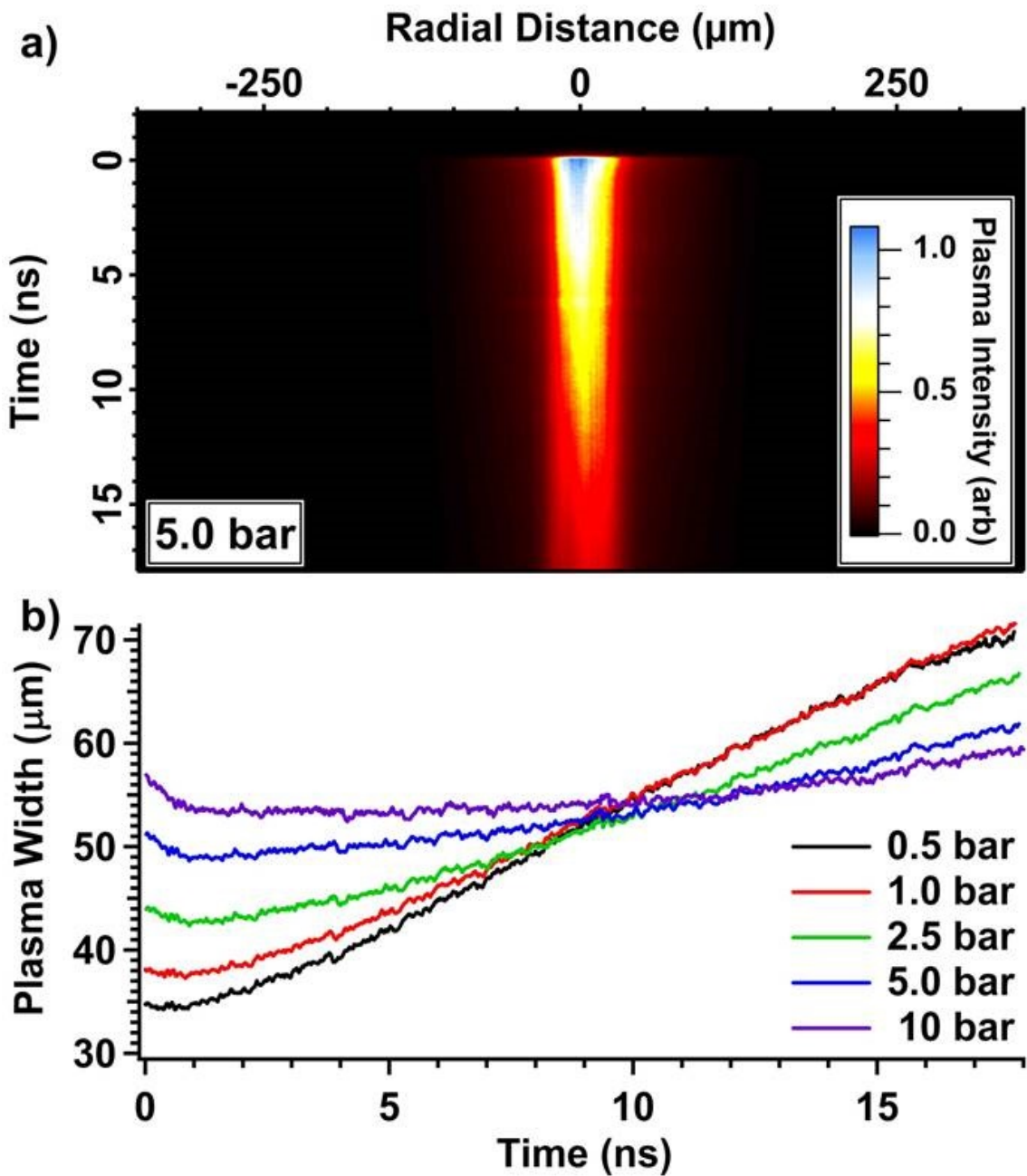


Figure 7.1: Spectrally integrated plasma emission ( $>495 \text{ nm}$ ) vs. radius and time. The streaked image a) was acquired for 5 bar xenon breakdown using a laser energy of  $235 \pm 4 \mu\text{J}/\text{pulse}$ , where  $t = 0$  indicates the moment of laser breakdown. The plasma's waist (FWHM) is plotted vs. time b) for various pressures. Plasma expansion becomes hindered with increasing pressure until  $\sim 5$  bar is reached, at which point the plasma waist dwells before expanding.

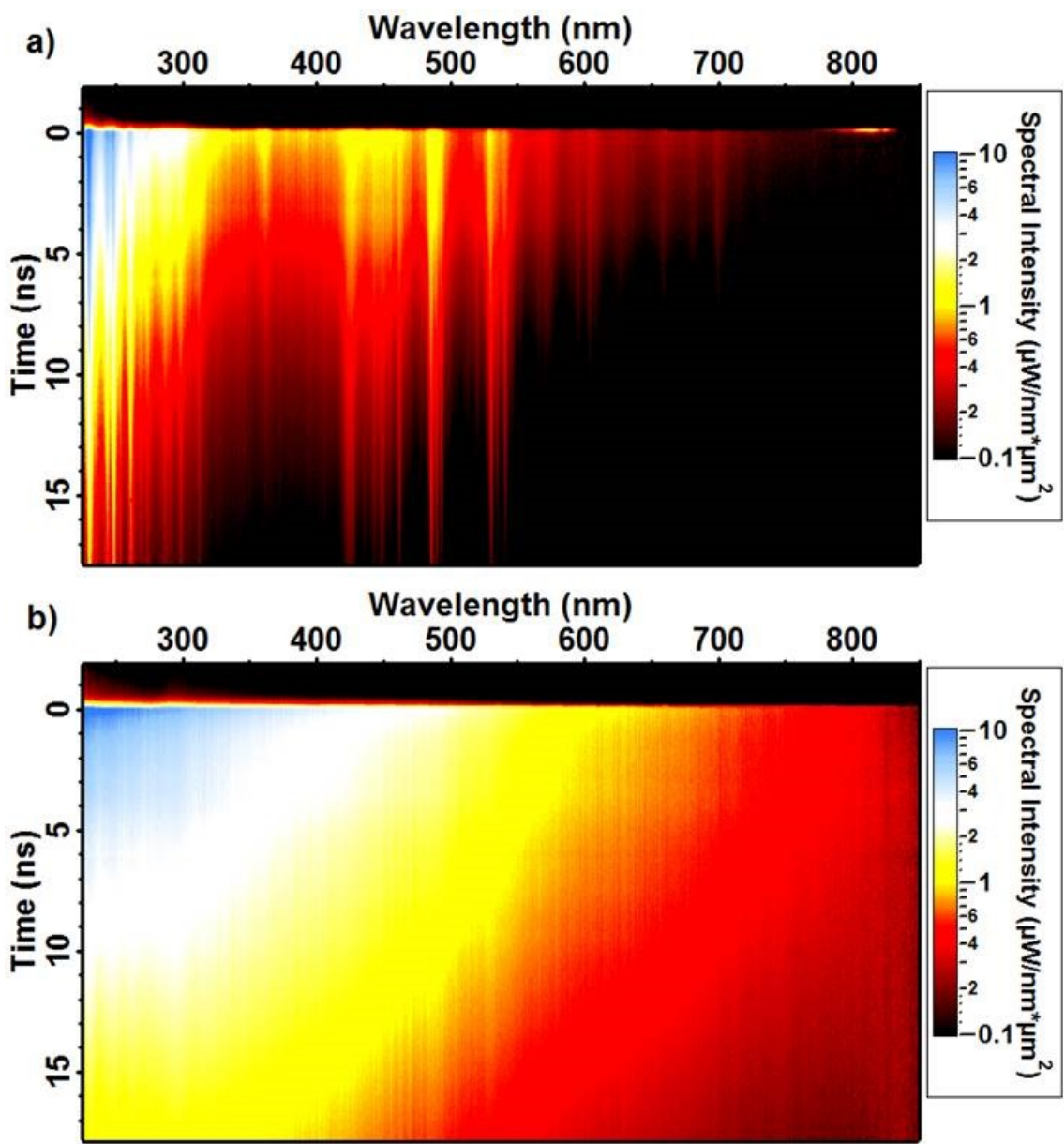


Figure 7.2: Calibrated spectrum vs. time for xenon breakdown at a) 0.5 and b) 5 bar using a laser energy of  $235 \pm 4 \mu\text{J}/\text{pulse}$ . Spectrum was acquired from a region of  $5.6 \times 5.6 \mu\text{m}$  located at the center of the plasma waist. At lower pressures, the plasma spectrum is dominated by atomic line emission. With increasing pressure, the spectrum is broadened until it becomes completely continuous ( $\sim 5$  bar). The absolute spectral intensity error is  $\sim 15\%$ .

intensity fluctuated by only  $\sim 10\%$  and optical triggering resulted in a minimal temporal jitter of 20 ps. Both streak and spectral images show the plasma emission as a function of time, where  $t_0 = 0$  ns marks the moment of laser breakdown. Indeed, laser-plasma scattering can enter the imaging system at the moment of breakdown and provide both a breakdown timestamp and a measurement for the system's temporal resolution. An example of this is present in Fig. 7.2a for  $t_0$  and at the laser wavelength of 825 nm.

A plasma's absolute spectral intensity provides important information regarding its opacity and mechanism of light emission. For this purpose, the imaging system was calibrated against known sources (Deuterium and QTH lamps) and corrected for solid angle. A temporal correction ( $< 30$  ps) was made to account for chromatic dispersion within the imaging optics. Finally, an intensity correction was applied due to chromatic aberration and tested against the known sources.

Spectral images were measured as a function of static pressure  $p_0$  for xenon, argon, and helium while maintaining a fixed laser power. For low  $p_0$  (Fig. 7.2a) the plasma spectrum is dominated by atomic lines for all times recorded. As  $p_0$  is increased, the continuum radiation rises while the atomic lines become heavily broadened. This trend continues until a critical pressure  $p_c$  is reached where the spectrum becomes completely continuous for early times (Fig. 7.2b), which has been observed in a similar system [35]. The gas-dependent value of  $p_c$  is  $\sim 5$ , 20, and 60 bar for xenon, argon, and helium, respectively. The continuous nature at  $p_c$  is visualized in Fig. 7.3, where individual spectra are extracted from Fig. 7.2b and plotted vs. wavelength. For  $p_0 = p_c$ , continuous emission persists for a characteristic timescale  $t_{\text{line}}$ . This timescale is also gas-dependent and is approximately 5, 1.5, and 0.15 ns for xenon, argon, and helium, respectively. For  $t > t_{\text{line}}$ , line emission emerges from the continuum and grows in strength relative to the continuum. This effect is observed in Fig. 7.3 for the Xe I transition line at 823 nm.

In the field of SL and SCP, testing spectra for opacity has proven to be a powerful technique for uncovering plasma properties [2, 57, 61, 56, 9, 88, 87]. The spectral intensity radiated by an ideal blackbody at temperature  $T$  is

$$I_\lambda = \frac{2\pi hc^2}{\lambda^5 \left( \exp \left\{ \frac{hc}{\lambda k_B T} \right\} - 1 \right)}. \quad (7.2.1)$$

Deviations from blackbody behavior is quantified by multiplying  $I_\lambda$  by an effective emis-

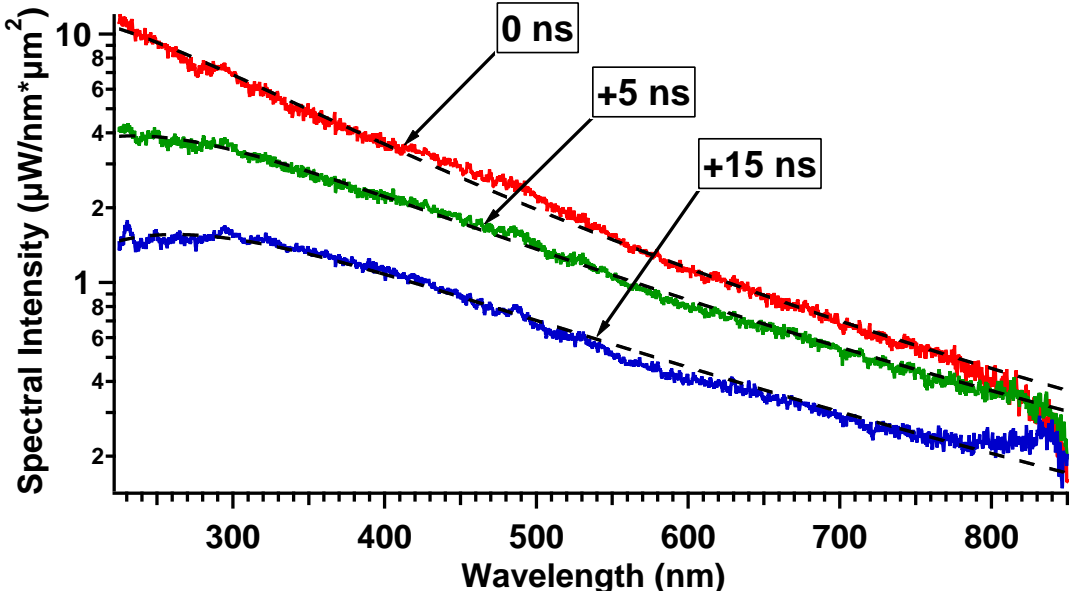


Figure 7.3: Spectral intensity for 5 bar xenon breakdown at different times relative to the plasma formation. Blackbody fits (dashed curves) are plotted for each spectrum with values of  $T = 16350, 12350$ , and  $11050$  K for  $t = 0, +5$ , and  $+15$  ns, respectively.

sivity  $\epsilon$ , where  $\epsilon = 1$  represents an ideal blackbody. Blackbody curves are presented in Fig. 7.3 and are well fit to the spectra.  $T$  and  $\epsilon$  from the blackbody fits are plotted vs. time in Fig. 7.4a. Blackbody behavior is observed as  $\epsilon > 0.8$  for  $t < 14$  ns and approaches  $\epsilon \approx 1$  at  $t \approx 5$  ns. Consistent with the definition of a blackbody as the ideal radiator at a given temperature, the emissivity in Fig. 7.4a never grows above unity even though the plasma temperature is decreasing exponentially! Further blackbody behavior is observed by measuring the emissivity value of the opaque 823 nm Xe I transition line  $\epsilon_{823}$ . Using the blackbody temperature, the intensity at 823 nm, and Eq. (7.2.1),  $\epsilon_{823}$  is plotted vs. time in Fig. 7.4a. For  $t > t_{\text{line}}$ , the plasma becomes increasingly transparent as indicated by the reduced emissivity and increased atomic line contribution to the spectrum. However, the emissivity for the strong 823 nm line remains opaque ( $\epsilon_{823} \approx 1$ ) for  $t > t_{\text{line}}$ . Like  $\epsilon$ ,  $\epsilon_{823}$  is never greater than unity which has been observed in other blackbody plasmas [57]. Blackbody behavior, along with an infrared opacity is also observed for 25 bar argon and 74 bar helium in Figs. 7.4b&c, respectively.

When the observed opacity is interpreted in terms of transport theory in SCP an

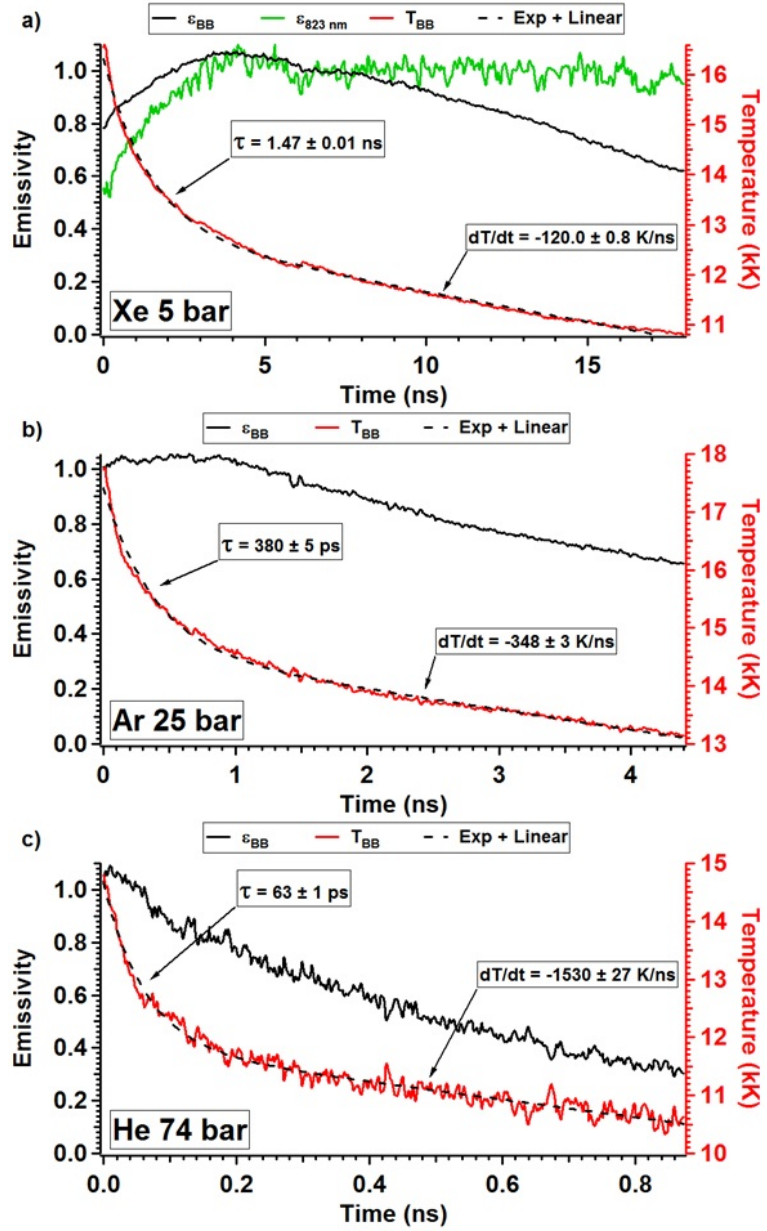


Figure 7.4: Plot of blackbody temperature (red curve) and effective emissivity (black curve) as a function of time for a) 5 bar xenon, b) 25 bar argon, and c) 74 bar helium. Laser energies of  $235 \pm 4$ ,  $325 \pm 3$ , and  $570 \pm 6 \mu\text{J}/\text{pulse}$  were used for xenon, argon, and helium, respectively. For all gases, the temperature initially decays exponentially and is followed by a long linear decay. A fit to an exponential+linear function is plotted (dashed curve) for each gas with characteristic timescales indicated. For xenon, the emissivity for the opaque Xe I transition is plotted (green curve) using the spectral intensity at 823 nm and the blackbody temperature.

estimate of the charge density can be obtained. A key condition for opacity is that the photon mean free path at a given wavelength must be smaller than the radiating body, written as  $\kappa R < 1$  where  $R$  is the plasma thickness and  $\kappa$  is the absorption coefficient of light. For dense plasma, the dominant form of absorption is the process of free-free inverse Bremsstrahlung where an electron absorbs light during a “collision” with an ion [106]. The collisionality in SCP is greatly affected by collective screening effects. In the presence of an oscillating electromagnetic field of frequency  $\omega$ , the collisionality is characterized by the unitless parameter  $\omega\tau_\omega$ , where  $\tau_\omega$  is the collision time of an electron with an ion. For an SCP in the multi-ionization regime [9]

$$\omega\tau_\omega = \left[ \frac{2}{\sqrt{6\pi}} \gamma^{1/2} \Gamma^{1/2} \Gamma_\omega \ln \left( \frac{0.7}{\sqrt{3}} \Gamma_\omega^{-3/2} + 1 \right) \right]^{-1}, \quad (7.2.2)$$

where  $\gamma$  is a unitless parameter representing the plasma frequency,  $\Gamma$  is the plasma coupling parameter, and  $\Gamma_\omega$  is the plasma coupling parameter in the presence of an electromagnetic field. These quantities are given by

$$\begin{aligned} \gamma &= \left( \frac{\omega_p}{\omega} \right)^2 = \frac{4\pi n_0 \bar{Z} e^2}{m_e \omega^2}, \quad \Gamma = \left( \frac{\bar{Z} e^2}{k_B T} \right) \left( \frac{4\pi n_0}{3} \right)^{1/3}, \\ \Gamma_\omega &= \Gamma \left[ \frac{k_B T}{\hbar \omega} \left( 1 - \exp \left( -\frac{\hbar \omega}{k_B T} \right) \right) \right], \end{aligned}$$

where  $\bar{Z} = n_e/n_0$  is the effective ionization level,  $n_0$  ( $n_e$ ) is the nuclei(electron) density, and  $m_e$  is the electron mass. For  $\bar{Z} < 1$ ,  $\Gamma = (e^2/k_B T) (4\pi \bar{Z} n_0/3)^{1/3}$ . The Coulomb logarithm in Eq. (7.2.2) represents screening effects and was found using a molecular dynamics simulation [22] and later supported in a laser-SL coupling experiment [9]. In the plasma regime where  $\gamma \ll 1 \ll \omega\tau_\omega$ , the absorption coefficient reduces to  $\kappa = \frac{\omega}{c} \frac{\gamma}{\omega\tau_\omega}$ . For 5 bar xenon breakdown at  $t = 5$  ns,  $T = 12350$  K,  $n_0 = 1.25 \times 10^{20}$  cm $^{-3}$ ,  $R = 50$   $\mu\text{m}$  (Fig. 7.1b), and selecting a spectral region relatively void of strong line emission (400 nm), an electron density of  $n_e > 4.0 \times 10^{20}$  cm $^{-3}$  is needed to satisfy the observed opacity ( $\kappa R \approx \pi$ ). This electron density requires over 3 levels of ionization and results in an SCP with  $\Gamma > 3.5$ . The initial attainment of such high levels of ionization is well known [96, 74]. We find that this level persists for an extended time and is a property of the equation of state of SCP.

The temporal evolution of the opaque spectrum yields the temperature as a function of time when  $\epsilon \approx 1$  (Fig. 7.4). This behavior can be connected to the transport in SCP, in particular the electron-ion collision time

$$\tau_{e-i} = \lim_{\hbar\omega \rightarrow 0} \tau_\omega = \left[ \frac{2}{\sqrt{6\pi}} \omega_p \Gamma^{3/2} \ln \left( \frac{0.7}{\sqrt{3}} \Gamma^{-3/2} + 1 \right) \right]^{-1}. \quad (7.2.3)$$

This is the timescale for electron-ion energy transfer and follows from Eq. 7.2.2 in the limit of no electric field. We argue that  $\tau_{e-i}$  accounts for the initial exponential drop in temperature soon after the laser-gas interaction. The intense laser pulse forms a plasma in the pressurized gas via the process of multiphoton ionization [72]. Recombination rapidly brings the electron density and light emission into LTE at the measured spectral temperature while leaving the ions cold. Due to their large mass, the ions take a longer time to heat up via collisions with the energetic electrons in a timescale  $\tau_{th} \approx \frac{M}{m_e} \tau_{e-i}$ , where  $M$  is the ion mass [106]. As the ions heat up the electron temperature drops exponentially (Fig. 7.4). For the range of  $\Gamma$  given above, Eq. 7.2.3 can be approximated as  $\omega_p \tau_{e-i} \approx 5.37$  matching [22]. For 5/25/74 bar Xe/Ar/He breakdown (Fig. 7.4a/b/c), the exponential coefficient for the initial temperature decay is 1470/380/63 ps. Using  $T=12350/14550/12550$  K,  $n_e=4.0/6.3/7.0 \times 10^{20}$  cm<sup>-3</sup> (required for opacity at 400 nm), and Eq. 7.2.3, the predicted thermalization time is consistent with  $\tau_{th}=1170/305/37$  ps. Comparison of all gases results in a  $\tau_{th}$  that is roughly linear to the ion mass. Normalizing to argon, the ratio of atomic masses is 3.3:1:0.10 (Xe:Ar:He). Similarly, the ratio of the measured decay time divided by  $\tau_{e-i}$  is 3.3:1:0.18, which is consistent with the screened theory of collisions in SCP as applied via Eq. 7.2.3 [22]. Had we used the collision time appropriate to dilute plasma theory we would have found  $\tau_{th}=160/71/5.2$  ps.

Although rapid ionization from high-intensity laser pulses has been achieved in a variety of systems [11, 23, 78], we further observe that a high level of ionization is maintained for a surprisingly long period of time. Is the persistent electron density due to local electronic thermodynamic equilibrium or far off-equilibrium behavior due to a long recombination time? In other words, is the plasma in ionization equilibrium at each time step in Fig. 7.4? To address this question, we consider the 3-body recombination timescale  $\tau_{rec}$  from plasma theory (photorecombination plays a minor role [106]) which occurs from

the capture of an electron by an ion in the presence of an additional electron, given by

$$\tau_{\text{rec}} = \left( \bar{v}_e \pi^2 r_0^5 \bar{Z}^4 n_0^2 \right)^{-1}, \quad (7.2.4)$$

where  $\bar{v}_e = \sqrt{8k_B T/m_e \pi}$  is the mean thermal electron speed and  $r_0 = \frac{2e^2}{3k_B T}$  is the impact parameter for recombination in a Coulomb collision. Eq. 7.2.4 and the plasma properties for xenon at  $t = 5$  ns results in an impossibly fast recombination time of 0.15 fs. This is a result of dilute plasma theory applied to the dense plasma which we study. In formulating Eq. 7.2.4, screening processes are not accounted for and will result in an overestimation of the probability of finding a second electron in the vicinity of the electron-ion collision. To this end, we account for screening by replacing  $r_0$  with the screened impact parameter  $\rho$  given by  $\sigma = \pi \rho^2 = \left( \bar{Z} n_0 \bar{v}_e \tau_{e-i} \right)^{-1}$ . The result of this substitution is that every electron-ion collision can result in a recapturing of the electron, and therefore  $\tau_{\text{rec}} \approx \tau_{e-i}$ . This timescale is still much faster than any experimental timescale and is necessarily smaller than  $\tau_{th}$ . We conclude the ionization is in a state of LTE with the electron temperature and light emission.

Ionization for an electron plasma in LTE is governed by Saha's equation given as

$$\frac{x_{m+1} x_e}{x_m} = \frac{2}{n_0} \frac{u_{m+1}}{u_m} \left( \frac{m_e k_B T}{2\pi\hbar^2} \right)^{3/2} \exp \left( -\frac{\chi_m}{k_B T} \right), \quad (7.2.5)$$

where  $x_m$  ( $x_e$ ),  $u_m$ , and  $\chi_m$  is the ion(electron) concentration, electronic partition function, and ionization potential for the  $m^{th}$  ion, respectively [40, 106]. Although the electrons and ions are at different temperatures for  $t < \tau_{th}$ , Eq. 7.2.5 still applies by using the electron temperature [19]. For 5 bar xenon at  $t \approx 5$  ns, the charge density is  $> 4 \times 10^{20} \text{ cm}^{-3}$  while the temperature is only  $\sim 12000$  K. According to Saha's equation, the degree of ionization for the first ionization level ( $m=0$  and  $\chi_1=12.1$  eV) should be less than 3%. Yet the opacity suggested by our data requires over 3 levels of ionization. Therefore, the collective processes at work in SCP must reduce the overall ionization potential by an amount comparable to  $\chi_3$ . In particular, the lowering of  $\chi_m$  through Debye screening results in a change of the average ionization potential by [40, 106]

$$\Delta \bar{\chi} = 2(\bar{Z} + 1)e^3 \sqrt{\frac{\pi \bar{Z} (\bar{Z} + 1) n_0}{k_B T}}. \quad (7.2.6)$$

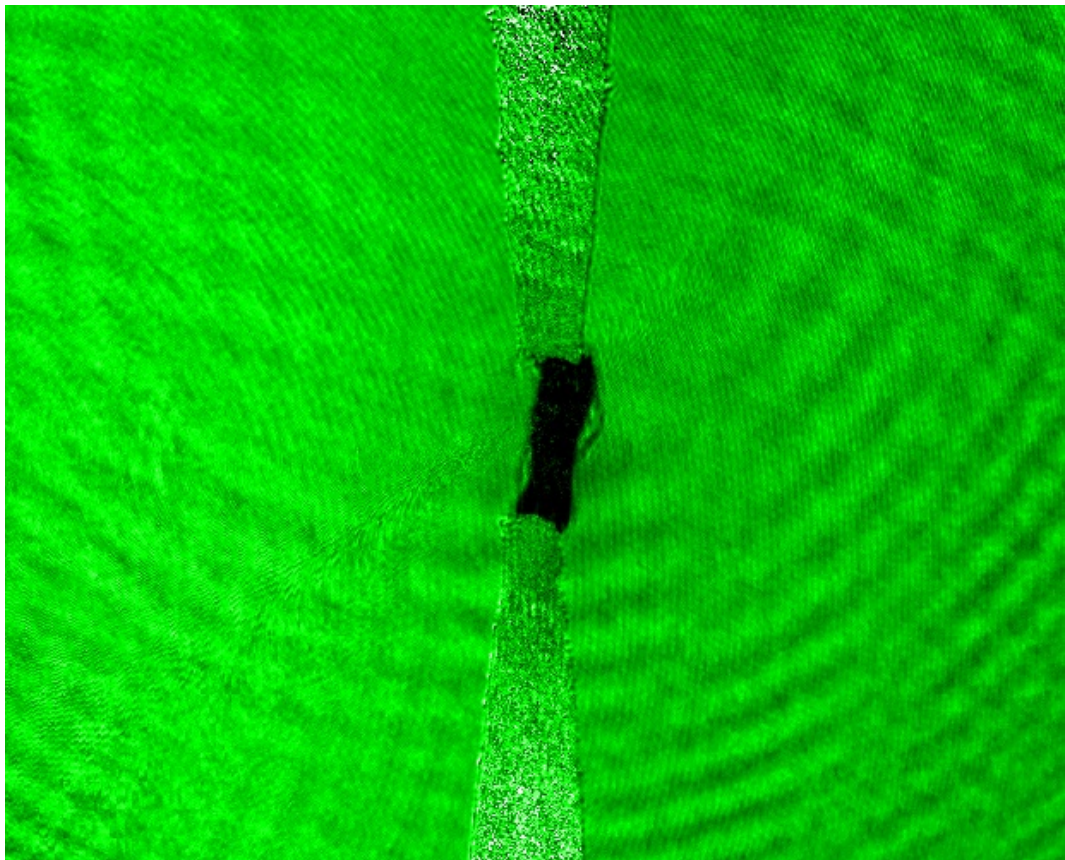
Using the measured plasma properties of xenon breakdown ( $\bar{Z}=3.2$ ), the ionization potential is dramatically reduced by  $\bar{\Delta\chi}=32$  eV. This value of potential reduction, albeit remarkably high, is consistent with the observed level of ionization as it lies between  $\chi_3=31.1$  eV and  $\chi_4=41.0$  eV.

Application of calibrated streaked spectral imaging to femtosecond laser breakdown in high-pressure gases reveals both transport and thermodynamic properties of strongly-coupled plasmas. We have used calibrated streaked spectral imaging to study laser-induced breakdown of high-pressure gases. We observe micron-scale blackbody spectra that persist long after the exciting laser has been turned off. Spectral analysis indicates the presence of a plasma with a degree of ionization much higher than follows from Saha's equation. We conclude a strongly-coupled LTE plasma is formed in an unexpected region of parameter space (defined by atomic density and temperature). The timescale for thermal relaxation depends strongly on plasma screening and its measurement discriminates between various theories, selecting in favor of [22]. Future work will study the dwell time and expansion of the strongly-coupled plasma. These systems may possibly reach regions of parameter space occupied by matter obeying quantum statistics. The discovery of an opaque microplasma as a thermodynamic state suggests electric discharges in pressurized gases as a new route toward optical switches.

We gratefully acknowledge support from DARPA MTO for research on micro-plasmas. We thank Brian Naranjo, Keith Weninger, Carlos Camara, Gary Williams, and John Koulakis for valuable discussions.

# **Chapter 8**

## **Spark Discharge in High-Pressure Gases**



## 8.1 Introduction<sup>1</sup>

The results from Chapter 7 show that the plasma phase transition can be recreated outside the phenomenon of sonoluminescence. This was accomplished by rapidly depositing energy into a high pressure gas using intense electromagnetic fields. However, the high expense and size of ultra-fast lasers limits many practical applications for this new phase of matter. So it is natural to ask, what other ways can energy be deposited into a high pressure gas? In this chapter a phenomenon known since classical antiquity is investigated as a new way of generating the plasma phase transition, the spark discharge.

As with the laser-breakdown experiment in Chapter 7, the spark discharge experiment relies on high pressure gas to achieve  $n_0 \sim 1 - 10 \times 10^{20}$  atoms/cm<sup>-3</sup>. Likewise, the timescale for energy transfer to the breakdown is crucial as hydrodynamic expansion lowers the plasma density. In this system, energy is delivered via electrons accelerating across a high voltage gap. Electrical resistivity (collisionality) randomizes the input energy and brings the system to T=24,000 K for a 10 bar xenon discharge. Using this temperature and  $\bar{Z} > 3$  as needed for opacity,  $\Gamma = 2$  which makes the spark discharge a source for strongly coupled plasmas.

In the experiment that follows, a new diagnostic technique is introduced into this thesis. Along with similar spectral analysis of the previous chapters, the absorption of light due to plasmas is measured. In this way, Kirchhoff's law is tackled from both sides and produces a truly convincing blackbody argument. This experiments shows that a spark discharge provides a means to creating on-demand dense plasma and functions as a fast optical switch.

---

<sup>1</sup>Chapter Image: A false-color microscope image of 10 bar xenon spark discharge. The photograph was backlit with a 3 ns laser pulse (532 nm) at the moment of peak plasma emission. The laser pulse is unimpeded by the surrounding gas (green background) and enters the imaging system, passing through a 532 nm line filter before exposing the camera. Laser light incident the blackbody spark plasma is completely absorbed (shadow in center) and does not make it to the camera. The shadows produced by the sharpened electrodes (center top and bottom) have been removed for clarity, although their outline can still be resolved. Broadband plasma emission is blocked by the line filter, thus giving the visual appearance of a “blackbody”.

## 8.2 A Nanosecond, High-Power, Dense, Microplasma Switch for Visible Light

In the field of sonoluminescence (SL), intense cavitation of gas bubbles within a fluid generates extreme conditions and the emission of light. Recent discoveries in SL have shown the emission originates from highly-ionized dense plasmas of micron scale [29, 57, 61, 56, 9]. Furthermore, this plasma is a new phase of matter that is characterized by its high ionization at unexpectedly low temperatures ( $\sim 1$  eV) [57]. A salient property of this microplasma is its opacity to visible light due to its high electron density ( $\sim 10^{21}$  cm $^{-3}$ ). This feature motivates its application as an active optical limiter. The direct use of SL as an optical switch has limited applications as it cannot be triggered on-demand. However, SL plasma originates from a thermodynamic state and can be reproduced in any system, regardless of how it's created. Indeed, a recent experiment has shown that the highly-ionized plasma phase can be generated using laser breakdown in high-pressure gases[8]. In this Letter we report on an optical switch generated by a spark discharge in high-pressure gases. The switch reported can block visible light in nanosecond timescales and is capable of high-power handling when subjected to intense laser pulses.

The application of high-voltage (HV) between two gas-separated electrodes can generate plasma through dielectric breakdown. This rapid breakdown is known as the spark discharge. Sparks can be developed in nanosecond timescales and heated to thousands of degrees through non-linear resistive heating [52]. At these temperatures, gases become ionized and radiate light. This rapid increase of light emission is shown in Fig. 8.1 for sparks generated in high-pressure xenon gas. Parallel to its light emission is a plasma's ability to absorb incoming light. The insets of Fig. 8.1 show images (10 ns gate) of spark plasmas absorbing light from a 532 nm pulsed laser. By delaying the moment of spark discharge relative to the laser pulse, the plasma's optical transmission was recorded as a function of time (left axis of Fig. 8.1). An intimate relationship exists between the emission and absorption of light by a body. This relationship is known as Kirchhoff's law of thermal radiation and can be written as

$$\frac{J_\nu}{A_\nu} = S_\nu = \frac{2\pi h\nu^3}{c^2} \frac{1}{e^{h\nu/kT} - 1}, \quad (8.2.1)$$

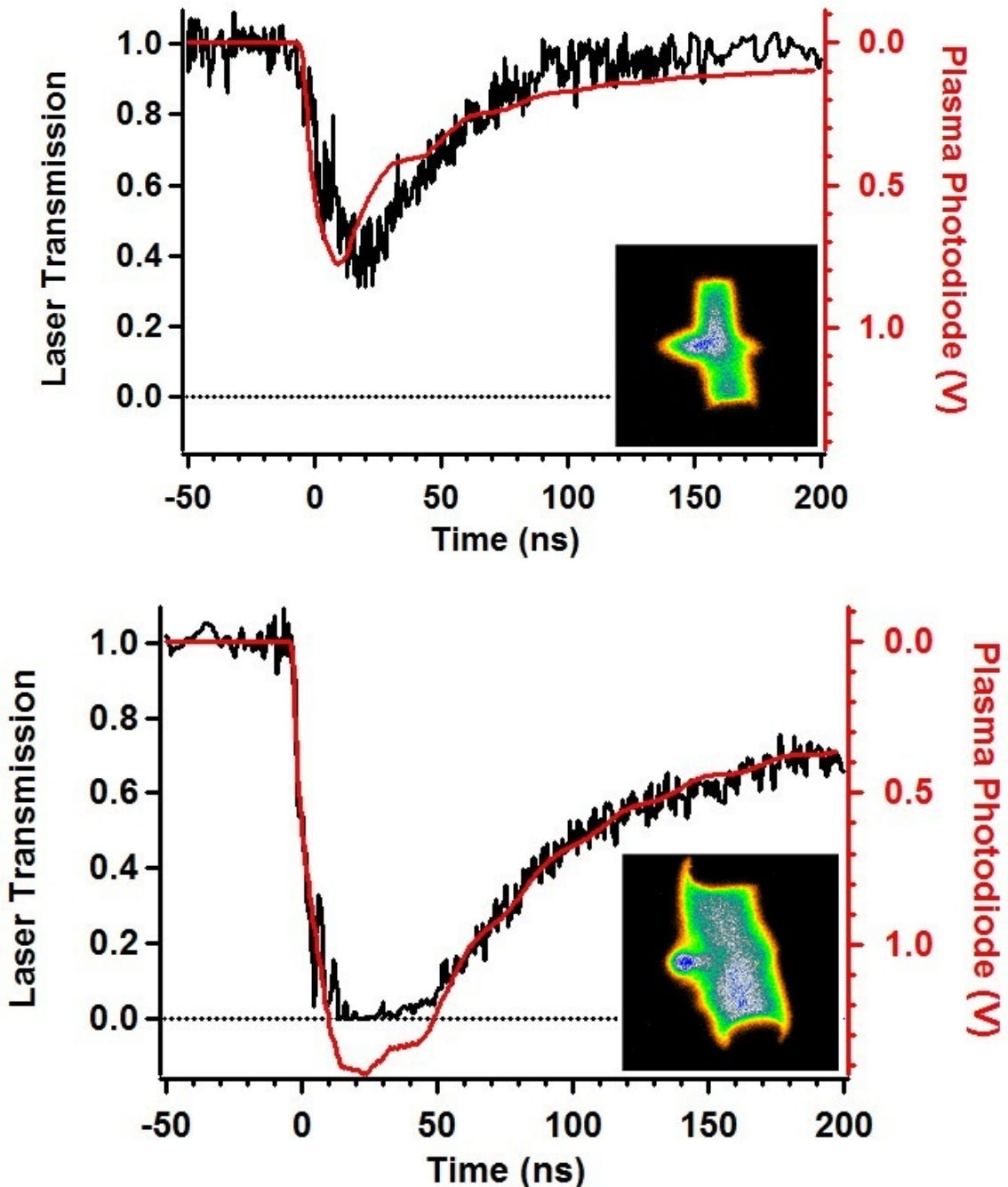


Figure 8.1: Laser transmission and plasma emission of spark discharges formed in a) 2 and b) 10 bar xenon gas as a function of time. Laser transmission (black curves) was recorded for 532 nm laser pulses focused through the center of the spark plasma. Plasma emission (red curves) was recorded with a fast photodiode. Insets show images taken with a framing camera during the moment of laser-plasma interaction. Laser absorption occurs within the spark volume and surface for 2 and 10 bar discharges, respectively.

where  $J_\nu$  is the amount of radiation emitted per unit time per unit surface area,  $A_\nu$  is the absorptivity, and  $S_\nu$  is the radiant energy flux of a blackbody at temperature  $T$  and frequency  $\nu$ . This law states that the ratio of a body's emission to its absorption is equal to blackbody emission, which only depends on  $T$  and  $\nu$ . Kirchhoff's law is beautifully represented in Fig. 8.1 as a strong correlation is observed between light emission and laser transmission (absorption) as a function of time. In general, plasma emission becomes more intense with increasing density [39]. This trend is observed in Fig. 8.1 for 2 versus 10 bar discharges. Similarly, the amount of transmitted laser energy decreases with increasing pressure. Eventually, a critical pressure is reached where the plasma becomes opaque and laser transmission falls to zero. For pressures  $\gtrsim 10$  bar, laser pulses are completely blocked and absorption occurs only on the plasma's surface (inset of Fig. 8.1b).

Spark discharges were generated using two tungsten needles (45  $\mu\text{m}$  tip radius) centered in a stainless-steel pressure chamber (PC), as shown in Fig. 8.2a. Optical access was granted with four UV fused-silica windows mounted on the PC. Distance between the electrode tips was adjusted with micron precision using a custom high-pressure actuator. Variable HV pulses were generated by an external circuit shown in Fig. 8.2c. A variable-length fast pulser (Behlke FSWP71-02, 1- ns rise time) was charged with a +5 kV power supply through a 10 M $\Omega$  resistor. Upon triggering, +5 kV pulses are sent through a transmission line ending with an SHV connection. Pulse lengths were set to 1  $\mu\text{s}$  for the discharges presented in this Letter. The HV electrode was connected to the external circuit through an NPT-to-SHV feed-through and the ground electrode was connected to the chamber body. Due to the voltage being near the breakdown threshold, 10 bar discharges jittered in time by 100s of nanoseconds relative to the input trigger. To improve the temporal jitter, seed electrons were created through the photoelectric effect by projecting a UV light source (D2 lamp) onto the electrodes [53].

The plasma images in Fig. 8.1 were acquired using a framing camera (Specialised-Imaging, Custom SIMD-052) capable of capturing four 3 ns images in a 12 ns interval. Plasma emission was collected and imaged onto the framing camera. Following Fig. 8.2b, plasma emission was collected by an infinity-corrected microscope objective (MO) and imaged onto the framing camera with a tube lens (Mitutoyo 10 $\times$  total magnification). A filter stack (FS) was placed between the objective and tube lens. In FS3 were neutral

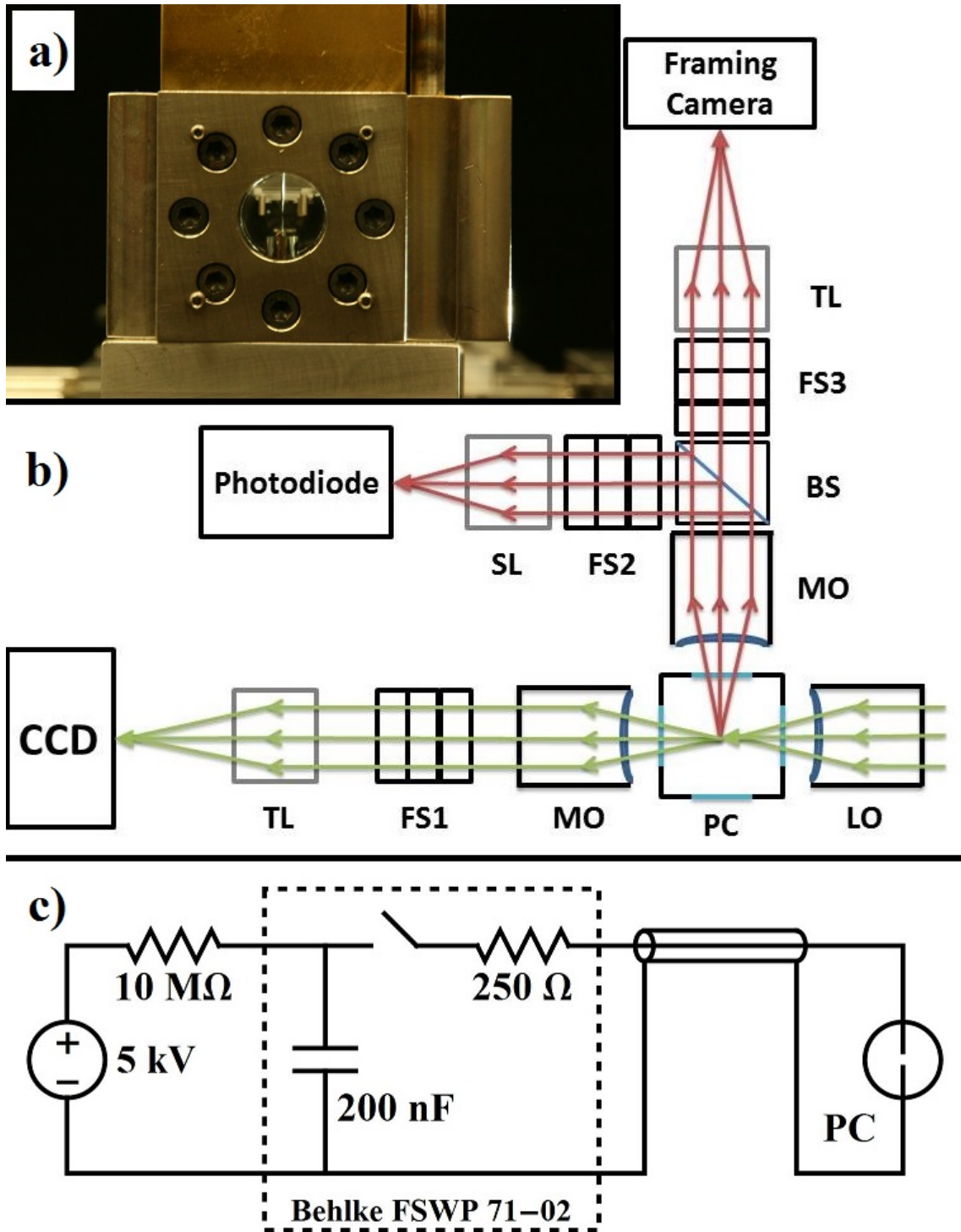


Figure 8.2: Experimental setup: a) Photograph of pressure chamber with tungsten needle electrodes. b) Optical block diagram for laser transmission, plasma emission, and fast spark imaging (framing). Included are laser (green arrows) and plasma emission (red arrows) ray traces. c) High-voltage circuit diagram.

density filters and a 532 nm notch filter to protect the framing camera from incidental laser scattering and pass broadband plasma emission.

Laser transmission curves from Fig. 8.1 were measured by focusing laser pulses through the spark discharge. TEM00 pulses from a seeded YAG were focused into the PC (green arrows in Fig. 8.2b) with a laser objective (LO). The measured flashwidth, energy, beam waist, and intensity at focus was  $2.18 \pm 0.15$  ns,  $8.02 \pm 0.88$   $\mu\text{J}/\text{pulse}$ ,  $4.24 \pm 0.02$   $\mu\text{m}$ , and  $2.63 \pm 0.29 \times 10^{10}$   $\text{W}/\text{cm}^2$ , respectively. After passing through the spark discharge at minimum focus, the laser is collected, filtered, and imaged onto a triggerable CCD camera (Mightex CCE-B013-U). In FS1 were neutral density filters and a 532 nm line filter to protect the camera from strong laser intensities and block broadband plasma emission. Transmission is normalized using the integrated laser intensity on the CCD for pulses arriving before the spark discharge.

A signal representing plasma emission (“Plasma Photodiode” in Fig. 8.1) was needed to sort the CCD and framing camera images as a function of time. In Fig. 8.2b, a beam splitter sends a portion of the plasma emission to a fast photodiode (1 ns rise time). The broadband light sent to the photodiode was filtered by FS2 (532 nm notch) and magnified  $0.6\times$  by a simple lens (SL). Timing signals from the plasma photodiode and cameras were recorded on an oscilloscope for every laser pulse. A timestamp was assigned for each event based on the time difference between the plasma photodiode and the cameras. Timing to each instrument was controlled through a delay generator (SRS DG645).

From Eq. 8.2.1, the condition for opacity is given by  $A_\nu = 1$  and therefore  $J_\nu = S_\nu$ . This states that an opaque body must emit blackbody radiation for a given frequency. The transmission curve for 10 bar discharges in Fig. 8.1b indicates complete absorption at 532 nm, and must therefore radiate as a blackbody at 532 nm. To confirm this requirement, calibrated spectrum was measured as a function of time as shown in Fig. 8.3. Temporally-resolved spectrum was acquired using a calibrated fiber-coupled spectrometer (Acton) and gated to 10 ns exposures with an ICCD (Princeton Instruments). Once more, a timestamp from the plasma photodiode is recorded for every discharge. In this way, spectra are sorted in time and averaged (2 ns time-bins) to make the spectral image in Fig. 8.3a. For early moments, the discharge radiates continuous broadband spectrum followed by xenon line emission. Temporal line-outs from the spectral images are shown

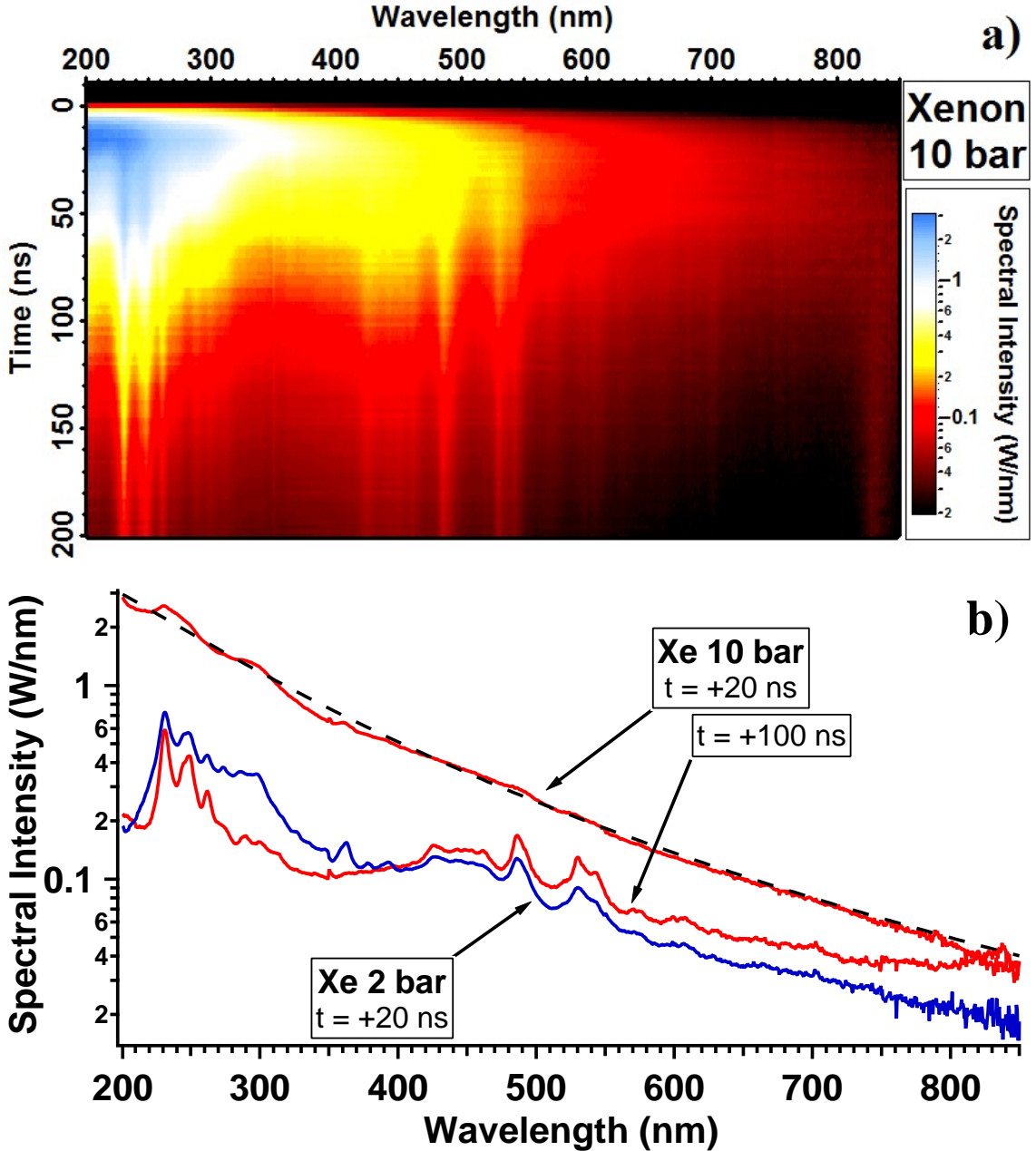


Figure 8.3: Calibrated spectrum for 10 bar xenon discharges. a) Temporally-resolved spectral image shows continuous broadband emission for early times. As the plasma expands, xenon line emission emerges from the continuum for later times. b) Spectral line-outs reveal opaque behavior during the early moments of discharge and is well fit to blackbody emission (black dashed curve). Blackbody spectrum is observed concurrently with complete absorption from Fig. 8.1b.

in Fig. 8.3b. Indeed, this spectrum is well fit to blackbody emission ( $S_\nu$ ) during the same moments as complete laser absorption (Fig. 8.1b). Because the spectrum is calibrated in intensity, the fit in Fig. 8.3b provides both the blackbody's temperature (24000 K) and area of emission ( $4.9 \times 10^4 \mu\text{m}^2$ ). This is in excellent agreement with the plasma's luminous area ( $2\pi Rh = 2\pi (43 \mu\text{m})(173 \mu\text{m}) = 4.7 \times 10^4 \mu\text{m}^2$ ) taken with the framing camera images. For times  $\gtrsim 50$  ns, xenon lines emerge from the continuum and increase in strength. These lines represent a transparent plasma and is consistent with the absorption measurement in Fig. 8.1b. This increase in line emission is due primarily to the plasma's hydrodynamic expansion into the surrounding gas, resulting in a lowered atomic density. For comparison, spectrum at 2 bar xenon discharge is provided in Fig. 8.3b and shows reasonable agreement.

Transmission curves were constructed for laser intensities spanning 7 orders of magnitude ( $2.6 \times 10^7 - 10^{13} \text{ W/cm}^2$ ). These curves were independent of laser intensity until the laser breakdown threshold was reached. Laser breakdown occurred at  $1.0 \pm 0.1 \times 10^{12} \text{ W/cm}^2$  and  $2.6 \pm 0.3 \times 10^{11} \text{ W/cm}^2$  for 2 and 10 bar, respectively. This further indicates that the loss of laser light is due to linear absorption by the spark plasma. Beyond the laser breakdown threshold, the transmission curves deviated toward lower transmission due to energy loss from laser breakdown [10]. This trend suggests that there is no limit to the plasma's power handling capability and can be utilized at very high laser intensities. Fig. 8.4 shows framing images of 10 bar spark-laser interactions for a laser intensity ten times larger than laser breakdown ( $2.6 \times 10^{12} \text{ W/cm}^2$ ). Each image was exposed for 10 ns with 0 ns interframe time. In Fig. 8.4a, the incident laser pulse (from left to right) is focused between the tungsten electrodes with the spark switched off (no HV). In this configuration, laser breakdown is formed both before and after the electrodes and  $\sim 10\%$  of the laser energy is transmitted to the CCD camera. With the spark activated, the laser pulse slams into the plasma column and is completely absorbed (Fig. 8.4b). Once more, no laser energy passes through to the CCD camera for early times ( $\sim 0 - 50$  ns after spark initiation). Laser energy is absorbed only on the surface of the spark plasma and is a further indication of an opaque body. The laser energy deposited to the spark plasma is so large that a luminous wave propagates within the plasma (from left to right in Fig. 8.4b). Conversely, laser energy is deposited to the plasma volume at later times as

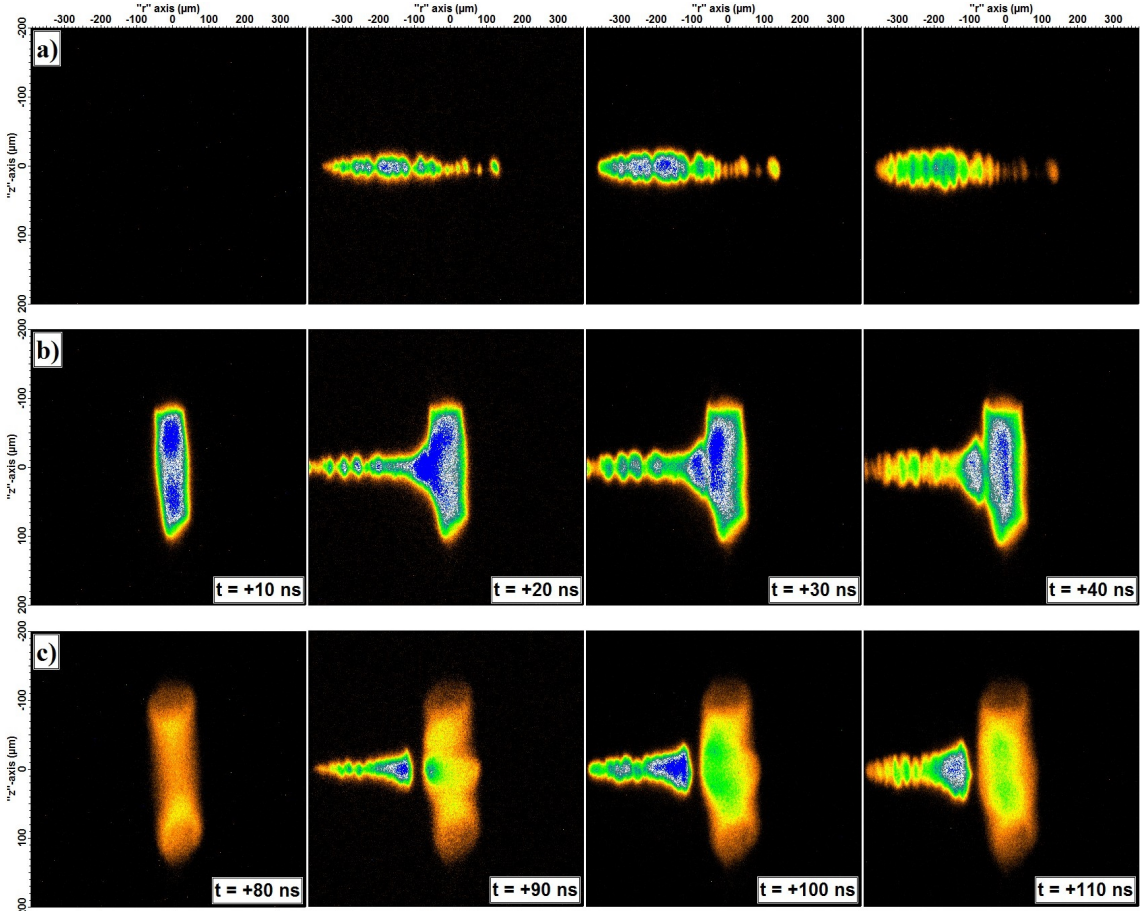


Figure 8.4: 10 ns framing images of a) laser breakdown without a spark and b) laser absorption at +20 ns and c) +90 ns after spark discharge initiation in 10 bar xenon gas. In all cases, the laser was set to  $2.6 \times 10^{12} \text{ W/cm}^2$  and centered between the electrode gap. A dark region exists between the laser breakdown and spark plasma for  $t \gtrsim 50 \text{ ns}$  and grows larger with later laser pulses. Shadowgraph measurements have shown this effect is due to laser breakdown induced by a shock front generated by the spark discharge.

shown in Fig. 8.4c. Here too a luminous wave propagates within the plasma (from middle to top/bottom in Fig. 8.4c). This observation is consistent with both the measured spectrum and absorptivity, as a volume emitter is also a volume absorber.

The discovery of a highly-ionized microplasma as a thermodynamic state has motivated its reproduction outside of sonoluminescence. We have successfully generated an opaque plasma using spark discharges in high-pressure xenon and is activated within 10 ns of triggering. As an active optical limiter, this plasma has seemingly limitless power handling as laser energy is converted into generating ever more plasma. In other words, the switch reported in this Letter cannot be damaged because it is already broken. This novel optical switch can now be optimized in parameter space for faster discharge speeds, lower energy consumption, and longer periods of opacity.

We gratefully acknowledge support from DARPA MTO for research on micro-plasmas. We thank Brian Kappus, Brian Naranjo, and Guillaume Plateau for valuable discussions.

# Chapter 9

## Conclusion

The plasma phase transition has been successfully generated using three vastly different mechanisms. A commonality in all plasmas are their inherent non-linear nature, and it's no surprise that we can generate them using non-linear effects. In this thesis, the plasma phase transition is generated through the following non-linear mechanisms:

1. Through the adiabatic heating and compressing of bubbles using non-linear fluid dynamics.
2. Through optical breakdown in high pressure gases using non-linear electromagnetic absorption.
3. Through electrostatic breakdown in high pressure gases using non-linear resistive heating.

In each case, energy is deposited into a high density gas of micron size. The end result is a new thermodynamic state characterized by its high ionization and opacity. By generating the plasma phase transition in various systems, we can use many different diagnostics and probing techniques. These techniques have already provided information on the temperature, electron density, and transport properties for this new state of matter. The theory of ionization is now extended to multiple levels of ionization and is shown to be consistent with the measured plasma properties.

The question of sonoluminescence's universality has been addressed and much knowledge has been gained by exploring this new phase of matter. However, questions still remain and new ones are formed:

- The screening model (“Daligault”) used to describe transport properties conflicts with the model (“Debye”) used to describe the thermodynamic ionization level. This high level of ionization requires a Debye screening length that is smaller than the interatomic spacing. And yet, the transport measurements show that Daligault’s formulation to be the correct form. This suggests the interatomic spacing as the screening length. How can these two observations co-exist?
- Although much has been discovered, the plasma phase transition theory is incomplete as nothing is included to prevent runaway ionization. What prevents this runaway from occurring?

These questions warrant future investigation and can extend our understanding of strongly coupled plasmas. Sonoluminescence has escaped its liquid confines and is ready to give up its secrets.

# Appendix A

## Derivation of the Electron-Ion Collision Time

The following derivation of the electron-ion collision time is taken from Zel'dovich and Raizer [106] and differs from 4.0.1 by a numerical constant on the order of unity.

Consider a collision with an electron (mass  $m$  and charge  $-e$ ) and an ion (mass  $M$  and charge  $Ze$ ) which pass each other at a distance  $r$  and a relative velocity of  $v$  (Fig. A.1). The force acting on the particles is of the order

$$F \sim \frac{(-e)(Ze)}{r^2} = \frac{-Ze^2}{r^2}.$$

The amount of time in which this force is acting on the particles is of the order  $t \sim \frac{r}{v}$ . The relative velocity change due to this force in this amount of time is of the order

$$\Delta v \sim Ft \frac{m+M}{mM} \approx \frac{-Ze^2}{mvr}$$

where the approximation  $M \gg m$  is applied. The square of the velocity change is the desired quantity as the electron-ion collision timescale is a timescale for energy transfer. This is given by

$$(\Delta v)^2 \sim \frac{Z^2 e^4}{m^2 v^2 r^2}.$$

For an ion density  $n_i$ , the probability of a collision is proportional to  $2\pi r dr$ . The rate of

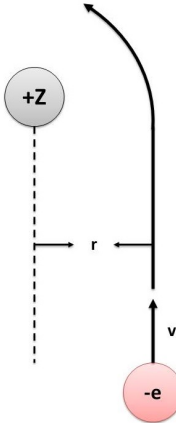


Figure A.1: Collision trajectory for an electron incident on an ion.

change is given by

$$\frac{d(\Delta v)^2}{dt} \sim n_i v \int_{r_{min}}^{r_{max}} (\Delta v)^2 2\pi r dr \sim \frac{2\pi n_i Z^2 e^4}{m^2 v} \ln \Lambda,$$

where  $\ln \Lambda$  is the Coulomb logarithm given by the limits of integration  $r_{max}$  and  $r_{min}$  ( $\Lambda \equiv \frac{r_{max}}{r_{min}}$ ). The limits of integration prevent a divergence in the radial integral and is determined by various models of screening (see Appendix B). Finally, the collision time can be defined as the timescale needed for  $(\Delta v)^2$  to change by  $v^2$  such that

$$\tau_{e-i} = v^2 \frac{dt}{d(\Delta v)^2} = \frac{1}{v} \frac{(mv^2)^2}{2\pi n_i Z^2 e^4 \ln \Lambda}. \quad (\text{A.0.1})$$

For the ion and electron temperatures studied in this thesis ( $v_e \gg v_i$ ), the mean thermal electron speed  $\bar{v} = \sqrt{\frac{8k_B T}{m\pi}}$  is used in place of  $v$  and  $mv^2$  is given by  $3k_B T$ . Introducing the plasma parameter  $\Gamma = \frac{eZ}{k_B T} \left( \frac{4\pi n_i}{3} \right)^{1/3}$  and the plasma frequency  $\omega_p = \sqrt{\frac{4\pi Z n_i e^2}{m}}$ , Eq. A.0.1 can be re-written as

$$\tau_{e-i} = 3 \left[ \frac{2}{\sqrt{6\pi}} \omega_p \Gamma^{3/2} \ln \Lambda \right]^{-1}, \quad (\text{A.0.2})$$

which differs from 4.0.1 by a factor of 3.

## Appendix B

# Derivation of Coulomb Logarithm

The Coulomb logarithm stems from the integration of the impact parameter for electron-ion collisions in plasmas. At its core, this term represents the effects of electrostatic screening which acts to shield-out long-distance collisions. The three screening models addressed in this thesis represent no, intermediate, and strong screening. Below is an alternative derivation of the Coulomb logarithm using the screened impact parameter  $\rho$  for the three cases with

$$\tau_{e-i} = (\bar{v}_e \pi \rho^2 n_i)^{-1} = \left[ \frac{2}{\sqrt{6\pi}} \omega_p \Gamma^{3/2} \ln \Lambda \right]^{-1}. \quad (\text{B.0.1})$$

### B.1 “Dilute” Model:

For plasmas whose constituent particles are weakly-interacting, screening is a weak and has only a logarithmic effect of the collision time. This is known as the “Dilute” model of screening and is given by

$$\ln \Lambda = \ln \left( \frac{\delta_D}{R_c} \right) = \ln \left( \frac{\Gamma^{-3/2}}{\sqrt{6}} \right), \quad (\text{B.1.1})$$

where  $\delta_D = \sqrt{\frac{k_B T}{8\pi n_e e^2}}$  is the Debye length,  $\Gamma = \frac{e^2}{k_B T} \left( \frac{4\pi n_e}{3} \right)^{1/3}$  is the plasma parameter, and  $R_c \equiv \frac{e^2}{k_B T}$  is the distance of closest approach, the distance at which the electrostatic and kinetic energies are equal and energy transfer is largest. In the temperatures explored in this thesis, the ionization level in the “Dilute” model is less than unity and  $n_e = n_i$ . This

form of the Coulomb logarithm is commonly used in plasma physics and is often set to a constant. Setting  $\ln \Lambda = 1$  results in

$$\tau_{e-i} = \left[ \frac{2}{\sqrt{6\pi}} \omega_p \Gamma^{3/2} \right]^{-1} \propto n_e^{-1} T^{3/2}.$$

Comparing this to the relationship of Eq. B.1.1 gives

$$\rho = \left( \frac{2}{3} \right)^{1/2} R_C.$$

In terms of a hard-sphere model, the collision parameter is proportional to the radius of closest approach in the “Dilute” model.

## B.2 “Daligault” Model:

An intermediate level of screening is realized in the “Daligault” model [22] and is given by

$$\ln \Lambda = \ln (0.7\Lambda + 1) = \ln \left( 0.7 \frac{\Gamma^{-3/2}}{\sqrt{3}} + 1 \right), \quad (\text{B.2.1})$$

where  $\sqrt{6}$  is replaced by  $\sqrt{3}$  according to [22]. In the dense limit where  $0.7 \frac{\Gamma^{-3/2}}{\sqrt{3}} \ll 1$ ,

$$\tau_{e-i} \approx \left[ \frac{2(0.7)}{6\sqrt{\pi}} \omega_p \right]^{-1} \propto n_e^{-1/2}.$$

Comparing this to the relationship of Eq. B.2.1 gives

$$\rho = \left( \frac{1.4}{9} \right)^{1/2} \left( \frac{a}{\delta_D} \right)^{1/2} a,$$

where  $a = \left( \frac{4\pi n_i}{3} \right)^{1/3}$  is the interionic spacing. In terms of a hard-sphere model, the collision parameter is proportional to the interionic spacing in the “Daligault” model, which is similar to the “ion-sphere” model.

## B.3 “Debye” Model:

A strong level of screening is realized in the “Debye” model and is given by

$$\ln \Lambda = \ln \sqrt{\Lambda^2 + 1} = \frac{1}{2} \ln \left( \frac{\Gamma^{-3}}{6} + 1 \right). \quad (\text{B.3.1})$$

In the dense limit where  $\frac{\Gamma^{-3}}{6} \ll 1$ ,

$$\tau_{e-i} \approx \left[ \frac{2}{12\sqrt{6\pi}} \omega_p \Gamma^{-3/2} \right]^{-1} \propto T^{-3/2}.$$

Comparing this to the relationship of Eq. B.3.1 gives

$$\rho = \left( \frac{1}{3} \right)^{1/2} \delta_D,$$

In terms of a hard-sphere model, the collision parameter is proportional to the Debye length in the “Debye” model.

# Appendix C

## Derivation of Inverse Bremsstrahlung

### C.1 Drude model

The Drude model is an application of kinetic theory which describes electronic motion in a sea of fixed (heavy) ions. This model does not include long range interactions and has an assumed collision time,  $\tau$ . Below are the key assumptions made for this derivation:

1. The plasma is infinite and homogenous.
2. The ions have infinite mass.
3. There are no external static electric or magnetic fields.
4. The electromagnetic phase velocity is much faster than the electron thermal velocity.

#### C.1.1 Electronic equation of motion

$$\dot{\mathbf{v}} = -\frac{e\mathbf{E}}{m_e} - \frac{\mathbf{v}}{\tau} \quad (\text{C.1.1})$$

Here,  $\dot{\mathbf{v}}$ ,  $-e$ , and  $m_e$  is the electron's velocity, charge, and mass respectively.  $\mathbf{E}$  is the electric field and  $\tau$  is the effective time between electron-ion collisions.  $\tau$  must be provided

for the Drude model. Maxwell's equations are now coupled to the equation of motion and are given by

$$\vec{\nabla} \cdot \tilde{\mathbf{E}} = -4\pi e n_e, \quad (\text{C.1.2})$$

$$\vec{\nabla} \cdot \tilde{\mathbf{B}} = 0, \quad (\text{C.1.3})$$

$$\vec{\nabla} \times \tilde{\mathbf{E}} = -\frac{\dot{\mathbf{B}}}{c}, \quad (\text{C.1.4})$$

$$\vec{\nabla} \times \tilde{\mathbf{B}} = \frac{\dot{\mathbf{E}}}{c} - \frac{4\pi e n_e \mathbf{v}}{c}, \quad (\text{C.1.5})$$

Now, we assume a propagating wave solution for  $\mathbf{E}$ ,  $\mathbf{B}$ , and  $\mathbf{v}$ ,

$$\begin{Bmatrix} \mathbf{E}(\mathbf{r}, t) \\ \mathbf{B}(\mathbf{r}, t) \\ \mathbf{v}(\mathbf{r}, t) \end{Bmatrix} = \begin{Bmatrix} \mathbf{E} \\ \mathbf{B} \\ \mathbf{v} \end{Bmatrix} \exp [(\mathbf{k} \cdot \mathbf{r} - \omega t) i]. \quad (\text{C.1.6})$$

Putting these solutions into equations 1-5 leads to

$$\mathbf{v} = \frac{e\mathbf{E}}{m_e} \frac{\tau}{i\omega\tau - 1}, \quad (\text{C.1.7})$$

$$i\mathbf{k} \cdot \mathbf{E} = -4\pi e n_e, \quad (\text{C.1.8})$$

$$i\mathbf{k} \cdot \mathbf{B} = 0, \quad (\text{C.1.9})$$

$$i\mathbf{k} \times \mathbf{E} = \frac{i\omega \mathbf{B}}{c}, \quad (\text{C.1.10})$$

$$i\mathbf{k} \times \mathbf{B} = -\frac{i\omega \mathbf{E}}{c} - \frac{4\pi e n_e \mathbf{v}}{c}. \quad (\text{C.1.11})$$

If we take Eq. C.1.11 and apply  $\times \mathbf{k}$  and utilize the vector identity  $\mathbf{A} \times (\mathbf{B} \times \mathbf{C}) = \mathbf{B}(\mathbf{A} \cdot \mathbf{C}) - \mathbf{C}(\mathbf{A} \cdot \mathbf{B})$  on the RHS we obtain

$$\frac{i\omega}{c} \left( \frac{\omega}{c} \mathbf{E} + \frac{4\pi e n_e \mathbf{v}}{ic} \right) = i\mathbf{E} \parallel \mathbf{k} \parallel^2 - i(\mathbf{k} \cdot \mathbf{E}) \mathbf{k}. \quad (\text{C.1.12})$$

Finally, substitute Eqs. C.1.7 and C.1.8 into Eq. C.1.12 to obtain

$$(\mathbf{k} \cdot \mathbf{E}) \mathbf{k} - \left[ k^2 - \frac{\omega^2}{c^2} + \frac{\omega_p^2}{c^2} \left( \frac{\omega^2 \tau^2}{1 + \omega^2 \tau^2} - \frac{\omega \tau}{1 + \omega^2 \tau^2} i \right) \right] \mathbf{E} = 0.$$

Therefore, the dispersion relation (for transverse waves) is

$$k^2 = \frac{\omega^2}{c^2} \left[ (1 - \gamma \beta) + \frac{\gamma \beta}{\omega \tau} i \right], \quad (\text{C.1.13})$$

$$\gamma = \frac{\omega_p^2}{\omega^2}, \quad \beta = \frac{\omega^2 \tau^2}{1 + \omega^2 \tau^2}, \quad \omega_p = \sqrt{\frac{4\pi e^2 n_e}{m_e}}$$

### C.1.2 Limits: $\omega \tau \gg 1$

In the limit of high driving frequency compared to the collision frequency,  $\beta \simeq 1$  and the dispersion relation becomes

$$k = \pm \frac{\omega}{c} \left[ (1 - \gamma) + \frac{\gamma}{\omega \tau} i \right]^{1/2}. \quad (\text{C.1.14})$$

In the limit of  $\omega \tau \gg 1$  and  $|1 - \gamma| \gg \frac{\gamma}{\omega \tau}$  which is equivalent to  $\omega \tau \gg (\gamma^{-1} - 1)^{-1}$ , the dispersion relation can be expanded in the square root to give

$$k \simeq \frac{\omega}{c} (1 - \gamma)^{1/2} \left[ 1 + (1 - \gamma)^{-1} \frac{\gamma}{2\omega \tau} i \right]$$

$$k \simeq \frac{\omega}{c} \left[ (1 - \gamma)^{1/2} + (1 - \gamma)^{-1/2} \frac{\gamma}{2\omega \tau} i \right]$$

**NOTE: The above approximation fails when  $\omega \approx \omega_p$  !!!**

Finally, to find the absorption by inverse Bremsstrahlung, we simply take twice the imaginary part of  $\mathbf{k}$ ,

$$\kappa = \frac{\omega}{c} \frac{\gamma}{\omega \tau} \frac{1}{|1 - \gamma|^{1/2}}. \quad (\text{C.1.15})$$

### C.1.3 Limits: $\omega \tau \gg 1$ and $\gamma \ll 1$ ( $\omega \gg \omega_p$ )

In the limit of high driving frequency compared to both the collision and plasma frequencies, the dispersion relation is simply

$$\kappa = \frac{\omega}{c} \frac{\gamma}{\omega\tau}. \quad (\text{C.1.16})$$

This is the absorption coefficient most commonly seen in plasma textbooks (Zel'dovich, etc.). As the collision time is  $\propto \gamma^{-1/2}$ , the absorption coefficient is  $\propto \gamma^{3/2} = \left(\frac{\omega_p}{\omega}\right)^3$ .

#### C.1.4 Limits: $\omega\tau \gg 1$ and $\gamma \gg 1$ ( $\omega \ll \omega_p$ )

In the limit of high driving frequency compared to the collision frequency, but smaller than the plasma frequency, the dispersion relation is simply

$$\kappa = \frac{\omega}{c} \frac{\gamma^{1/2}}{\omega\tau}. \quad (\text{C.1.17})$$

Interestingly enough, the absorption coefficient is now  $\propto \gamma = \left(\frac{\omega_p}{\omega}\right)^2$ .

## C.2 Dawson derivation

In 1962, John Dawson and Carl Oberman published their seminal work in *The Physics of Fluids* [20]. This work derives the absorption coefficient (inverse Bremsstrahlung) of a fully-ionized plasma. The plasma model they adopt to describe the electron dynamics is through the Vlasov-Poisson equations. Unlike the Drude model, this derivation makes no assumptions for the quantity  $\tau$  and in fact solves for the close and far “collisions” of electrons impacting ions. This derivation not only solves the dispersion relation, it also solves for  $\tau$ . The solution to the Vlasov-Poisson equations is used to calculate the plasma’s complex impedance,  $Z(\omega)$ . Once  $Z(\omega)$  is known, the dispersion relation can be calculated using the following relationship given by Maxwell’s equations together with Ohm’s Law

$$k^2 = \left(\frac{\omega^2}{c^2}\right) \left[1 - \frac{4\pi i}{\omega Z(\omega)}\right].$$

The absorption coefficient ( $\kappa$ ) is then simply twice the imaginary part of  $k$ . The quantity  $Z(\omega)$  is a complicated integral function which can be solved analytically for the limits of  $\gamma \gg 1$  and  $\gamma \ll 1$ . In 1973, Johnston and Dawson published in *The Physics of Fluids* [55] a correction to the values of  $\kappa$ .

$$\kappa = \frac{16\pi Z^2 n_e n_i e^6 \ln \Lambda(\nu)}{3c\nu^2 (2\pi m_e k_B T)^{3/2}} \frac{1}{|1 - \frac{\nu_p^2}{\nu^2}|^{1/2}} = \frac{\omega}{c} \frac{\gamma}{\omega\tau} \frac{1}{|1 - \gamma|^{1/2}}, \quad (\text{C.2.1})$$

$$\tau = \left( \frac{2}{\sqrt{6}\pi} \omega_p \Gamma^{3/2} \ln \Lambda(\omega) \right)^{-1}, \quad (\text{C.2.2})$$

$$\Gamma \equiv \left( \frac{e^2}{k_B T} \right) \left( \frac{4\pi n}{3} \right)^{1/3},$$

where  $\Lambda(\omega)$  = minimum of  $\frac{v_T}{\omega_p p_{min}}$ ,  $\frac{v_T}{\omega p_{min}}$ . Here,  $p_{min}$  is the minimum impact parameter for electron-ion collisions and is at the heart of the screening process in dense plasma. Dawson gives  $p_{min}$  = maximum of  $\frac{Ze^2}{k_B T}$ ,  $\frac{\hbar}{(m_e k_B T)^{1/2}}$  which is  $\frac{Ze^2}{k_B T}$  for  $T < 27\text{eV}$ . This leaves the following conditions,

$$\begin{cases} \Lambda(\omega) = \frac{1}{\sqrt{6}} \Gamma^{-3/2} & \text{for } \omega_p \gg \omega, \\ \Lambda(\omega) = \frac{\omega_p}{\omega} \frac{1}{\sqrt{6}} \Gamma^{-3/2} & \text{for } \omega_p \ll \omega. \end{cases}$$

The first limit results in the dilute Coulomb logarithm term as given by most authors. The second limit (high frequency limit) has an added factor of  $\gamma^{1/2}$ . This extra factor will not have a strong effect in dilute plasma ( $\Gamma \ll 1$ ) as the logarithm becomes a weak function. However, this term will become significant in strongly-coupled plasma ( $\Gamma \geq 1$ ) as will be discussed in the Conclusions section.

The results of the Dawson derivation are identical to that of the Drude model (Eq. C.2.1 = Eq. C.1.15) and a formula for  $\tau$  is generated. As will be shown in the next section, this formulation for  $\tau$  differs to that of Zel'dovich and Landau by a factor of  $\frac{\hbar\omega}{k_B T} \left( 1 - \exp \left( -\frac{\hbar\omega}{k_B T} \right) \right)$  which is due to the effects of stimulated emission.

### C.3 Zel'dovich and Landau derivation

In Chapter V.2-3 of Zel'dovich and Raizer [106], the absorption coefficient for inverse bremsstrahlung is derived. Zel'dovich provides a simplified derivation of free-free Bremsstrahlung emission and applies the principle of detailed balance to find the absorption coefficient. This derivation is based on a calculation of the energy change experienced

by an electron in close-proximity to an ion using an approximated acceleration. This does not take into account long range “collisions” and therefore lacks a logarithmic term. The exact calculation of the acceleration vector for a hyperbolic orbit was done by Landau and Lifshitz and results in a  $\ln \Lambda$  term. Fortunately, this exact calculation differs from the simplified Zel'dovich calculation by only 2.3. Landau derives the effective radiation term in two limits,  $\frac{\hbar\omega}{k_B T} \gg \frac{\lambda_e}{R_c}$  and  $\frac{\hbar\omega}{k_B T} \ll \frac{\lambda_e}{R_c}$ . For our plasma temperature (9,250K) this results in  $\lambda = 9.2 \mu\text{m}$  which is a very long wavelength compared to the laser-plasma interaction of our experiments. Therefore, the limit of  $\frac{\hbar\omega}{k_B T} \gg \frac{\lambda_e}{R_c}$  is applied which results in an absorption coefficient given by

$$\kappa = \frac{4}{3} \left( \frac{2\pi}{3m_e k_B T} \right)^{1/2} \frac{Z^2 e^6}{h c m \nu^3} n_i n_e \left( 1 - \exp \left( -\frac{\hbar\omega}{k_B T} \right) \right) = \frac{\omega}{c} \frac{\gamma}{\omega \tau}, \quad (\text{C.3.1})$$

$$\begin{aligned} \tau &= \frac{3}{4\pi e^4 n_e} \left( \frac{3m_e k_B T}{2\pi} \right)^{1/2} \frac{\hbar\omega}{\left( 1 - \exp \left( -\frac{\hbar\omega}{k_B T} \right) \right)}, \\ \tau &= \left( \frac{\sqrt{2\pi}}{3} \omega_p \Gamma^{3/2} \right)^{-1} \left[ \frac{\hbar\omega}{k_B T \left( 1 - \exp \left( -\frac{\hbar\omega}{k_B T} \right) \right)} \right]. \end{aligned} \quad (\text{C.3.2})$$

The second equality in Eq. C.3.1 is identical to Eq. C.1.16 as this derivation was also taken in the  $\omega\tau \gg 1$  and  $\omega \gg \omega_p$  limits. Eq. C.3.2 has a new term added to the collision time which is not present in Eq. C.2.2 from Dawson. This new term accounts for stimulated emission. If  $\hbar\omega \ll k_B T$ , this term vanishes and becomes Eq. C.2.2, lower by a factor of  $\sim \frac{1}{2} \ln \Lambda$ .

## C.4 Conclusions

The preeminent works of Zel'dovich/Landau and Dawson/Oberman were derived very differently, but resulted in essentially the same expression for the absorption of inverse Bremsstrahlung radiation. Furthermore, each resulted in a slightly different factor (Dawson  $\rightarrow |1 - \gamma|^{-1/2} \ln \Lambda$ , Zel'dovich  $\rightarrow$  stimulated emission) which added to the overall picture. With this spirit in mind, below is our formulation for describing an oscillating electromagnetic field interacting with a fully ionized model.

$$k^2 = \frac{\omega^2}{c^2} \left[ (1 - \gamma\beta) + \frac{\gamma\beta}{\omega\tau_\omega} i \right], \quad (\text{C.4.1})$$

$$\omega\tau_\omega = \left[ \frac{2}{\sqrt{6\pi}} \gamma^{1/2} \Gamma^{1/2} \Gamma_\omega \ln \left( \frac{0.7}{\sqrt{3}} \Gamma_\omega^{-3/2} + 1 \right) \right]^{-1}, \quad (\text{C.4.2})$$

$$\Gamma_\omega = \Gamma \left[ \frac{k_B T}{\hbar\omega} \left( 1 - \exp \left( -\frac{\hbar\omega}{k_B T} \right) \right) \right], \quad (\text{C.4.3})$$

Here, the results of Dimonte and Daligault [22] for the logarithmic term is applied and a frequency-dependent plasma parameter  $\Gamma_\omega$  is included.  $\Gamma_\omega$  was chosen such that it behaves continuously as a function and in its first derivative. It was also formulated to obey both limiting cases. In the high frequency limit ( $\frac{\hbar\omega}{k_B T} \gg 1$ ),  $\Gamma_\omega \approx \left(\frac{e^2}{\hbar\omega}\right) \left(\frac{4\pi n}{3}\right)^{1/3}$  and is independent of temperature and only weakly dependent on the density. This is true for high frequency photons as their energies are high enough that the *average* plasma parameter is unaffected. In the low frequency limit ( $\frac{\hbar\omega}{k_B T} \ll 1$ ),  $\Gamma_\omega \approx \Gamma$  and reduces to the well-known  $\tau_{e-i}$ , which corresponds to electron-ion collisions in the absence of an electromagnetic field.

Below are two interesting limiting cases for a strongly-coupled plasma ( $\Gamma \geq 1$ ) when  $\omega\tau \gg 1$  and  $\hbar\omega \ll k_B T$ .

$$\begin{cases} \omega\tau_\omega \simeq 5.37\gamma^{-1/2} \text{ and } \kappa \simeq 1.17\frac{\gamma}{\lambda} & \text{for } \omega_p \gg \omega (\gamma \gg 1) \\ \omega\tau_\omega \simeq 5.37\gamma^{-1/2} \text{ and } \kappa \simeq 1.17\frac{\gamma^{3/2}}{\lambda} & \text{for } \omega_p \ll \omega (\gamma \ll 1) \end{cases}$$

This result shows the collision frequency is always smaller and scales only with the plasma frequency in the dense plasma regime. With the formulation above, only  $\omega$ ,  $T_{\text{plasma}}$ , and  $n_e$  are needed to describe this model for a very large parameter space.

Finally, this result for  $\tau$  can be shown to reproduce the electron-ion collision time which also governs the transfer of energy between electrons with ions and is a crucial finding in the “Laser Breakdown of High-Pressure Noble Gases” experiments. All that is needed to show this equivalence is to let  $\hbar\omega \rightarrow 0$  resulting in

$$\tau \simeq \left( \frac{2}{\sqrt{6\pi}} \omega_p \Gamma^{3/2} \ln \Lambda \right)^{-1} \approx 2.17 \times (\omega_p \Gamma^{3/2} \ln \Lambda)^{-1}$$

where the expression inside the log has been set to  $\Lambda$  for simplified notation. Comparisons to formulations by Spitzer, Swanson, and Zel'dovich are given below.

$$\tau_{Spitzer} \approx 2.35 \times (\omega_p \Gamma^{3/2} \ln \Lambda)^{-1}$$

$$\tau_{Swanson} \approx 2.35 \times (\omega_p \Gamma^{3/2} \ln \Lambda)^{-1}$$

$$\tau_{Zel'dovich} \approx 1.32 \times (\omega_p \Gamma^{3/2} \ln \Lambda)^{-1}$$

## Appendix D

### Supplemental Material - Sulfuric Acid Sonoluminescence

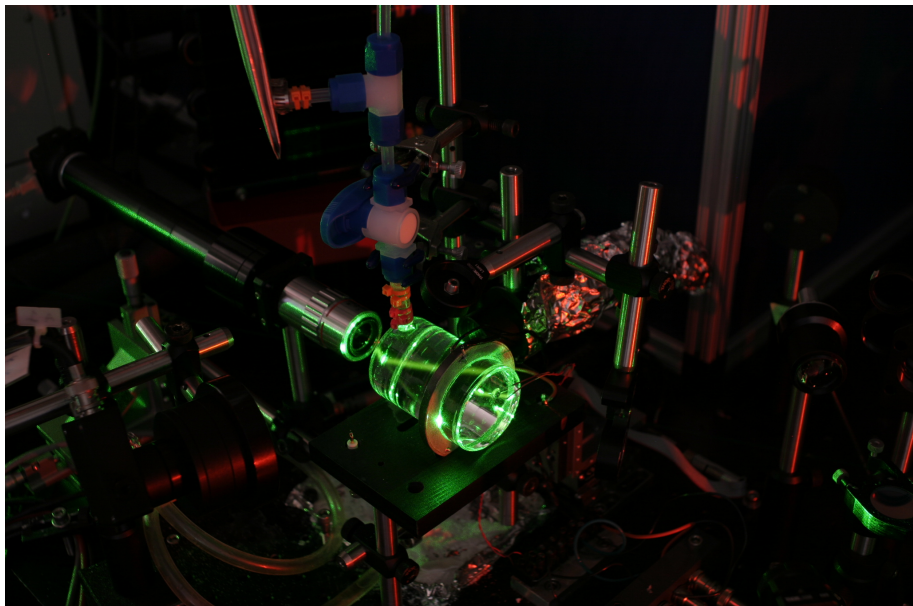


Figure D.1: Photograph of the experimental setup showing the SL resonator (center), Mie collecting optic (bottom left), microscope objective for bubble calibration (left of resonator), and the laser-bubble beam path (green illumination).

The experimental arrangement for the sulfuric acid sonoluminescence experiment is shown in Fig. D.1. A pair of lenses were used to collect 47 degrees of solid angle centered

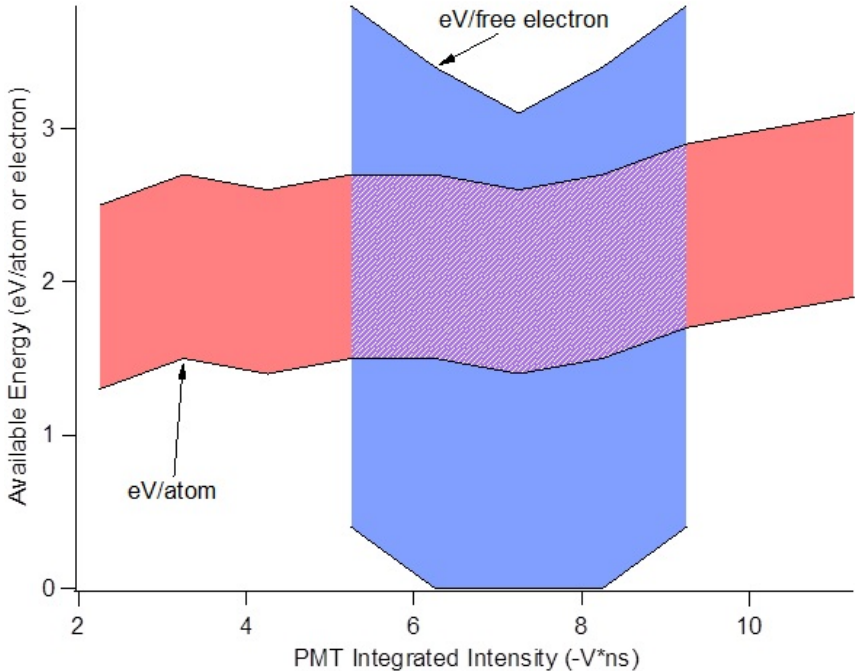


Figure D.2: Available energy as a function of PMT integrated intensity. The red area represents the measured energy per xenon atom available to create the sonoluminescing plasma. The blue area represents the energy available for ionization per free electron for opaque regions after heating. This represents an upper bound on the ionization potential to ionize a free electron. The minimum number of free electrons and therefore the energy needed to create them could only be determined in cases where  $R_e \simeq R_c$ .

at 48 degrees relative to the exit of the beam. The beam entered the cylindrically-shaped acoustic cell through a flat side in order to preserve the Gaussian shape of the beam as much as possible. The laser was triggered at  $\sim 150$  Hz to fire at a given phase of the bubble motion and the intensity of the Mie scattering signal as well as the intensity and timing of the SL was recorded. The large size of the laser beam (3.8 mm 1/e diameter) and the extreme brightness (TW) allowed us to overcome the spatial jitter (several mm) and intensity (10s of W) of the SL. At any point in phase the Mie scattering data contains a variety of intensities corresponding to the changing collection angles into the diode from bubble movement. This distribution is roughly Gaussian and corresponds to the bubble's distribution of positions within its sphere of movement. As the bubble cannot move more than a few microns within any given collapse, position distribution is not a function

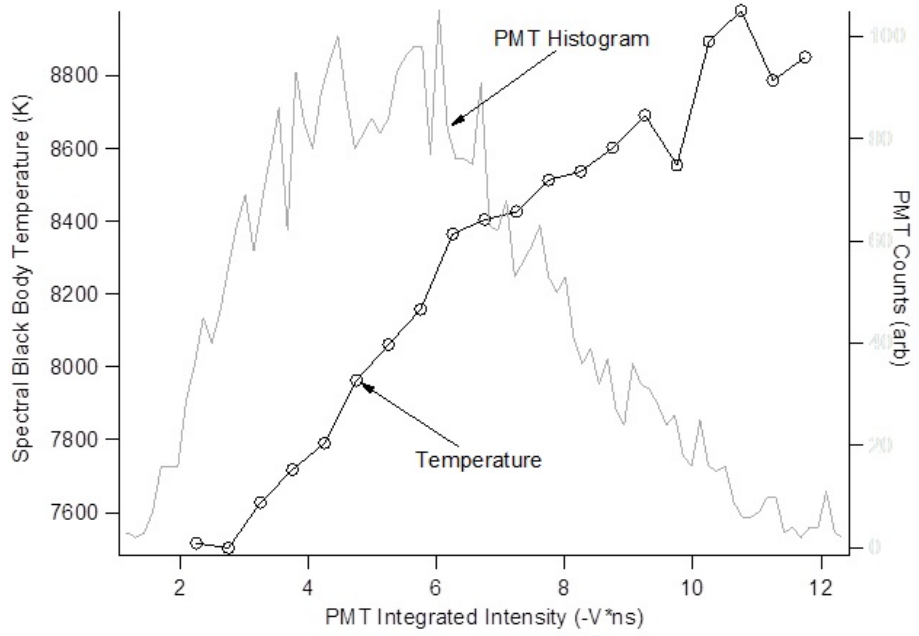


Figure D.3: PMT histogram with associated spectrum Planck black body temperature fits. The spectrum data is discriminated by 0.5 V ns ranges of PMT integrated intensity.

of phase and therefore we can directly compare different points in phase through their average. In order to resolve the minimum radius, a proportionally large number of events were captured at this point in phase.

# Appendix E

## Supplemental Material - Sonoluminescence-Laser Interaction

### E.1 Experimental Setup

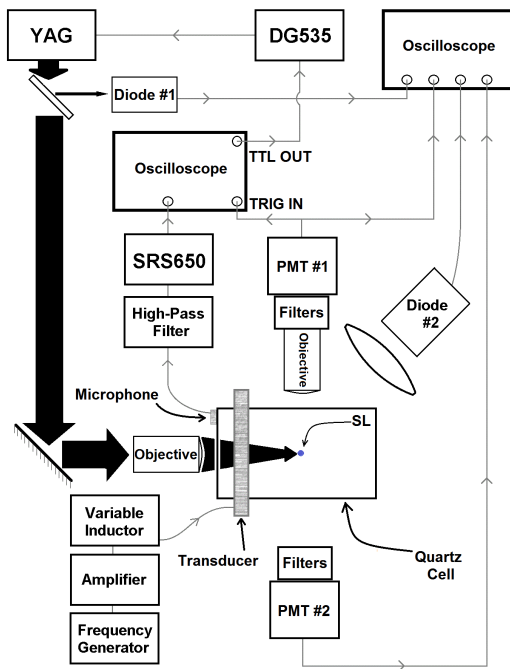


Figure E.1: Block diagram of the experimental setup showing laser, timing, SL, and data acquisition components.

The experimental arrangement for the SL-laser interaction experiment is shown in Fig. E.1. The quartz cell is driven on resonance by a piezoelectric ring transducer. The transducer is powered by an electrically resonant circuit. A frequency generator seeds the resonant frequency into an acoustic amplifier which is then fed into series with a variable inductor. This is done to match the electrical to acoustic resonance and obtain large acoustic amplification at minimum electric output.

A piezoelectric microphone is epoxied onto the SL resonator and serves two purposes for this experiment. The first is to help locate the frequency at which bubbles are trapped and emit SL. The second is to ensure the same bubble dynamics and collapse location over the course of an experimental run. Over the course of experimenting, the author of this thesis found that the high-frequency components (from shock waves) within the microphone's carrier signal was correlated with the intensity and collapse location of SL. In other words, each SL amplitude and location within the resonator has its own unique high-frequency signature. By recording this signature, a unique SL can be recalled on a day-to-day basis. The microphone signal is sent through a high-pass filter and preamplifier, and the signature is recorded onto an oscilloscope. There are three parameters which can be adjusted to recall the desired signature: the driving frequency, the driving amplitude, and the temperature of the SL cell with a cooling fan (within 0.5 C). The author of this thesis used the latter for simplicity and reproducibility. Over the course of an experiment, the temperature was adjusted and the position of the SL bubble remained fixed, as verified with laser scattering.

The timing signals of this experiment went as follows:

1. SL emission is collected by an infinity corrected microscope objective and fed into PMT#1 (Hamamatsu H5783-03).
2. The signal from PMT#1 is split into two oscilloscopes. The first oscilloscope (middle Fig. E.1) is used as a trigger for the microphone signals. The second oscilloscope digitizes the PMT signal for analysis.
3. The first oscilloscope outputs a trigger to a delay generator (SRS DG535).
4. The delay generator is limited to 10 Hz and outputs an accurately delayed trigger

to the YAG laser. The YAG requires  $\sim 254 \mu\text{s}$  from trigger input to light output, which corresponds to the 8<sup>th</sup> SL collapse after the initial trigger.

For each laser pulse, the oscilloscope records the signals from two PMTs (measuring the SL-laser interaction), a diode measuring the laser intensity, and a diode measuring the Mie scattered light. Two PMTs are used to increase the overall dynamic range of the SL-laser interaction measurement. PMT#1 is kept in a fixed position while the distance of PMT#2 to the bubble is adjusted. Both PMTs are calibrated against each other in time and intensity for every PMT#2 location.

## E.2 Continuous Mie Scattering

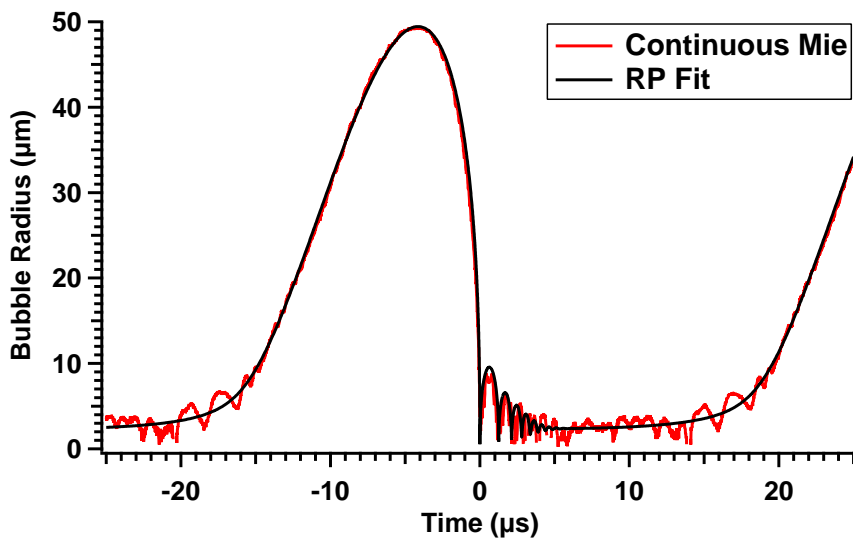


Figure E.2: Continuous Mie scattering of water SL (1% Xe in 150 Torr N<sub>2</sub>) and the best RP fit. The RP fit values are  $p_a = 1.40$  bar and  $R_0 = 3.20 \mu\text{m}$ , which results in  $R_{max} = 49.4 \mu\text{m}$  and  $R_c = 0.547 \mu\text{m}$ .

The bubble dynamics were measured with continuous Mie scattering and fit to the Rayleigh-Plesset (RP) equation. The ambient bubble radius  $R_0 = 3.20 \mu\text{m}$  and the minimum collapse radius  $R_c = 0.547 \mu\text{m}$  results in a final collapse density  $n_c = 4.93 \times 10^{21} \text{ atoms/cm}^{-3}$ .

### E.3 Spectrum

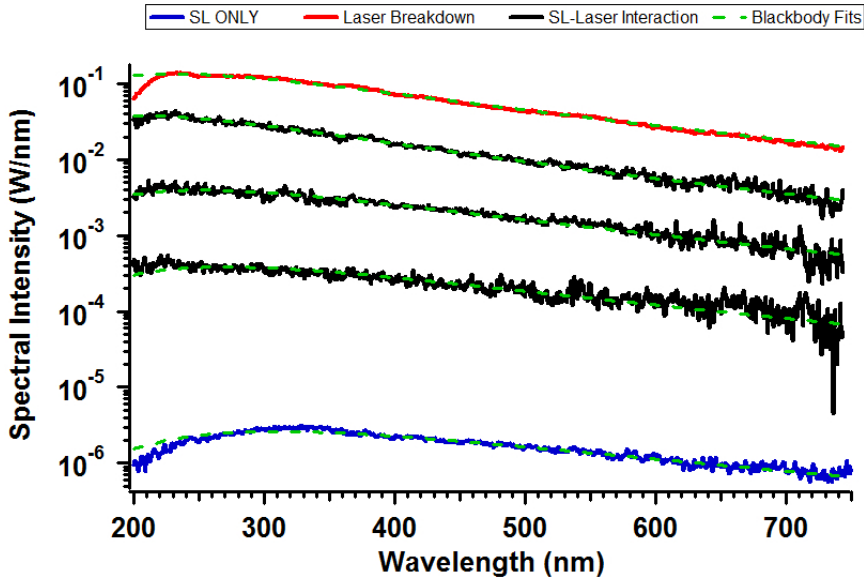


Figure E.3: Calibrated spectrum of SL with (blue curve) and without (black curves) 1064 nm laser interaction. Spectrum of laser breakdown in water without an acoustic field (no SL) was measured (red curve). All spectra are well fit to blackbody emission (green dashed curves).

Calibrated spectrum in Fig. E.3 was measured for SL-laser interactions. In addition, the spectrum was measured for SL without a laser field (SL Only) and laser-water breakdown without an acoustic field (no SL). In all cases, the spectrum is well fit to blackbody emission. For SL only, the blackbody temperature  $T = 9250$  K and radius of emission  $R_e = 0.47 \mu\text{m}$ .  $R_e$  is consistent with  $R_c$  from the RP fit and suggests a bubble-filling blackbody. SL-laser interaction spectra are shown for various interaction strengths. Increasing interaction strengths results in an increase in both  $T$  and  $R_e$ . In Fig. E.3,  $T = 10590, 11420$ , and  $13950$  K and  $R_e = 4.08, 10.9$ , and  $20.4 \mu\text{m}$  for SL-laser interactions. Even larger  $R_e$  is found for laser-water breakdown ( $T = 12390$  K and  $R_e = 51.7 \mu\text{m}$ ). Increased  $R_e$  for SL-laser plasma is consistent with laser-water breakdown initiated by SL plasma.

## Appendix F

### Supplemental Material - Laser Breakdown in High-Pressure Gases

#### F.1 Experimental Setup

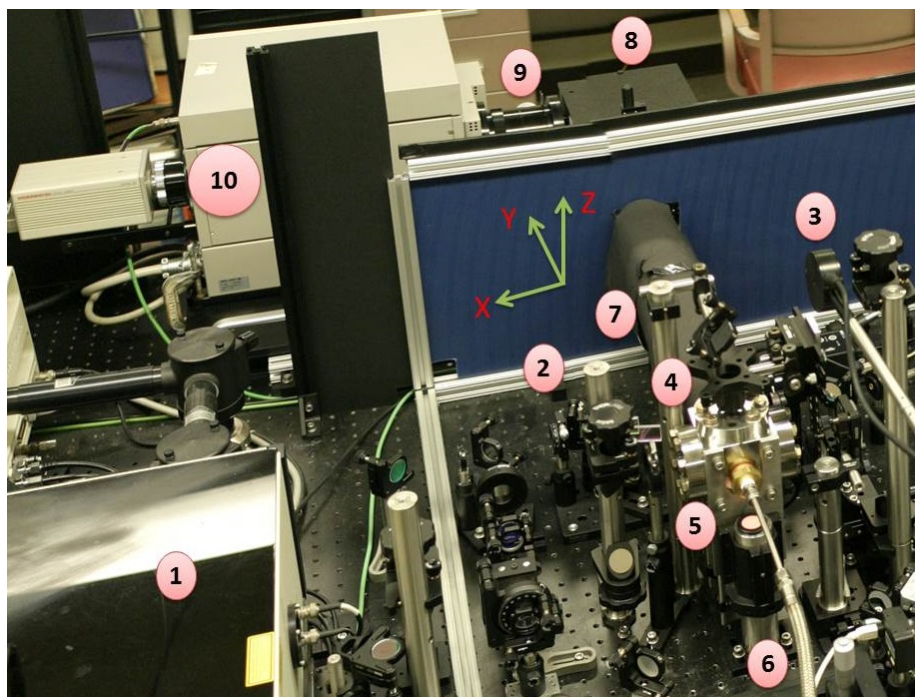


Figure F.1: Photograph of the laser breakdown experimental setup.

The experimental arrangement for the laser breakdown experiment is shown in Fig. F.1. Laser pulses are produced from an amplified Ti:Sapphire laser system and output at the amplifier (1). A 1 kHz pulse train of 120 fs laser pulses is aligned through a polarized variable attenuator (2).

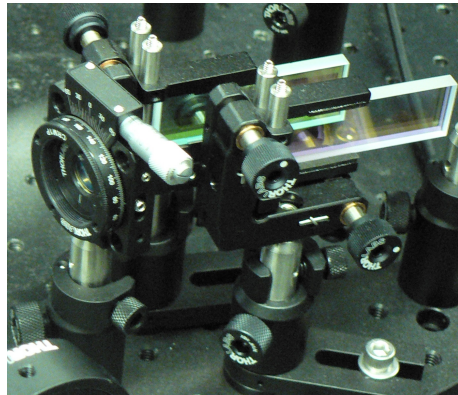


Figure F.2: Photograph of the polarizing variable attenuator.

The attenuator varies the incoming pulse energy continuously from 0 – 1 mJ/pulse. In Fig. F.2, the attenuator first rotates the laser polarization with a  $1/2$ -wave plate (left). The laser is reflected from the surfaces of two dielectric polarizers, whose reflection coefficient is polarization specific. In this way, the laser energy can be varied smoothly and without significantly increasing the pulse width. The laser energy can be measured just before and after each experimental run with a power meter that is inserted in the beam path (3). The laser is first aligned straight through the center of the pressure chamber using two mirrors and IR targets. Once aligned, a 6 cm lens (4) is inserted in the beam path and focuses the laser pulses into the center of the pressure chamber (5). The lens is mounted on a translation stage and moves the focal position relative to the chamber in the “Z” axis (laser propagation direction). Small changes in the focal position in the other two directions (“X” and “Y”) are controlled with the final steering mirror. Gas is inserted into the chamber with high-pressure flexible tubing (6).

The plasma emission is collected and imaged by a UV triplet lens (7, covered with blackout) onto the entrance slits of a 150 mm spectrometer (8) in the “X-Z” plane. The slits are oriented along the length of the plasma (“Z” axis) and close in the plasma’s

radial direction (“X” axis). The image from the spectrometer output is focused onto the entrance slits of a 1:1 UV-NIR relay achromat (9) that are oriented in the “X” axis. This image is relayed onto the photocathode of the streak camera (10). In this setup, the plasma radius/spectrum is measured as a function of time. The streak imaging system can be seen in Fig. F.3 (left)

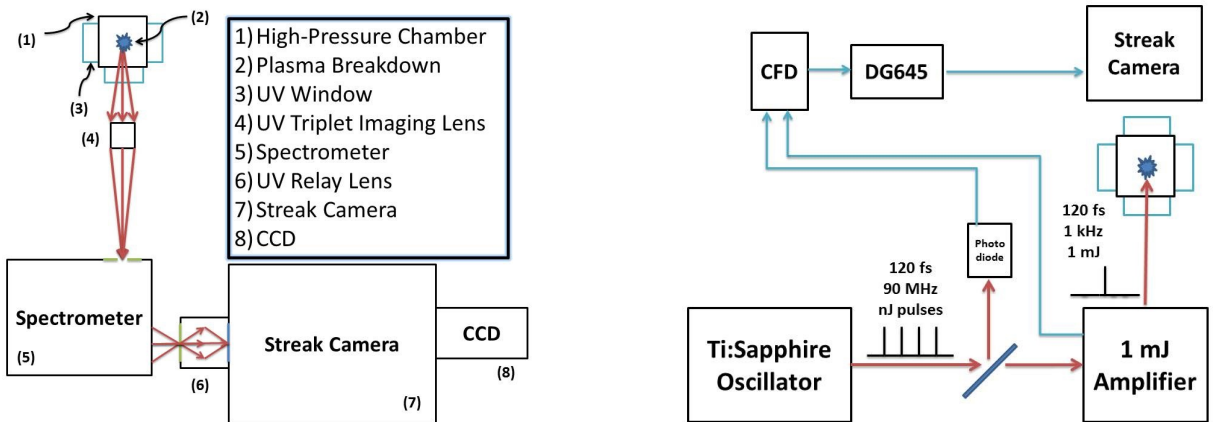


Figure F.3: Block diagram of the experimental setup showing the spectral diagnostic (left) and the laser timing components (right).

Streaking the plasma emission requires precise and repeatable timing. Although the amplification stage provides an electrical timing signal preceding the laser output with sufficient time, the temporal jitter is  $\gtrsim 100$  ps and limits the overall streak resolution. A system-limited resolution (20 ps in multishot mode) was achieved through an optical trigger generated from the output train of the Ti:Sapphire oscillator. The timing scheme is shown in Fig. F.3 (right). Before entering the laser amplifier, a small amount of laser energy from the Ti:Sapphire oscillator is reflected off a glass slide and measured by a fast photodiode. This signal is sent to a constant-fraction discriminator (CFD) and creates a 90 MHz electric trigger. However, a veto signal stops these 90 MHz triggers until the laser amplifier signal (1 kHz) is received. The 1 kHz  $< 20$  ps jitter output from the CFD is sent to a delay generator (DG645). This signal is then delayed to match the plasma emission to the streak camera.

## F.2 Opacity

Spectral opacity has been established after a critical pressure for xenon, argon, and helium. Complimenting the opacity arguments in Chapter 7 are the following observations.

### F.2.1 Spectral Saturation

Continuous emission from high density plasma originates mostly from bremsstrahlung emission (see Chapter 4), whose intensity is proportional to  $n_e^2$ . If the laser breakdown plasmas were transparent emitters at a higher temperature than the blackbody fit, then adding more gas will continue to increase the continuous spectrum through bremsstrahlung. However, this is not observed as seen in Fig. F.4, which graphs the spectrum of xenon, argon, and helium breakdown as a function of pressure for a fixed laser energy. As the static pressure is increased, the overall spectral intensity increases. Once the critical pressure is reached where blackbody behavior is observed, the spectrum “saturates” in intensity with increasing pressure. This indicates that the blackbody plasma produced by laser breakdown maintains similar temperatures for a wide range of initial pressures. This is not too surprising as the laser energy is fixed and the breakdown mechanism is mostly independent of atomic atomic density (multiphoton ionization).

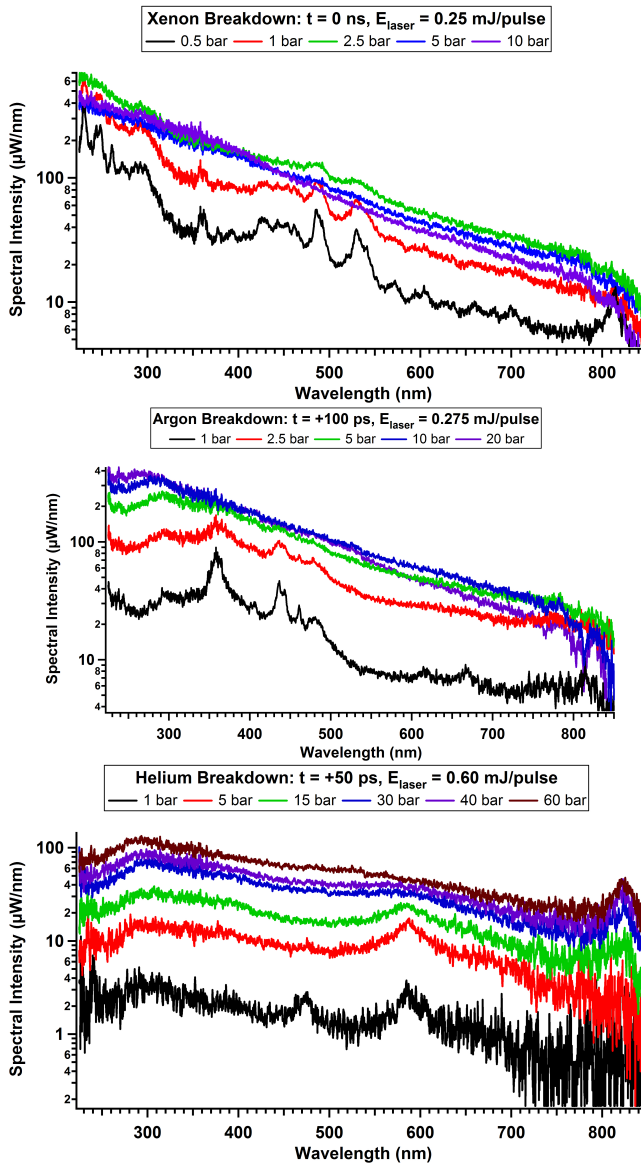


Figure F.4: Early spectrum for xenon/argon/helium (top/middle/bottom) vs. static gas pressure. Spectral intensity saturates at a gas-dependent density for all gases.

### F.2.2 Absorption Lines

A key sign of a highly opaque plasma is the observation of absorption lines. A famous example is the sun's absorption lines known as Fraunhofer lines. These lines are frequently observed in astronomical bodies and are used to determine elemental compositions. Absorption lines from the laser breakdown produced in this experiment originate from a

temperature gradient within the plasma. In this description, photons are emitted from hotter regions within the plasma. These photons are absorbed as they propagate outward by plasma of decreasing temperature. A point is reached where most photons will escape the plasma and produce a blackbody spectrum. However, photons near opaque atomic lines are strongly absorbed and re-emitted at a lower temperature, and therefore lower intensity. This results in a dip near atomic lines and is seen for xenon and argon in Fig. F.5.

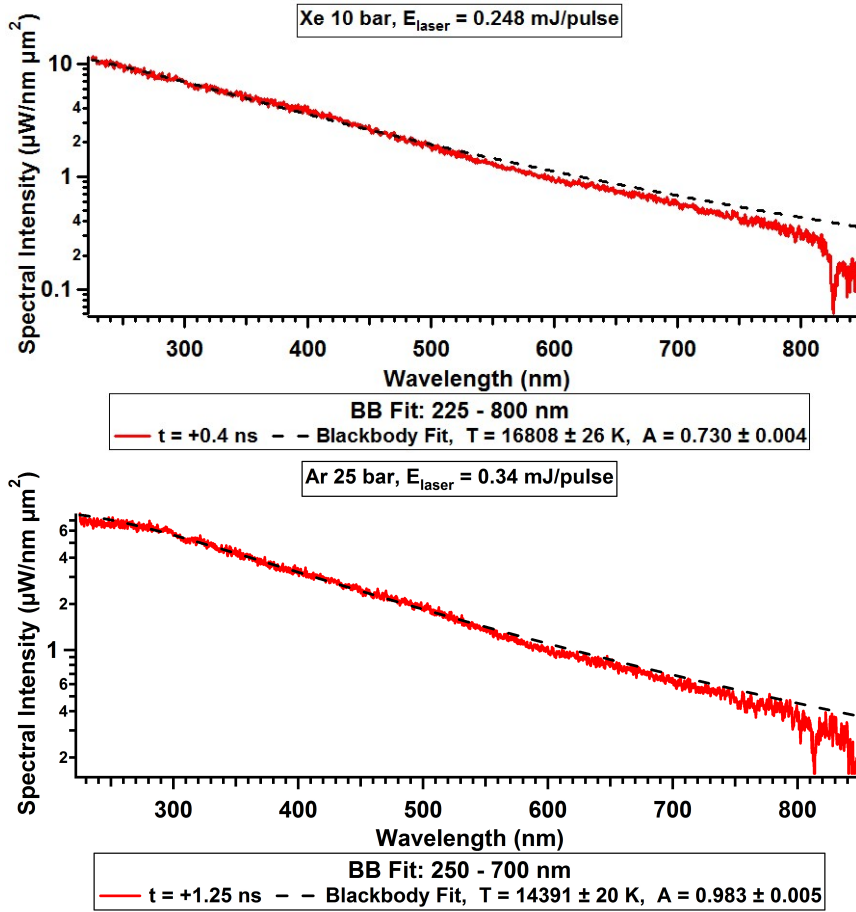


Figure F.5: Spectrum of 10 bar xenon (top) and 25 bar argon (bottom) breakdown. Absorption lines appear during early times for 823 nm Xe and 811.5 nm Ar lines

### F.3 Greybody

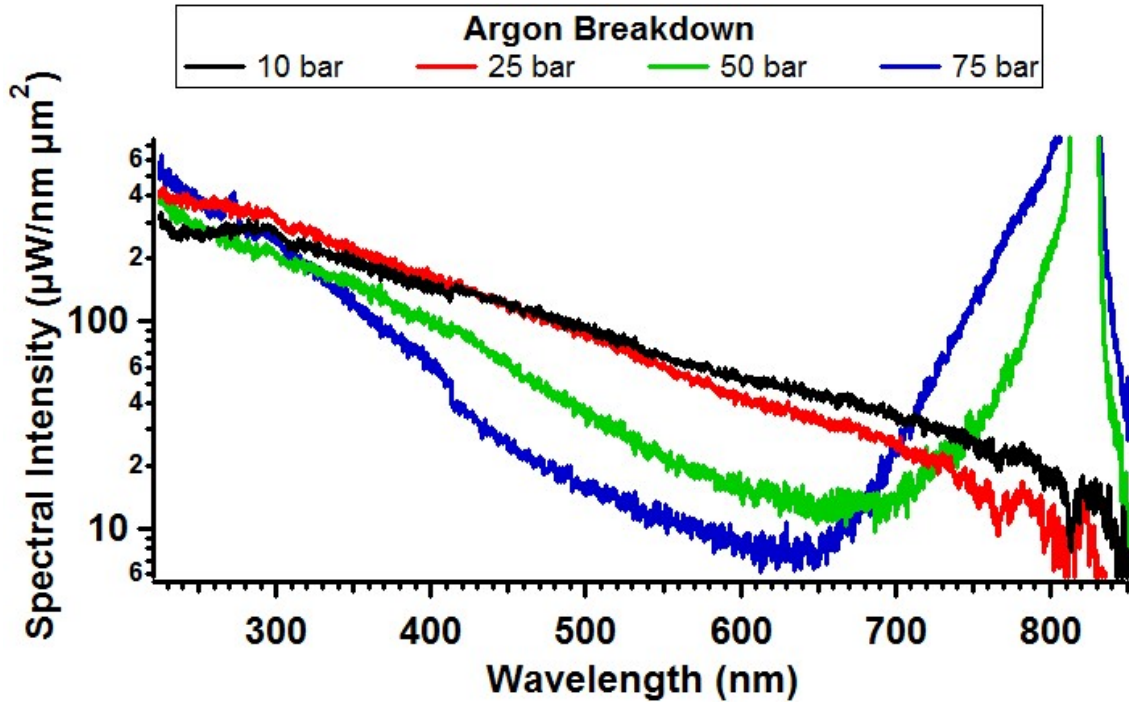


Figure F.6: Spectrum of argon laser breakdown as a function of pressure at early times. Spectrum is taken at  $t = +100$  ps for 10 and 25 bar and  $t = +10$  ps for 50 and 75 bar. Laser scattering ( $\sim 650 - 850$  nm) grows as a function of pressure and is shown at  $t \sim 0$  ps (green and blue curves).

A curious thing occurs to the breakdown spectrum beyond the critical pressure. As pressure increases, the plasma spectrum starts to *diverge* from blackbody behavior. In Fig. F.6, the spectral intensity of argon breakdown begins to *decrease* for red wavelengths. This is completely opposite the absorption coefficient of bremsstrahlung with increasing density. This effect continues deeper into the blue wavelengths with increasing pressure, reaching  $< 400$  nm at 75 bar.

To describe this observation, we look to the work of Skowronek et. al [81] and the concept of a greybody. In this work, temporally and spatially-resolved calibrated spectrum was measured for high electron density plasmas generated from powerful electric discharges. The plasma was found to be highly opaque in the visible spectrum and not in the infrared. They proposed that the drop in infrared was due to plasma frequency

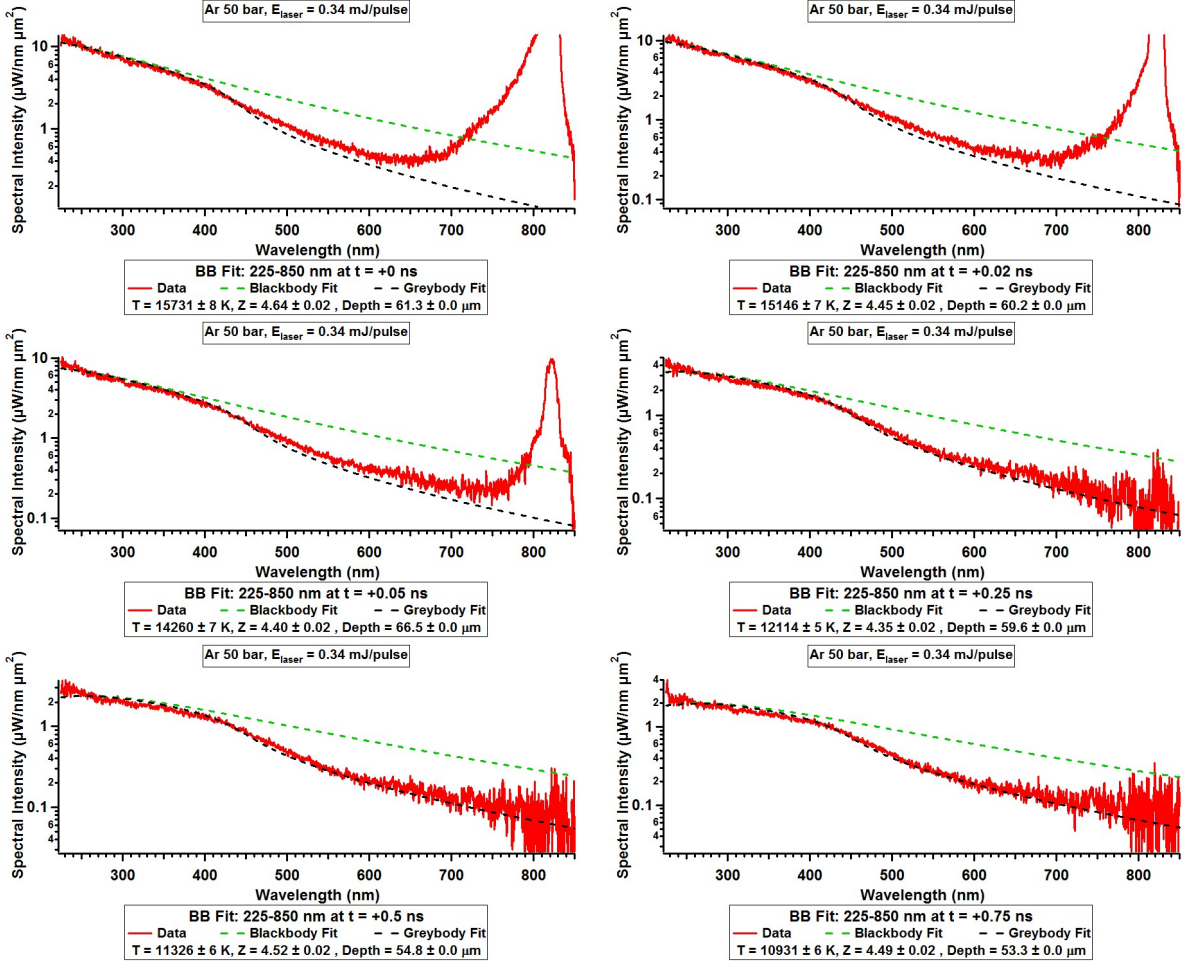


Figure F.7: Spectrum of 50 bar argon breakdown for various times with blackbody (green dashed) and greybody (black dashed) fits.

reflections ( $\omega_p$ -reflection). This effect is also seen in Chapter 6 for SL in water, as a laser of 1064 nm is reflected from a high density plasma. This effect, as well as a drop in intensity due to  $\kappa l_{BB} < 1$  can be described as a greybody model, whose spectral emissivity is a function of wavelength.

The formulation of a greybody is defined by a wavelength-dependent emissivity [81]

$$\epsilon = \frac{I}{I_0} = (1 - R) \frac{1 - \exp(-\kappa l_{BB})}{1 - R \exp(-\kappa l_{BB})}, \quad (\text{F.3.1})$$

where  $R$  is the reflection coefficient (Eq. 4.1.4),  $\kappa$  is the absorption coefficient (Eq. 4.1.3),  $l_{BB}$  is the plasma depth, and  $I$  ( $I_0$ ) is the intensity of the greybody(blackbody) at tempera-

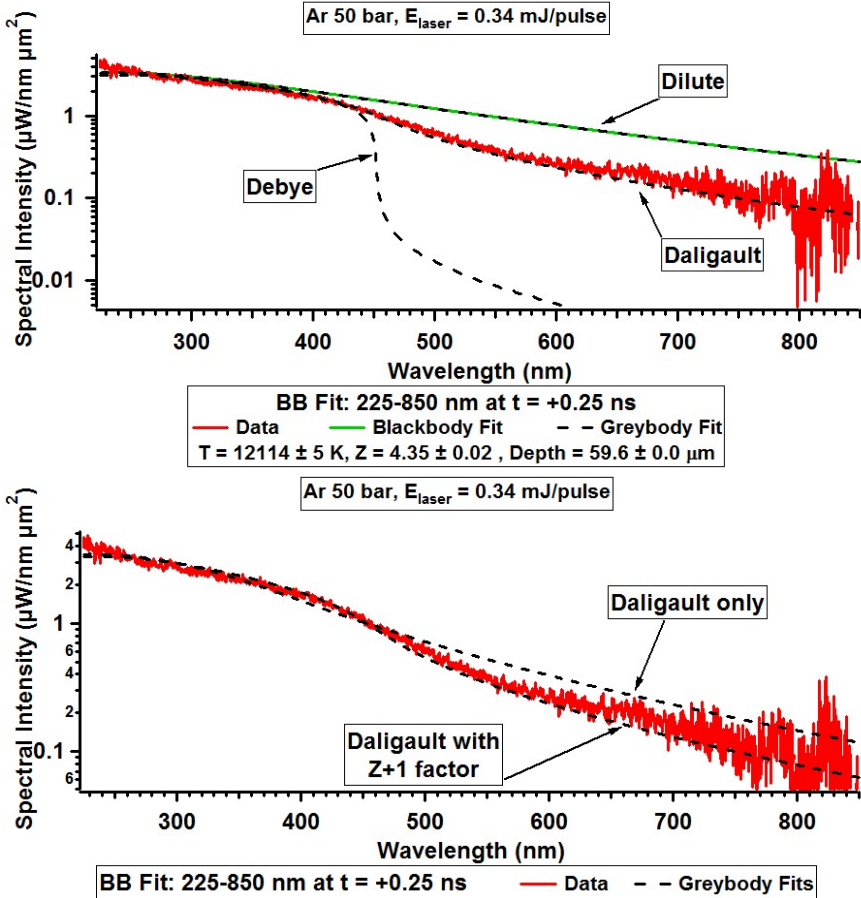


Figure F.8: Spectrum of 50 bar argon breakdown with various greybody screening models (top). Spectrum of 50 bar argon breakdown with and without  $(\bar{Z} + 1)^{-1/2}$  in Coulomb logarithm (bottom).

ture  $T$  (Eq. 7.1). Greybody fits for 50 bar argon breakdown are shown as a function of time in Fig. F.7, where  $l_{BB}$  is set to the plasma waist using the streak images. The spectrum is well fit to a greybody using only two adjustable parameters ( $T$  and  $\bar{Z}$ )! Only the “Daligault” screening model produces reasonable spectral fits as shown in Fig. F.8(top). The “Dilute” model of screening is almost identical to a blackbody, as  $\omega_p$ -reflection is shorted-out by the high level of dampening ( $\omega\tau_\omega \lesssim 1$ ). For the extreme “Debye” screening model,  $\omega_p$ -reflection is near 100% for frequencies below  $\omega_p$  due to  $\omega\tau_\omega \gg 1$ . Furthermore, this analysis has the ability to fine-tune the exact expression for the Coulomb logarithm. For example, the greybody fits from Figs. F.7 and F.8(bottom) include the factor  $(\bar{Z} + 1)^{-1/2}$

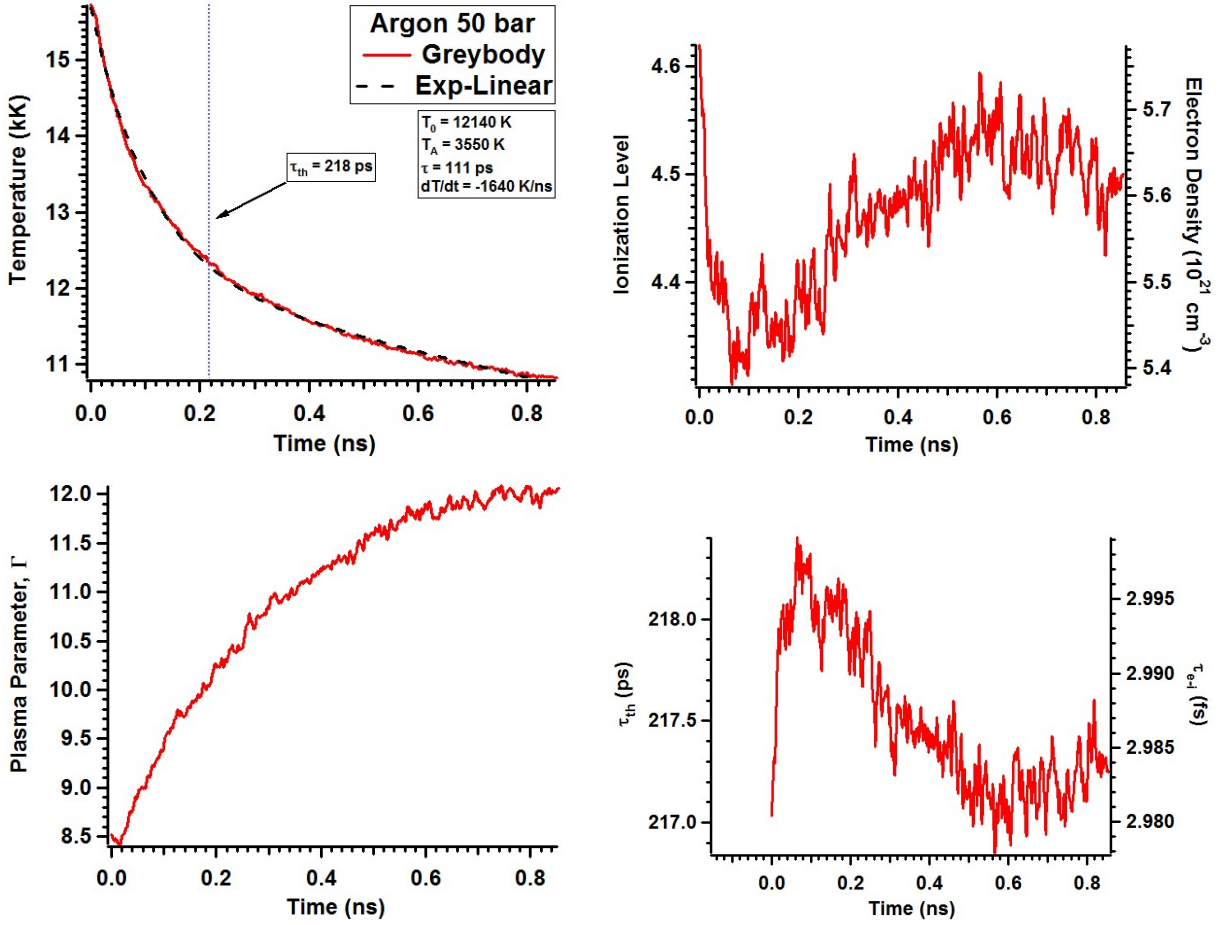


Figure F.9: Temperature, electron density, plasma parameter, and electron-ion collision time for 50 bar argon breakdown using greybody fits.

within the Coulomb logarithm ( $\Lambda = \Gamma^{-3/2} (3(\bar{Z} + 1))^{-1/2}$ ), which is not included in [22].

Unlike the bounds placed in the blackbody analysis of Chapter 7, greybody fits produce exact values for the electron density. From the greybody fits, we now know the  $T$ ,  $n_e$ ,  $n_0$ , and  $\tau_{e-i}(\ln \Lambda)$  for a strongly-coupled plasma, whose properties are measured as a function of time in Fig. F.9. Like the analysis of Chapter 7, the calculated thermalization time from the greybody fits are self-consistent with the exponential drop in temperature (Fig. F.9, top-left).

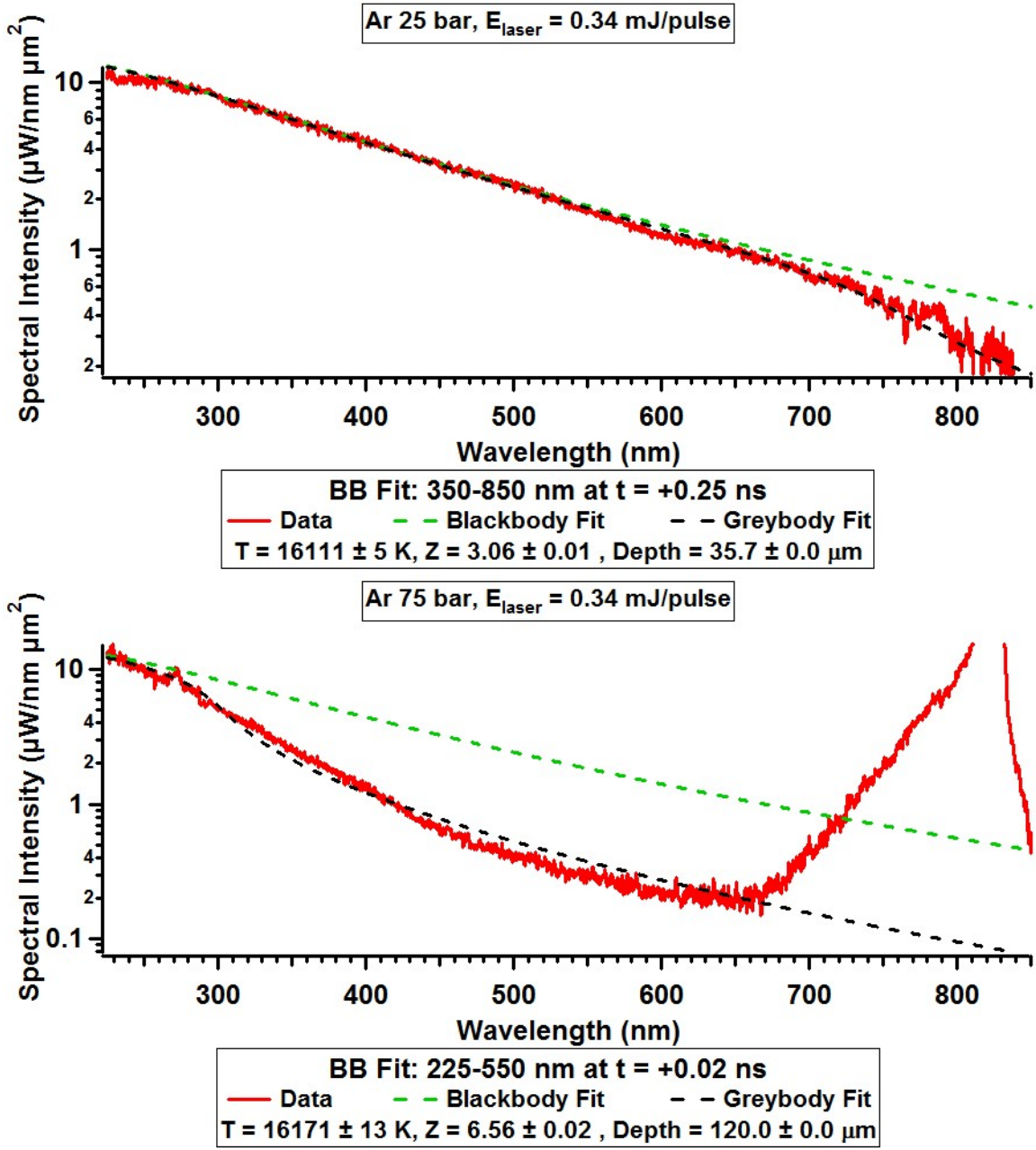


Figure F.10: Spectrum of 25 and 75 bar argon breakdown with greybody fits.

Finally, greybody analysis is extended to 25 and 75 bar argon breakdown in Fig. F.10. These pressures show excellent agreement with the greybody formula used for 50 bar argon and indicate an ever-growing ionization level with increasing atomic density. This is consistent with the phase transition theory explored in this thesis. Greybody values for

Pressure (bar)	t (ps)	T (K)	$\bar{Z}$	$n_e$ (cm $^{-3}$ )	$\Gamma$	$\tau_{e-i}$ (fs)	$\tau_{th}$ (ps)	$T_F$ (K)
25	+250	16,110	3.06	$1.9 \times 10^{21}$	4.4	4.4	320	6,500
50	+20	15,150	4.45	$5.6 \times 10^{21}$	8.5	3.0	220	13,300
75	+20	16,170	6.56	$1.2 \times 10^{22}$	13.5	2.4	170	22,000

Table F.1: Plasma parameters for argon breakdown using greybody values.

argon breakdown are shown in Table F.1. These results indicate a new regime of physics is being opened to experiment. Quantum statistics are needed for such high electron densities as the Fermi temperature  $T_F$  becomes larger than the plasma temperature.

# Appendix G

## Supplemental Material - Spark Discharge in High-Pressure Gases

### G.1 Experimental Setup

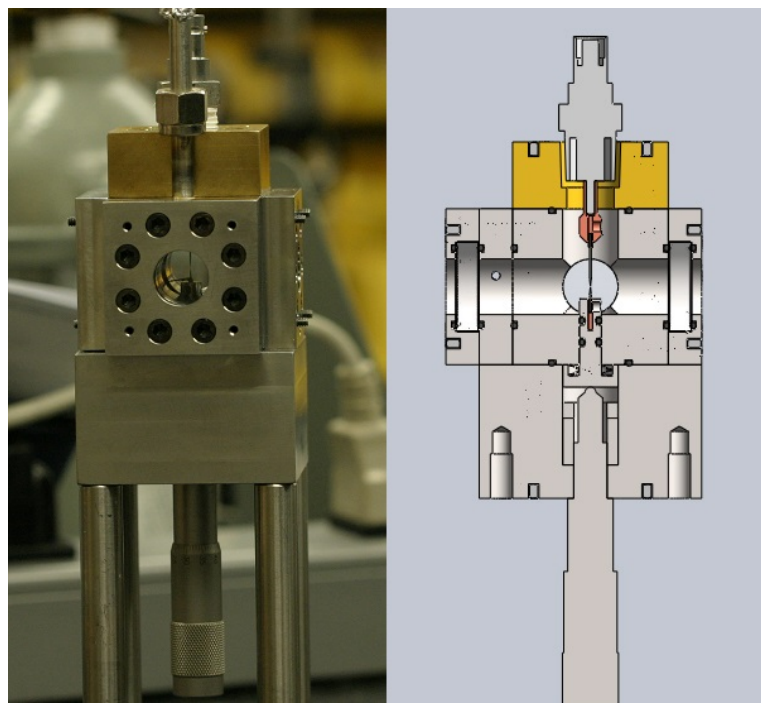


Figure G.1: Photograph of the pressure chamber for the spark discharge experiment (left) and a CAD cross section (right).

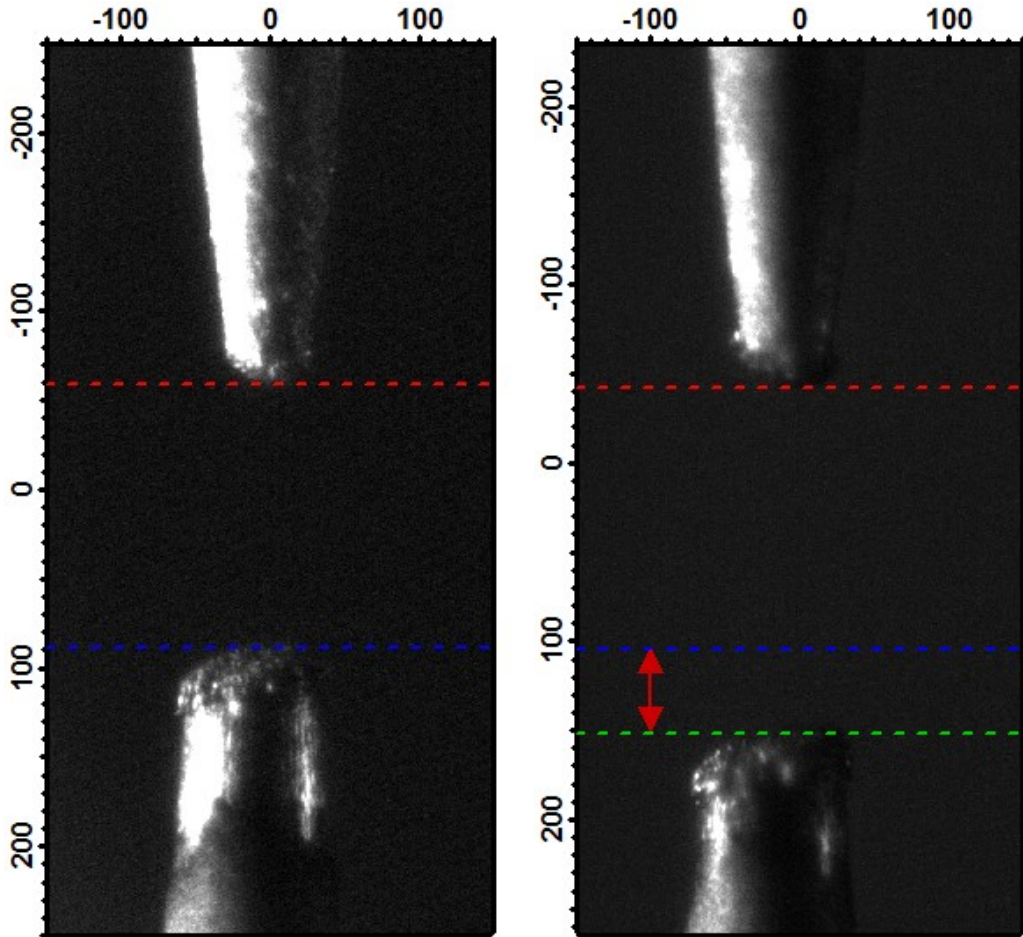


Figure G.2: Microscope image of tungsten needles before (left) and after (right)  $\sim 32,000$  discharges in 10 bar xenon. Spatial scales are in microns.  $\sim 45 \mu\text{m}$  of tungsten is ablated from the high-voltage electrode.

The high pressure chamber used in the spark discharge experiment is shown in Fig. G.1. The chamber body is constructed from a  $1.5'' \times 1.5'' \times 1.5''$  stainless steel body with 1" bore holes from four sides. Sharpened tungsten electrodes are located at the center of the chamber. Light emission from the spark discharge is observed through UV quartz windows on four sides of the chamber. High voltage (HV) is connected to the top electrode through a high pressure NPT/SHV feedthrough. The bottom electrode is grounded to the chamber (connected to SHV ground) through a grounding strip inside the chamber. Pressure seals were made with o-rings and tested to 100 bar.

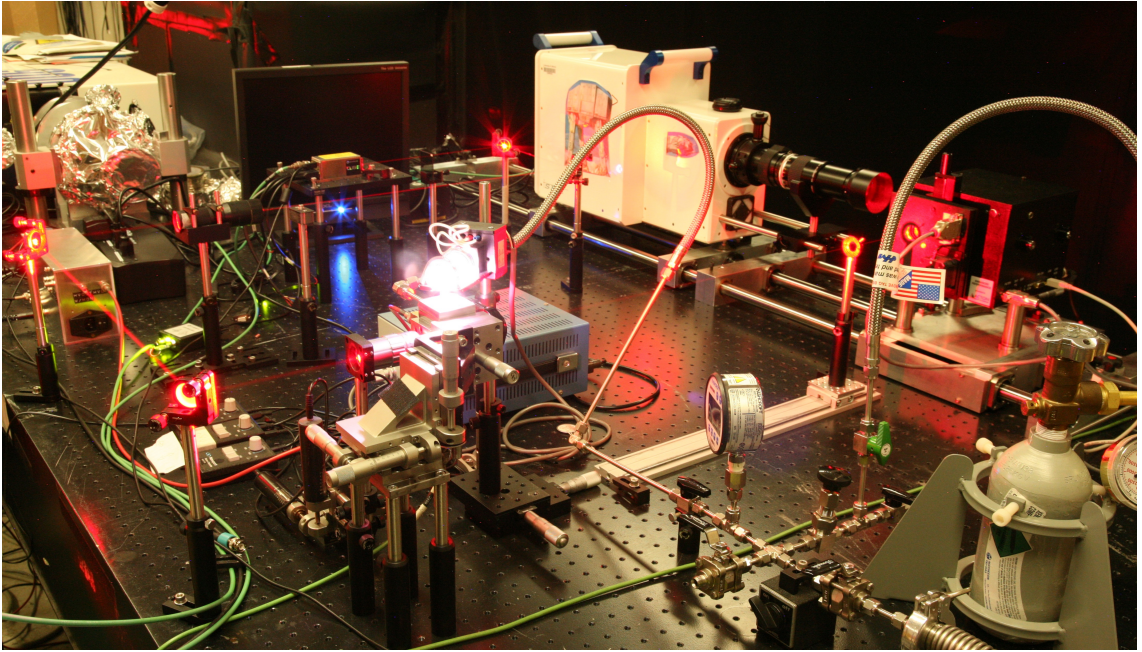


Figure G.3: Experimental photograph of the spark discharge with CW laser absorption.

During operation, tungsten is ablated from the HV electrode after each spark, which suggests electron bombardment as the primary source of damage. This is quantified in Fig. G.2 which shows the needles before and after  $\sim 32,000$  sparks (10 bar xenon operated at 5 kV).  $\sim 45 \mu\text{m}$  of tungsten is removed resulting in  $\sim 1.4 \text{ nm}$  of tungsten/spark. To keep the gap distance fixed between each experimental run, the needles were moved closer to each other by a custom actuator (see bottom of Fig. G.1).

A photograph of the spark discharge with CW laser absorption experiment is shown in Fig. E.1. In this experiment, spark discharges are generated in the pressure chamber, located in the center of Fig. E.1. Sparks were facilitated by the production of photoelectrons using a UV light source (D2 lamp) and improved overall timing. The spark plasma was imaged by a UV-NIR triplet lens (Edmund Optics) onto the entrance slits of a 150 mm Acton spectrometer (right). Within the spectrometer, the image was either reflected or spread in wavelength. The spectrometer output was relayed 1:1 by a Nikon 105 mm F4.5 UV Lens into a framing camera (Specialised-Imaging, Custom SIMD-052). The framing camera consists of 4 $\times$  ICCDs capable of gating at 3 ns for a single event. Each ICCD

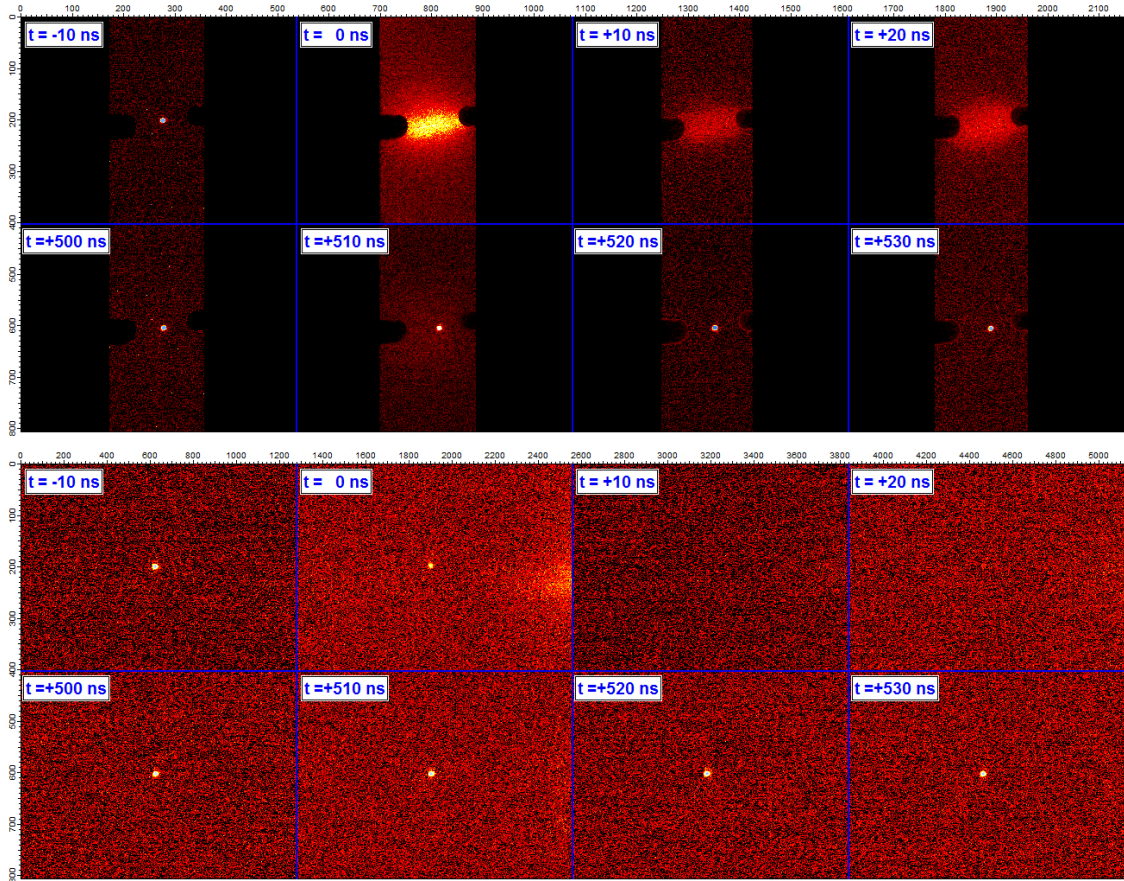


Figure G.4: Framing images of CW laser blocking with 20 bar xenon discharge using the spectrometer in reflection mode (top) and spectrum mode (bottom).

acquires 2 images separated by user-supplied delay, although limited to  $\sim 500$  ns between the first and last 4 images. This framing camera was customized for spectral sensitivity down to 200 nm, allowing full spectroscopic measurements. Both the framing camera and spectrometer were aligned on a custom rail system for micron precision.

A 100 mW CW triggerable laser (Coherent CUBE-640 nm) was focused through the center region of the spark discharge using a 40 mm microscope objective. To achieve smallest focus, the laser beam waist was expanded by 3 $\times$  before focusing. Accurate temporal synchronization of the spark discharge, framing camera acquisition, and laser triggering was achieved through a delay generator (SRS DG645). Fig. G.4 shows framing images of a single spark event taken in reflection mode (top) and spectrum mode (bottom).

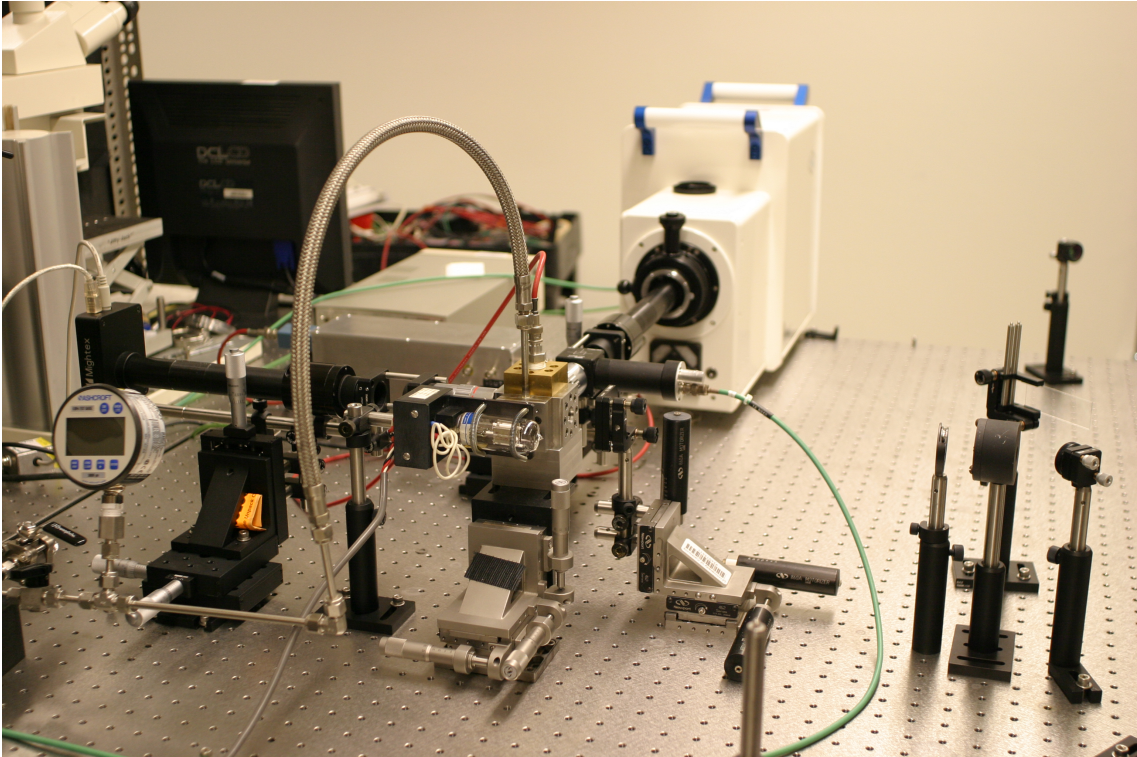


Figure G.5: Experimental photograph of the spark discharge with YAG laser absorption.

In reflection mode, the x-y dimensions are spatial and is illustrated by the tungsten electrode shadows. At  $t = -10$  ns, the focused laser passes through the electrode gap unimpeded (bright spot in center of image). At  $t = 0$  ns, the discharge is initiated and a bright plasma forms. The laser disappears for subsequent times ( $t = +10, +20$  ns) as the plasma becomes opaque. For long times after the discharge, the laser again passes through the electrode gap (bottom four images). Using this technique, the laser transmission can be measured as a function of the spark discharge (time, intensity, etc.). Improved signal:noise is achieved by spreading the spectrum in spectrometer mode (bottom graph). Once more, the laser is completely blocked by the spark discharge ( $t = 0, +10, +20$  ns) and achieves an instrument-limited attenuation ratio  $\gtrsim 4000 : 1$ .

A photograph for the spark discharge with high-intensity pulsed laser (YAG) absorption experiment is shown in Fig. E.1. A detailed description of the optical arrangement can be found in Chapter 8.

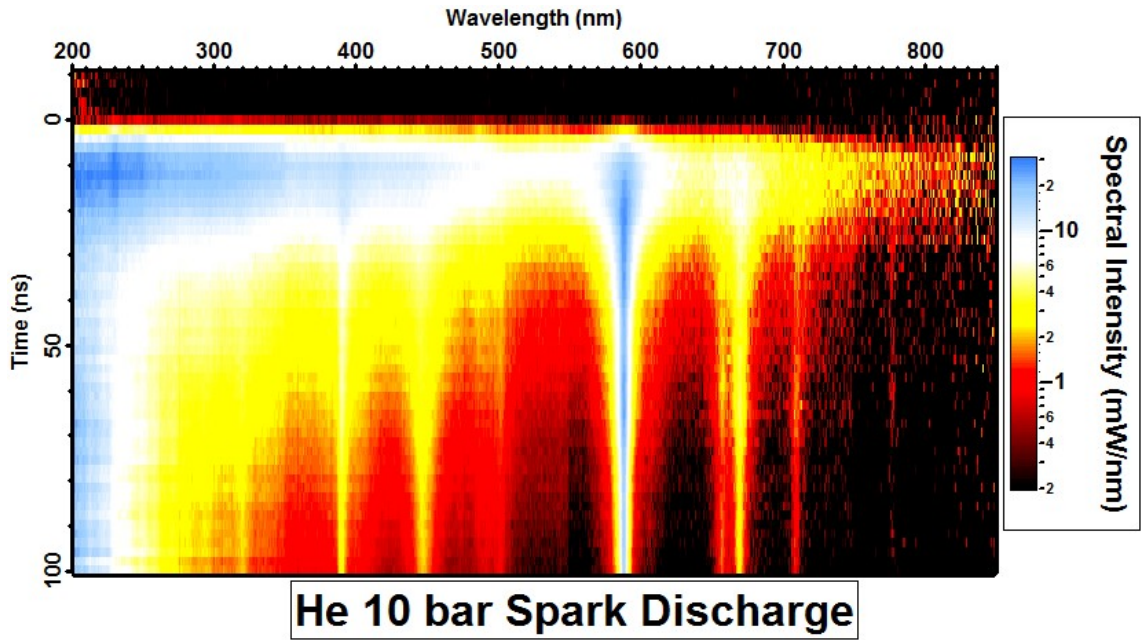


Figure G.6: Temporally-resolved spectral image for helium 10 bar spark discharge. Strong line emission is present for all times, indicating a transparent plasma.

## G.2 Spectrum

Time-resolved spectrum of the spark discharge was taken using a fiber-coupled spectrometer gated at 10 ns. In order to piece together single spectra in the temporal domain, the moment of discharge must be recorded relative to the spectrometer gate. This was accomplished with a fast photodiode shown in Fig. (8.2). Sorting each spectrum in time and averaging over 2 ns bins results in the spectral image in Fig. G.6. For the case of helium 10 bar breakdown, line emission dominates for all times. This is primarily due to the high ionization potential which limits the number of free electrons, and subsequent opacity. Spectra for xenon and helium 10 bar at early times are shown in Fig. G.7. Blackbody emission is well fit to the continuous portion of the helium spectrum with  $T = 13,000$  K and  $A = 4.8 \times 10^3 \mu\text{m}^2$ . This area indicates an emissivity  $\epsilon \approx 0.1$  when compared to the plasma area measured from the framing camera images.

After 10s of nanoseconds, the spectrum of xenon 10 bar discharge breaks from blackbody behavior and becomes line dominated (see Fig. 8.3). This drop in emissivity is due to hydrodynamic expansion as evidenced by the growing plasma radius from framing images,

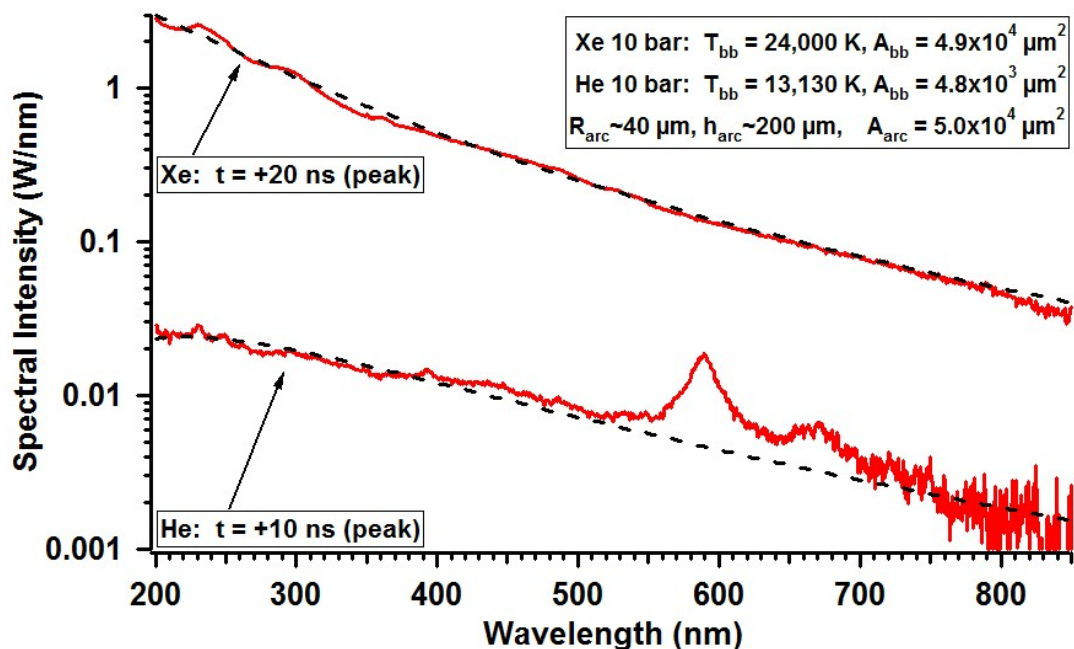


Figure G.7: Spectral intensity of 10 bar helium and xenon discharge at early times.

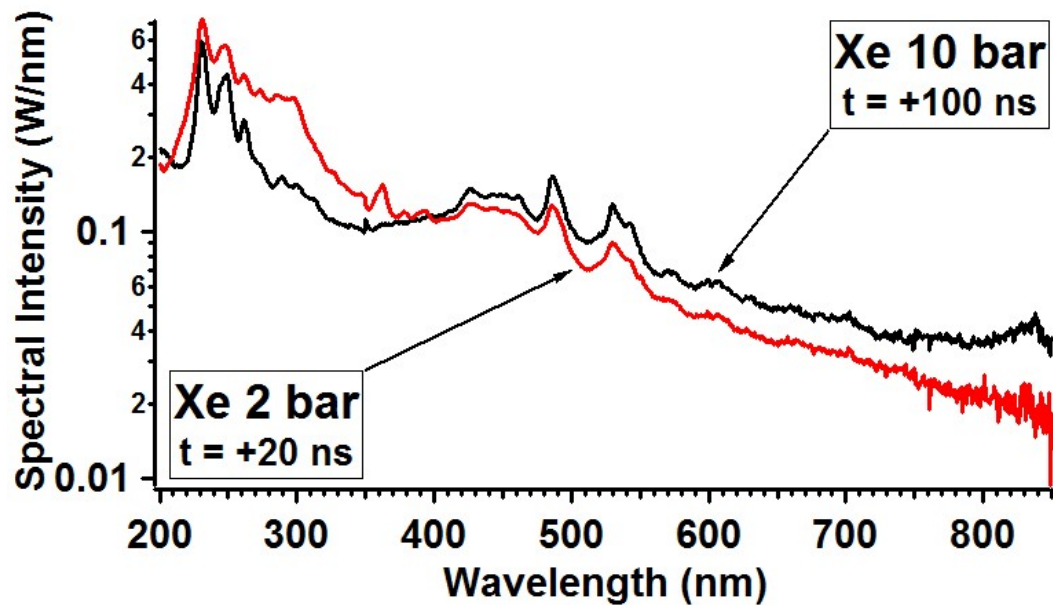


Figure G.8: Spectral intensity of xenon 10 and 2 bar taken at +100 and +20 ns, respectively.

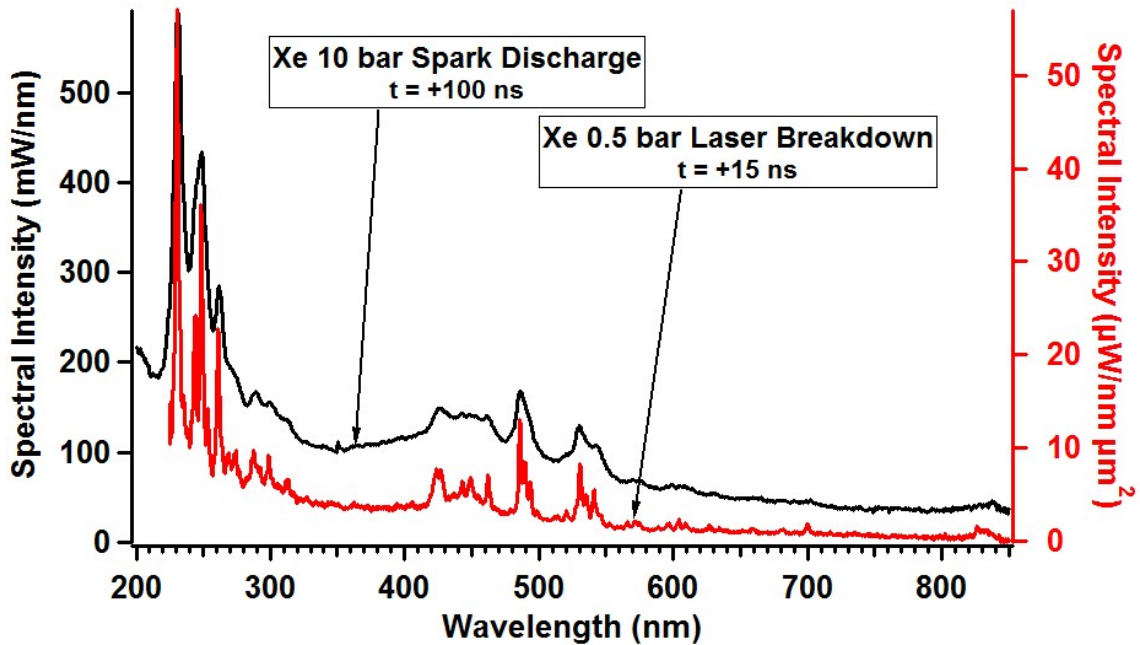


Figure G.9: Spectral intensity comparison of xenon 10 bar spark discharge and 0.5 bar laser breakdown.

growing spectral lines, and emitted shock waves. Fig. G.8 shows the spectral similarity in lower pressure discharges at early times and higher pressure discharges at later times. This spectra suggests the drop in opacity is due to the rapid decrease in density.

Although Saha's equation allows for any number of atomic species, the claim of a plasma phase transition due to density effects becomes unclear with the introduction of metallic contaminants. In this system, it is known that tungsten is removed from the electrode surfaces (see Fig. G.2) after every discharge. However, there are no indications that contamination affects the plasma discharge or is even within the plasma itself. For example, no spectral lines of tungsten are observed for xenon discharges. Although there are many lines that are difficult to distinguish, a comparison to laser-breakdown (Chapter 7) shows only the presence of xenon atomic lines (Fig. G.9). If contaminates are the primary source of free electrons, one would expect much weaker emission as the contaminants will have settled over long timescales. However, the intensity of plasma emission fluctuated by only  $\sim 10\%$  and is independent of the time between discharges. Furthermore, tungsten migrating to the center of the plasma from the electrodes during a discharge is limited by

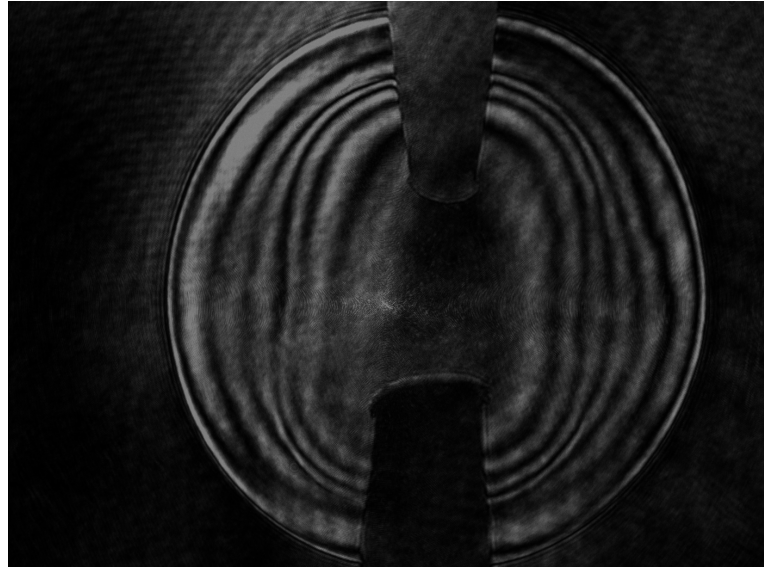


Figure G.10: Shadowgraph of shock front from 10 bar xenon discharge. The image is taken with a 3 ns YAG pulse timed 100s of nanoseconds after the discharge is initiated.

its high mass. For  $T = 24,000$  K, a tungsten atom can travel  $33\text{ }\mu\text{m}$  in 20 ns. Therefore, one would expect a very large intensity gradient down the plasma column. This is not observed and suggests the plasma phase transition is at work. (Note:  $33\text{ }\mu\text{m}$  should be considered an extreme upper bound as it assumes no collisions!)

### G.3 Shock waves

Although in its infancy, measurements have been made on the shock waves produced by spark discharges. A shadowgraph of 10 bar xenon discharge is shown in Fig. G.10. This image was taken by backlighting the electrodes with a 3 ns 532 nm YAG pulse. The sharp intensity discontinuity in the shape of a circle indicates the shock front. Once more, a timestamp for each spark-laser event is recorded using fast photodiodes and pieced together in time. For each shadowgraph, an averaged line-out of  $5\text{ }\mu\text{m}$  in height (relative to plasma length) is used to measure the plasma radius as a function of time. Fig. G.11 shows the shadowgraph intensity as a function of radius and time. The sharp increase in intensity indicates the shock front radius and is plotted in Fig. G.12 as a function of time. It is known that shock waves from instantaneous sources propagate with self-similar

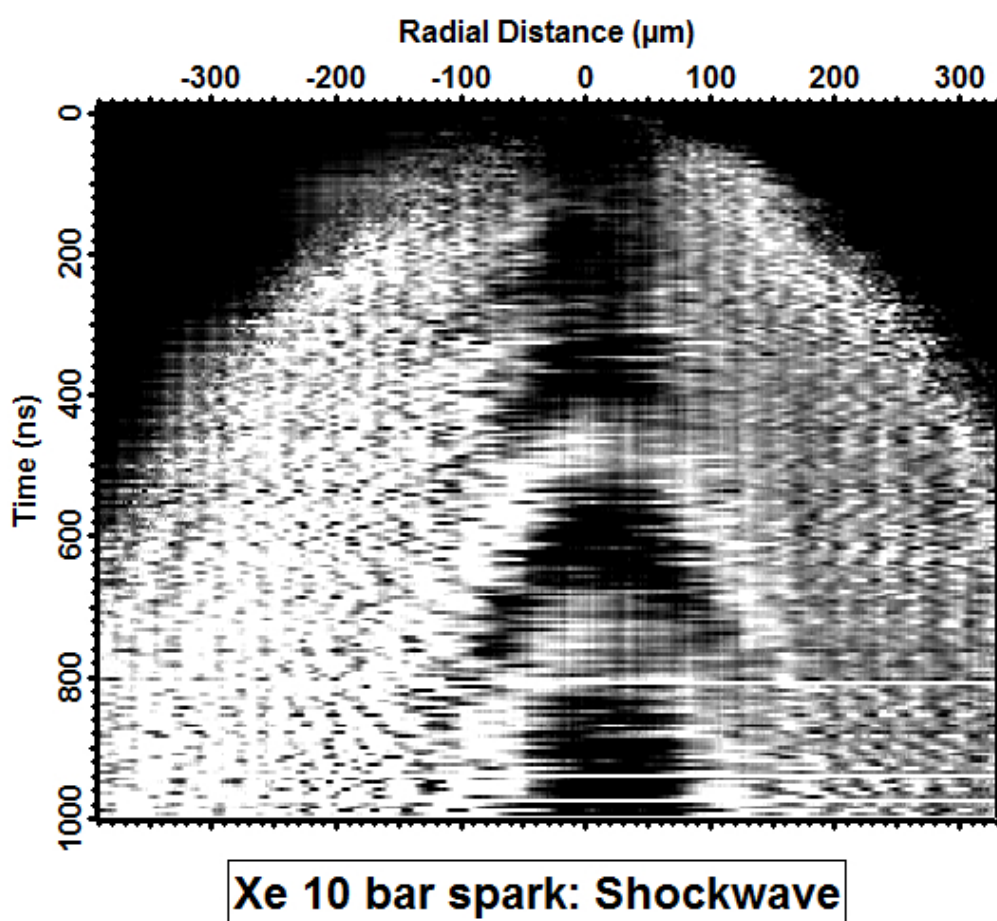


Figure G.11: Image of shock wave as a function of radius and time for 10 bar xenon discharge.

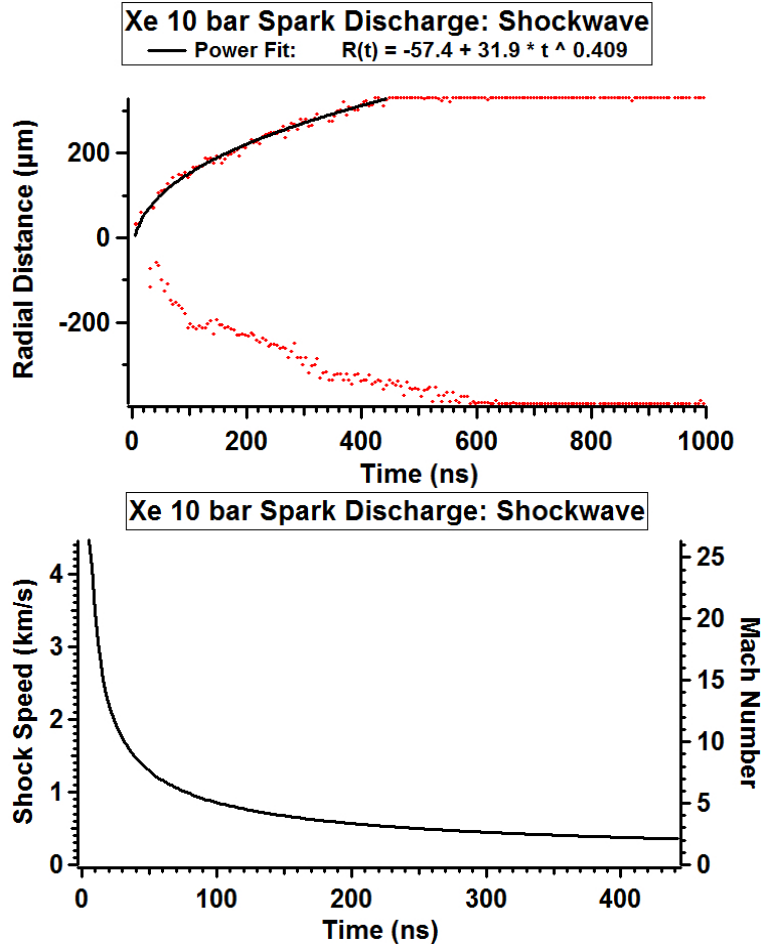


Figure G.12: Shock wave radius (top) and velocity (bottom) as a function of time for 10 bar xenon discharge. A power law is well fit (black curve) to the radius as a function of time.

profiles ([106]). For an instantaneous line source, the shock radius propagates as a power law given by

$$R(t) \propto t^{1/2}.$$

The experimental shock radius is well fit to a power law with a time dependence of  $t^{0.4}$  as shown in Fig. G.12. The speed of the shock front from the power law curve is shown and approaches speeds greater than Mach 10! Although these early results are promising, much more research is needed to extract the initial boundary conditions that describe the emission of these shock waves.

# Bibliography

- [1] Ohan Baghdassarian, Bernd Tabbert, and Gary Williams. Luminescence Characteristics of Laser-Induced Bubbles in Water. *Physical Review Letters*, 83(12):2437–2440, September 1999.
- [2] Ohan Baghdassarian, Bernd Tabbert, and Gary Williams. Luminescence from laser-created bubbles in cryogenic liquids. *Physical Review E*, 75(6):066305, June 2007.
- [3] Bradley Barber and Seth Putterman. Light scattering measurements of the repetitive supersonic implosion of a sonoluminescing bubble. *Physical Review Letters*, 69(26):3839–3842, December 1992.
- [4] Bradley P. Barber. Resolving the picosecond characteristics of synchronous sonoluminescence. *The Journal of the Acoustical Society of America*, 91(5):3061, 1992.
- [5] Bradley P Barber, Robert A. Hiller, Ritva Löfstedt, Seth J. Putterman, and Keith R. Weninger. Defining the unknowns of sonoluminescence. *Physics Reports*, 281(2):65–143, March 1997.
- [6] Bradley P. Barber and Seth J. Putterman. Observation of synchronous picosecond sonoluminescence. *Nature*, 352(6333):318–320, July 1991.
- [7] Alexander Bass, Steven Ruuth, Carlos Camara, Barry Merriman, and Seth Putterman. Molecular Dynamics of Extreme Mass Segregation in a Rapidly Collapsing Bubble. *Physical Review Letters*, 101(23):234301, December 2008.
- [8] A. Bataller, G. R. Plateau, B. Kappus, and S. Putterman. Blackbody Emission from Laser Breakdown in High-Pressure Gases. *Phys. Rev. Lett.*, 2014.

- [9] Bataller, A., Kappus, B., Camara, C. and S. Putterman. Collision Time Measurements in a Sonoluminescing Micro-Plasma with a Large Plasma Parameter. *Phys. Rev. Lett.*, 2014.
- [10] C. V. Bindhu, S. S. Harilal, M. S. Tillack, F. Najmabadi, and A. C. Gaeris. Laser propagation and energy absorption by an argon spark. *Journal of Applied Physics*, 94(12):7402, 2003.
- [11] N. Bloembergen. Laser-induced electric breakdown in solids. *IEEE Journal of Quantum Electronics*, 10(3):375–386, March 1974.
- [12] Iver Brevik, Valery Marachevsky, and Kimball Milton. Identity of the van der Waals Force and the Casimir Effect and the Irrelevance of These Phenomena to Sonoluminescence. *Physical Review Letters*, 82(20):3948–3951, May 1999.
- [13] E. Brush, S. G., Sahlin, H. L., Teller. Monte Carlo Study of a One-Component Plasma. I. *The Journal of Chemical Physics*, 45(6):2102, 1966.
- [14] A.A. Buzukov and V.S. Teslenko. Sonoluminescence Following Focusing of Laser Radiation into a Liquid. *JETP Letters-USSR*, 14(5):189, 1971.
- [15] Carlos Camara, Seth Putterman, and Emil Kirilov. Sonoluminescence from a Single Bubble Driven at 1 Megahertz. *Physical Review Letters*, 92(12):1–4, March 2004.
- [16] G. Cao, S. Danworaphong, and G. J. Diebold. A search for laser heating of a sonoluminescing bubble. *The European Physical Journal Special Topics*, 153(1):215–221, January 2008.
- [17] Avik Chakravarty, Theo Georghiou, Tacye Phillipson, and Alan Walton. Stable sonoluminescence within a water hammer tube. *Physical Review E*, 69(6):066317, June 2004.
- [18] Qi D. Chen and Long Wang. Luminescence from transient cavitation bubbles in water. *Physics Letters, Section A: General, Atomic and Solid State Physics*, 339:110–117, 2005.

- [19] Xi Chen and Peng Han. On the thermodynamic derivation of the Saha equation modified to a two-temperature plasma. *Journal of Physics D: Applied Physics*, 32(14):1711–1718, July 1999.
- [20] John Dawson and Carl Oberman. High-Frequency Conductivity and the Emission and Absorption Coefficients of a Fully Ionized Plasma. *Physics of Fluids*, 5:517, 1962.
- [21] P Debye and E Hückel. De la theorie des electrolytes. I. abaissement du point de congelation et phenomenes associes. *Physikalische Zeitschrift*, 24(9):185–206, 1923.
- [22] Guy Dimonte and Jerome Daligault. Molecular-dynamics simulations of electron-ion temperature relaxation in a classical Coulomb plasma. *Physical review letters*, 101:135001, 2008.
- [23] T. Ditmire, J. W. G. Tisch, E. Springate, et al. High-energy ions produced in explosions of superheated atomic clusters. *Nature*, 386(6620):54–56, March 1997.
- [24] W. Ebeling, A. Förster, W. Richert, and H. Hess. Thermodynamic properties and plasma phase transition of xenon at high pressure and high temperature. *Physica A: Statistical Mechanics and its Applications*, 150(1):159–171, May 1988.
- [25] W. Ebeling and W. Richert. Pressure Ionization of Atoms in Plasmas. *Beiträge aus der Plasmaphysik*, 25(5):431–436, 1985.
- [26] Claudia Eberlein. Sonoluminescence as Quantum Vacuum Radiation. *Physical Review Letters*, 76(20):3842–3845, May 1996.
- [27] S Eliezer. The interaction of high power lasers with plasmas. *Plasma Physics and Controlled Fusion*, pages 74–77, 2003.
- [28] David J Flannigan and Kenneth S Suslick. Plasma formation and temperature measurement during single-bubble cavitation. *Nature*, 434(7029):52–5, March 2005.
- [29] David J. Flannigan and Kenneth S. Suslick. Inertially confined plasma in an imploding bubble. *Nature Physics*, 6(7):1–4, June 2010.

- [30] V Fortov, I Iakubov, and A Khrapak. *Physics of Strongly Coupled Plasma*. International Series of Monographs on Physics. OUP Oxford, 2006.
- [31] H Frenzel and H Schultes. Luminescence in ultra-ray layered water. Short announcement. *Zeitschrift Fur Physikalische Chemie-Abteilung B-Chemie Der Elementarprozesse Aufbau Der Materie*, 27(5/6):421–424, December 1934.
- [32] D. Felipe Gaitan. *Ph.D. Thesis*. PhD thesis, University of Mississippi, 1990.
- [33] D. Felipe Gaitan. Sonoluminescence and bubble dynamics for a single, stable, cavitation bubble. *The Journal of the Acoustical Society of America*, 91(6):3166, 1992.
- [34] D.F. Gaitan, A. A. Atchley, S.D. Lewia, et al. Spectra of single-bubble sonoluminescence in water and glycerin-water mixtures. *Physical Review E*, 54(1):525–528, July 1996.
- [35] S. V. Garnov, V. V. Bukin, A. A. Malyutin, et al. Ultrafast Space-time and Spectrum-time Resolved Diagnostics of Multicharged Femtosecond Laser Microplasma. In *AIP Conference Proceedings*, pages 37–48. AIP, 2009.
- [36] M. Gitterman and V. Steinberg. First-Order Phase Transition in Metallic Vapors. *Physical Review Letters*, 35(23):1588–1591, December 1975.
- [37] Kenneth Goettel, Jon Eggert, Isaac Silvera, and William Moss. Optical Evidence for the Metallization of Xenon at 132(5) GPa. *Physical Review Letters*, 62(6):665–668, February 1989.
- [38] B. Gompf, R. Günther, G. Nick, R. Pecha, and W. Eisenmenger. Resolving Sono-luminescence Pulse Width with Time-Correlated Single Photon Counting. *Physical Review Letters*, 79(7):1405–1408, August 1997.
- [39] H R Griem. *Principles of Plasma Spectroscopy*. Cambridge University Press, Cambridge, U.K., cambridge edition, 1997.
- [40] Hans R Griem. High-Density Corrections in Plasma Spectroscopy. *Phys. Rev.*, 128(3):997–1003, November 1962.

- [41] Dominik Hammer and Lothar Frommhold. Sonoluminescence: How bubbles glow. *Journal of Modern Optics*, 48(2):239–277, February 2001.
- [42] E Newton. Harvey. Sonoluminescence and Sonic Chemiluminescence. *Journal of the American Chemical Society*, 61(9):2392–2398, 1939.
- [43] Sascha Hilgenfeldt, Siegfried Grossmann, and Detlef Lohse. A simple explanation of light emission in sonoluminescence. *Nature*, 398:402–405, 1999.
- [44] Sascha Hilgenfeldt, Siegfried Grossmann, and Detlef Lohse. Sonoluminescence light emission. *Physics of Fluids*, 11(6):1318, 1999.
- [45] R Hiller, K Weninger, S J Puttermann, and B P Barber. Effect of noble gas doping in single-bubble sonoluminescence. *Science (New York, N.Y.)*, 266:248–250, 1994.
- [46] Robert Hiller, Seth Puttermann, and Bradley Barber. Spectrum of synchronous picosecond sonoluminescence. *Physical Review Letters*, 69(8):1182–1184, August 1992.
- [47] Robert Hiller, Seth Puttermann, and Keith Weninger. Time-Resolved Spectra of Sonoluminescence. *Physical Review Letters*, 80(5):1090–1093, February 1998.
- [48] Stephen Hopkins, Seth Puttermann, Brian Kappus, Kenneth Suslick, and Carlos Camara. Dynamics of a Sonoluminescing Bubble in Sulfuric Acid. *Physical Review Letters*, 95(25):2–5, December 2005.
- [49] J D Huba. *NRL Plasma Formulary Supported by The Office of Naval Research*. 2011.
- [50] S Ichimaru. *Statistical Plasma Physics, Volume I: Basic Principles*. Frontiers in Physics Series. Westview Press, 2008.
- [51] Setsuo Ichimaru. Strongly coupled plasmas: high-density classical plasmas and degenerate electron liquids. *Rev. Mod. Phys.*, 54(4):1017–1059, October 1982.

- [52] Shin Itami and Tsutomu Araki. An intense, broadband emission spectrum, thyratron-gated nanosecond light source using a commercially available Xe short-arc lamp. *Review of Scientific Instruments*, 67(9):3035, 1996.
- [53] Tetsuo Iwata, Toshiki Tanaka, Toshiyuki Komatsu, and Tsutomu Araki. An externally controlled, nanosecond-pulsed, Xe lamp using a high voltage semiconductor switch. *Review of Scientific Instruments*, 71(11):4045, 2000.
- [54] Peter Jarman. Sonoluminescence: A Discussion. *The Journal of the Acoustical Society of America*, 32(11):1459, 1960.
- [55] Tudor Wyatt Johnston and John M. Dawson. Correct values for high-frequency power absorption by inverse bremsstrahlung in plasmas. *Physics of Fluids*, 16(5):722, 1973.
- [56] B. Kappus, A. Bataller, and S.J. Puttermann. Energy Balance for a Sonoluminescence Bubble Yields a Measure of Ionization Potential Lowering. *Physical Review Letters*, 111(23):234301, December 2013.
- [57] Brian Kappus, Shahzad Khalid, Avik Chakravarty, and Seth Puttermann. Phase transition to an opaque plasma in a sonoluminescing bubble. *Physical Review Letters*, 106(23):234302, 2011.
- [58] Brian Kappus, Shahzad Khalid, and Seth Puttermann. 100-Watt Sonoluminescence Generated By 2.5-Atmosphere-Pressure Pulses. *Physical Review E*, 83(5):056304, May 2011.
- [59] Brian A. Kappus. *Sonoluminescence: A Plasma Phase Transition*. PhD thesis, University of California, Los Angeles, 2010.
- [60] Brian A. Kappus, Avic Chakravarty, and Seth J. Puttermann. Drop tube generates 10-W flashes of sonoluminescence. *The Journal of the Acoustical Society of America*, 120(5):3165, 2006.

- [61] Shahzad Khalid, Brian Kappus, Keith Weninger, and Seth Puterman. Opacity and Transport Measurements Reveal That Dilute Plasma Models of Sonoluminescence Are Not Valid. *Physical Review Letters*, 108(10):104302, March 2012.
- [62] Sergey A. Khrapak. Effective Coulomb logarithm for one component plasma. *Physics of Plasmas*, 20(5):054501, 2013.
- [63] Yu. K. Kurilenkov and A. A. Valuev. the electrical conductivity of plasma in wide range of charge densities. *Beitr. Plasmaphys.*, 24(3):161–172, 1984.
- [64] L.D. Landau, EM Lifshitz, and L.P. Pitaevski. *Statistical Physics, Course of Theoretical Physics*. Butterworth-Heinemann, Oxford, 3rd ed., v edition, 1980.
- [65] F Lepoint-Mullie, D De Pauw, and T Lepoint. Analysis of the new electrical model of sonoluminescence. *Ultrasonics Sonochemistry*, 3(1):73–76, 1996.
- [66] Ritva Lofstedt, Bradley P. Barber, and Seth J. Puterman. Toward a hydrodynamic theory of sonoluminescence. *Physics of Fluids A: Fluid Dynamics*, 5(11):2911, 1993.
- [67] Robert Q. Macleay and Louis V. Holroyd. Space-Time Analysis of the Sonoluminescence Emitted by Cavitated Water. *Journal of Applied Physics*, 32(3):449, 1961.
- [68] M.A. Margulis. Fundamental problems of sonochemistry and cavitation. *Ultrasonics Sonochemistry*, 1(2):S87–S90, January 1994.
- [69] Thomas Matula, Ronald Roy, Pierre Mourad, William McNamara III, and Kenneth Suslick. Comparison of Multibubble and Single-Bubble Sonoluminescence Spectra. *Physical Review Letters*, 75(13):2602–2605, September 1995.
- [70] William C. Moss, Douglas B. Clarke, John W. White, and David A. Young. Hydrodynamic simulations of bubble collapse and picosecond sonoluminescence. *Physics of Fluids*, 6(9):2979–2985, September 1994.

- [71] V. V. Nesterenko and I. G. Pirozhenko. Is the Casimir effect relevant to sonoluminescence? *Journal of Experimental and Theoretical Physics Letters*, 67(6):445–449, March 1998.
- [72] J. Noack and A. Vogel. Laser-induced plasma formation in water at nanosecond to femtosecond time scales: calculation of thresholds, absorption coefficients, and energy density. *IEEE Journal of Quantum Electronics*, 35(8):1156–1167, 1999.
- [73] B E Noltingk and E A Neppiras. Cavitation produced by Ultrasonics. *Proceedings of the Physical Society. Section B*, 63(9):674–685, September 1950.
- [74] B. M. Penetrante, J. N. Bardsley, W M. Wood, C. W Siders, and M. C. Downer. Ionization-induced frequency shifts in intense femtosecond laser pulses. *Journal of the Optical Society of America B*, 9(11):2032, November 1992.
- [75] A. Prosperetti and Y. Hao. Modelling of spherical gas bubble oscillations and sonoluminescence. *Philosophical Transactions of the Royal Society A: Mathematical, Physical and Engineering Sciences*, 357(1751):203–223, February 1999.
- [76] Andrea Prosperetti. The thermal behaviour of oscillating gas bubbles. *Journal of Fluid Mechanics*, 222:587, April 1991.
- [77] S.J. Puttermann. Sonoluminescence: sound into light. *Scientific American*, 282(2):46–51, 1995.
- [78] F Quéré, S Guizard, and Ph Martin. Time-resolved study of laser-induced breakdown in dielectrics. *Europhysics Letters (EPL)*, 56(1):138–144, October 2001.
- [79] F Reif. *Fundamentals of statistical and thermal physics*. McGraw-Hill, 1 edition, June 1965.
- [80] T. K. Saksena. Sonoluminescence from Stable Cavitation. *The Journal of Chemical Physics*, 53(5):1722, 1970.

- [81] M Skowronek, J Rous, A Goldstein, and F Cabannes. Influence of Plasma Frequency on the Light Emitted by an Exploding Ionized Gaseous Filament. *Physics of Fluids* (1958-1988), 13(2), 1970.
- [82] L Spitzer. *Physics of fully ionized gases*. Interscience tracts on physics and astronomy. Interscience Publishers, 1962.
- [83] Devanatha Srinivasan and Louis V. Holroyd. Optical Spectrum of the Sonoluminescence Emitted by Cavitated Water. *Journal of Applied Physics*, 32(3):446, 1961.
- [84] John C. Stewart and Jr. Pyatt, Kedar D. Lowering of Ionization Potentials in Plasmas. *The Astrophysical Journal*, 144:1203, June 1966.
- [85] C.-K. Su, C. Camara, B. Kappus, and S. J. Puttermann. Cavitation luminescence in a water hammer: Upscaling sonoluminescence. *Physics of Fluids*, 15(6):1457, 2003.
- [86] Kenneth S Suslick. Sonochemistry. *Science (New York, N.Y.)*, 247(4949):1439–45, March 1990.
- [87] Kenneth S Suslick, Nathan C Eddingsaas, David J Flannigan, Stephen D Hopkins, and Hangxun Xu. Extreme conditions during multibubble cavitation: Sonoluminescence as a spectroscopic probe. *Ultrasonics sonochemistry*, 18(4):842–6, July 2011.
- [88] Kenneth S Suslick and David J Flannigan. Inside a collapsing bubble: sonoluminescence and the conditions during cavitation. *Annual review of physical chemistry*, 59:659–83, January 2008.
- [89] R P Taleyarkhan, C D West, J S Cho, et al. Evidence for nuclear emissions during acoustic cavitation. *Science (New York, N.Y.)*, 295(5561):1868–73, March 2002.
- [90] P. R. Temple. *Master's Thesis*. Master's thesis, University of Vermont, 1970.
- [91] Raúl Urteaga and Fabián J Bonetto. Trapping an intensely bright, stable sonoluminescing bubble. *Physical review letters*, 100:074302, 2008.

- [92] G Vazquez, C Camara, S Puttermann, and K Weninger. Sonoluminescence: natures smallest blackbody. *Optics Letters*, 26(9):575, 2001.
- [93] George Vazquez, C Camara, S J Puttermann, and K Weninger. Blackbody spectra for sonoluminescing hydrogen bubbles. *Physical review letters*, 88:197402, 2002.
- [94] K. Weninger, B. Barber, and S. Puttermann. Pulsed Mie Scattering Measurements of the Collapse of a Sonoluminescing Bubble. *Physical Review Letters*, 78(9):1799–1802, March 1997.
- [95] C.D. West and R. Howlett. Timing of Sonoluminescence Flash. *Nature*, 215(5102):727–727, August 1967.
- [96] Wm. Wood, C.W. Siders, and M.C. Downer. Measurement of femtosecond ionization dynamics of atmospheric density gases by spectral blueshifting. *Physical review letters*, 67(25):3523–3526, December 1991.
- [97] C. Wu and Paul Roberts. Shock-wave propagation in a sonoluminescing gas bubble. *Physical Review Letters*, 70(22):3424–3427, May 1993.
- [98] C. C. Wu and P. H. Roberts. A Model of Sonoluminescence. *Proceedings of the Royal Society A: Mathematical, Physical and Engineering Sciences*, 445(1924):323–349, May 1994.
- [99] Hangxun Xu, Nick G Glumac, and Kenneth S Suslick. Temperature inhomogeneity during multibubble sonoluminescence. *Angewandte Chemie (International ed. in English)*, 49:1079–1082, 2010.
- [100] Hangxun Xu and Kenneth S Suslick. Molecular Emission and Temperature Measurements from Single-Bubble Sonoluminescence. *Phys. Rev. Lett.*, 104(24):244301, June 2010.
- [101] Kyuichi Yasui. Mechanism of single-bubble sonoluminescence. *Physical Review E*, 60(2):1754–1758, August 1999.

- [102] Kyuichi Yasui. Single-Bubble and Multibubble Sonoluminescence. *Physical Review Letters*, 83(21):4297–4300, November 1999.
- [103] Kyuichi Yasui, Toru Tuziuti, Judy Lee, et al. The range of ambient radius for an active bubble in sonoluminescence and sonochemical reactions. *The Journal of chemical physics*, 128(18):184705, May 2008.
- [104] LI Yuan and Ping He. Influence of Sonochemistry on Single-Bubble Sonoluminescence. *Modern Physics Letters B*, 19(28n29):1711–1714, December 2005.
- [105] Mofreh R Zaghloul, Mohamed a Bourham, and J Michael Doster. A simple formulation and solution strategy of the Saha equation for ideal and nonideal plasmas. *Journal of Physics D: Applied Physics*, 33(8):977–984, April 2000.
- [106] Ya B Zeldovich. *Physics of Shock Waves and High Temperature Hydrodynamic Phenomena*. Dover, 2002.